A KINETIC STUDY OF
THE ELECTRON STIMULATED ADSORPTION OF AMMONIA
ON TUNGSTEN SINGLE CRYSTAL SURFACES

By

FU WING KONG, B. SC. (HONS.)

A Thesis

Submitted to the School of Graduate Studies

in Partial Fulfilment of the Requirements

for the Degree

Doctor of Philosophy

McMaster University

ELECTRON STIMULATED AMMONIA ADSORPTION ON TUNGSTEN

DOCTOR OF PHILOSOPHY (2004) (Chemistry)	McMaster University Hamilton, Ontario

TITLE:	A Kinetic Study of the Electron Stimulated Adsorption of Ammonia on Tungsten Single Crystal Surfaces
AUTHOR:	Fu wing Kong, B. Sc. (Hons.) (The Chinese University of Hong Kong)
SUPERVISOR:	Professor Peter T. Dawson

NUMBER OF PAGES: xxii, 201.

ABSTRACT

This thesis reports a comprehensive investigation of the effects of ammonia gas pressure, crystal temperature, electron beam current and angle of incidence on electron stimulated adsorption (ESA) of ammonia on W(100) and W(110) surfaces. An understanding of the kinetics of the ammonia dissociative adsorption has tremendous technological importance.

AES studies on the interaction of NH_3 with W(100) and W(110) have been conducted. The cross-section for ESA on W(110) is calculated to be 3.4×10^{-16} cm^2. The ESA rate increases with ammonia pressure at very low pressures but becomes independent of it at higher pressures. The ESA rate is first order in electron beam current but decreases with increasing crystal temperature. Except at low pressures, the ESA rate is found coverage-independent over a large coverage range. The desorption energies of two precursor states found are calculated to be 120 kJ mol^{-1} (N-W bonded) and 7 kJ mol^{-1} (H-bonded). All the evidence suggests a precursor state mechanism in which the activation sites and chemisorption sites are different. Yet it is inappropriate for a well-ordered single crystal surface and a novel alternative mechanism has been discovered.

The electron beam study leads to an understanding of how different adsorbates (NH_3, NH_2, NH and N) make different contributions to the measured overall N AES signal, and the signal attenuation is related to the shielding of the N atom by the bonded H atoms. An adsorption mechanism involving concepts about vacant site exclusion and stimulated dissociation of adsorbates was used to simulate the coverage evolution of individual adsorbates. The Auger sensitivity factors describing the signal attenuation from hydrogen shielding and from the electron beam's incident angle were deduced. The factors and the simulated coverages combined to produce simulated AES data that match the experimental results and reproduce the apparent coverage-independence.

ACKNOWLEDGEMENT

My special thanks and gratitude to my supervisor, Prof. Peter T. Dawson for his superior patience, consistent interest and encouragement over the course of this study. He led me to a most challenging research field, surface chemistry, and guided me throughout the duration of my graduate work. I cannot appreciate enough for his keen criticism, invaluable advice and suggestions in the preparation of this thesis.

Sincere thanks to Prof. Jacque Barbier and Prof. Randall S. Dumont, who served as members of my Ph. D. supervisory committee. Their advice and guidance are appreciated.

I thank McMaster University in providing financial assistance in the form of teaching assistantship, and the award of Centennial Scholarship. I would also like to express my gratitude for the research assistantship from Prof. Dawson.

Finally, I thank my dad, my wife and kids for their understanding and support throughout my time in the University.

Table of contents

Chapter One Introduction

Chapter Two Experimental techniques and instrumentation

Chapter Three Ground state adsorption of ammonia

Chapter Four Electron stimulated adsorption of ammonia

Chapter Five Ammonia pressure effect on the kinetics of the stimulated ammonia adsorption

Chapter Six Crystal temperature effects on the kinetics of the stimulated ammonia adsorption

Chapter Seven Effects of electron beam current density on the kinetics of the stimulated ammonia adsorption

Chapter Eight Angle of incidence of the electron beam and the stimulated ammonia adsorption

Chapter Nine Model for electron stimulated ammonia adsorption on tungsten single crystal surfaces

Chapter Ten Summary and conclusions

List of figures

Figure 9-17 The comparison between the simulated nitrogen AES signals and the experimental AES signals of the electron stimulated NH_3 adsorption on W (110), 5×10^{-7} torr NH_3, 300 K, normal incidence electron beam. Rate constants $k_1 = k_2 = k_3$.

Simulation parameters: $\alpha^{n}{}_{NH2,3}$ 100%, $\alpha^{n}{}_{NH}$ 40% and $\alpha^{n}{}_{N}$ 50%.

A more severe condition for re-activation of vacant sites.

Figure 9-18 The comparison between the simulated nitrogen AES signals and the experimental AES signals of the electron stimulated NH_3 adsorption on W (110), 5×10^{-7} torr NH_3, 300 K, glancing incidence electron beam. Rate constants $k_1 = k_2 = k_3$.

Simulation parameters: $\alpha^{g}{}_{NH2,3}$ 100%, $\alpha^{g}{}_{NH}$ 75% and $\alpha^{g}{}_{N}$ 11.5%.

A more severe condition for re-activation of vacant sites.

List of tables

Glossary

AES	Auger electron spectroscopy
ESA	Electron stimulated adsorption
ESD	Electron stimulated desorption
FWHM	Full width at half maximum
HREELS	High-resolution electron energy loss spectroscopy
IMFP	Inelastic mean free path
LEED	Low energy electron diffraction
QMS	Quadrupole mass spectrometer
RFA	Retarding field analyzer
SHG	Second harmonic generation
UPS	Ultraviolet photoemission spectroscopy
A	Pre-exponential factor
α_{NH_X}	Auger sensitivity factor
ΔE_{act}	Activation energy
E_d	Desorption energy
E_P	Energy of primary electron beam
E_{XYZ}	Kinetic energy of Auger electron of XYZ Auger transition
Φ	Work function
GS ads	Ground state adsorption
J	Electron current density
k_a	Adsorption rate constant
k_d	Desorption rate constant
N^{AES}	Nitrogen AES signal
$N(E)$	Energy distribution of electrons
Q	Cross section
θ_{NH_X}	Fraction coverage

CHAPTER ONE

INTRODUCTION

1.1 AMMONIA AND NITROGEN ADSORPTION ON TRANSITION METALS

The heterogeneous surface reactions between ammonia or nitrogen and transition metal surfaces have been an academic research topic for a century [Haber and Le Rossignol, 1908]. Some reaction products (transition metal nitrides) possess technologically attractive physical and chemical properties, while some others (e.g., ammonia or nitrate) are essential fertilizers to sustain the world population.

The nitrides of many transition metals have generated great theoretical and technological interest. Hafnium nitride, tantalum nitride, zirconium nitride and titanium nitride all have extremely high melting points (~3000 °C), and even vanadium nitride and niobium nitride have melting points higher than 2000 °C [Toth 1971, Lide 2003]. These refractory transition metal nitrides display industrially attractive physical properties such as good electrical and thermal conductivity, ultra-hardness and corrosion resistance [Kroll 2003, Zerr *et al.* 2003]. These nitrides are very good candidates as refractory, wear and corrosion resistant surface coatings.

With the loss of neighbouring atoms and the resulting changes in the coordination interactions, the atoms at the surface region of the metal nitrides behave differently from those in the bulk. Both adsorption and segregation change the surface composition from that of the bulk as the surface atoms seek different equilibrium spatial positions under new and decreased coordination. The physical properties of the transition metal nitrides are greatly dependent on the surface compositions, and hence a knowledge of the influence of any chemical reactions that change the surface structure and composition of these metal nitride coatings is of huge importance. Understanding the initial stages of interaction between nitrogen-containing gas molecules and transition metal surfaces, *i.e.*, the adsorption and the bulk diffusion, are critical to the growth of these metal nitride thin films and crucial to the aforementioned applications [Chen 1996].

The catalytic synthesis of ammonia from nitrogen (from air) and hydrogen (derived mainly from natural gas) - *i.e.*, the Haber process - is another economically important industry.

$$N_2(g) + 3\,H_2(g) \xrightleftharpoons{\text{Catalyst}} 2\,NH_3(g) \qquad \ldots (1\text{-}1)$$

The product from this nitrogen fixation process is an essential ingredient in the manufacture of fertilizers, explosives, and many other important chemicals. Therefore ammonia is produced in huge amounts annually (over 100 million tonnes in year 2000, see figure 1-1) [Max Appl. 2002]. The reaction mechanism is difficult to study since the equilibrium between the reactants and products requires a high pressure to produce an appreciable concentration of product. However, surface chemistry is best investigated under ultrahigh vacuum conditions with well-defined substrate surfaces. By the principle of microscopic reversibility, the reaction pathways for the ammonia synthesis are the same (reversed) as for the ammonia dissociation process and the ammonia dissociation can be studied in an ultrahigh vacuum system.

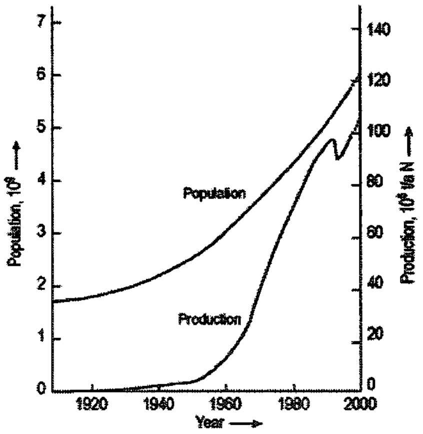

Figure 1-1
Development of ammonia production and world population. After Max Appl. [2002]

A key to improving both the transition nitride thin film formation and catalytic ammonia synthesis clearly relies on understanding the interaction of ammonia with the substrate surface. Thus an atomic scale kinetic investigation of the adsorption mechanism is an important academic research topic.

1.2 AMMONIA ADSORPTION PROCESSES

At room temperature or above, ammonia does not molecularly adsorb on tungsten surfaces. It chemisorbs in a dissociative manner, breaking at least one N-H bond to adsorb on the tungsten surface as NH_2 and H. This bond breaking can be facilitated by thermal activation, or electron stimulation.

1.2.1 Thermal activation

The dissociative adsorption of ammonia occurs via a transition state in which a N-H bond of an ammonia molecule is pulled apart by two neighbour sites on the surface (figure 1-2).

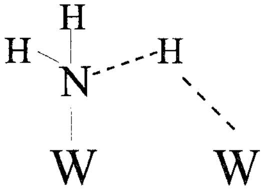

Figure 1-2 Schematic representation of a transition state during the chemisorption of ammonia on tungsten.

The endothermic N-H bond breaking is more than compensated by a new W-H bond formation and the strengthening of the N-W bond. The bond strength of $H-NH_2$ is 453 kJ mol^{-1} in free ammonia molecules [Berkowitz *et al.* 1994]. The dissociative adsorption of NH_3 is therefore allowed only when it is facilitated with the participation of a pair of vacant surface sites.

The direct result from this transition state formation is that the dissociative adsorption of ammonia on tungsten surfaces is limited to a half-monolayer coverage.

$$\theta = \frac{1}{2} \qquad \text{... via thermal activation}$$

θ being the fractional coverage of adsorbate. It takes two neighbour vacant surface sites to dissociate an ammonia molecule. Once the coverage reaches a half-monolayer with next nearest neighbour sites occupied on a (100) surface, C(2×2) structure, statistically there are no pairs of neighbour vacant sites left on the surface [Estrup and Anderson 1968, Griffiths *et al.* 1982, Bessent *et al.* 1995]. Ammonia adsorption ceases.

At room temperature, the ammonia coverage can be increased past half-monolayer when simultaneous electron stimulation is applied during the adsorption of ammonia.

1.2.2 Electron stimulation

Electron beams have been observed to cause significant changes in surface composition and structure [Madey and Yates Jr. 1971, Lichtman 1987, Rivière 1990, Ramsier and Yates Jr. 1991, Madey 1994, Tully 2000, Zaera 2001]. Because electrons have been used as the basis of many surface analytical techniques including electron microscopy, electron diffraction and electron spectroscopy, a thorough investigation of the influence of electron irradiation on an adsorbate / substrate system is necessary.

The electron-induced chemistry of ammonia adsorption on various surfaces has been studied to demonstrate the many surface processes triggered by electron stimulation [Chen 1996, Sun *et al.* 1996, Mocuta *et al.* 1997a, 1997b, Bater *et al.* 2000a, 2000b]. When electronically excited, weakly adsorbed ammonia will break an N–H bond, *i.e.*, electron stimulated dissociation. The remaining NH_2 fragments then develop a stronger interaction with the substrate, *i.e.*, electron stimulated adsorption (ESA, figure 1-3). The less energetic, fragmented hydrogen atoms are re-captured and adsorbed onto the substrate surface and are susceptible to further electron stimulated desorption (ESD).

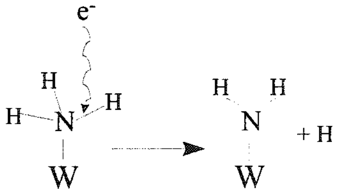

Figure 1-3 Schematic representation of the electron stimulation ammonia adsorption on tungsten surface. Only one surface site is required.

Several X-ray photoelectron spectroscopy (XPS) and high resolution electron energy loss spectroscopy (HREELS) experiments [Diebold and Madey 1992, Schwaner *et al.* 1996, Sun *et al.* 1996] have provided evidence of adsorbed NH_2, NH, N and H on the substrate surface. Mass spectrometry experiments have confirmed the desorption of H when an ammonia covered Cu(110) sample was bombarded with electrons [Mocuta *et al.* 1997 (a)].

The elementary surface process induced by electron excitation can be schematically expressed in the following equation:

$$W_2NH_2 + NH_3 \xrightarrow{e} 2\,WNH_2 + H \qquad \ldots (1\text{-}2)$$

where W_2NH_2 represents a NH_2 half-covered tungsten surface (one NH_2 for every two surface W atoms). WNH_2 is thus a NH_2 fully covered tungsten surface (one NH_2 for every surface W atom).

The impact of electron irradiation on the ammonia adsorption / decomposition on W(100) has been studied for decades. A LEED study by Anderson and Estrup [1968] reported that electron beams could produce a (1×1) structure from the NH_3 covered C(2×2) structure, *i.e.*, a doubling in surface concentration [also Tucker, Jr. 1964, Ermich 1965, Estrup and Anderson 1967 (a), 1968, Matsushita and Hansen 1970]. In 1996, Chen reported that full monolayer nitrogen coverage could be achieved on W(100), W(110) and W(111) by adsorbing ammonia with electron irradiation at room temperature. In all three samples the saturation nitrogen uptake is doubled from half monolayer without electron stimulation to a full monolayer with stimulation.

$$\theta = 1 \qquad \ldots \text{ via electron stimulation.}$$

1.3 THEORY OF ELECTRON STIMULATION

1.3.1 Introduction

The mechanisms proposed to explain electron stimulated dissociation, adsorption and desorption start from an electronic excitation followed by a relaxation. The initiation of these processes involves an electron-electron interaction causing an excitation of a bound electron in a surface adsorbate.

The possibility of a direct momentum transfer between a bombarding electron and an adsorbate species is mathematically found to be unimportant [McDaniel 1989]. The average relative energy loss (*i.e.*, the ratio between the energy loss by direct momentum transfer and the electron's original kinetic energy) of the incident electron in a classical collision of smooth elastic spheres is about $2m_e / M$, where m_e is the electron mass and M is the rest mass of the adsorbate. Consider the lightest possible M, a hydrogen atom; the relative energy transfer from the bombarding electron to the hydrogen atom is only about 0.1%. An electron of energy 500 eV can only transfer at most 0.5 eV to its collision partner, and the energy is too small to induce bond dissociation and desorption of an adsorbate. Unless incident electrons of energy up to 10 keV are employed, the minute energy transfer by direct momentum transfer is not an important factor in electron-induced processes.

In addition, the electron-adsorbate interaction is believed to be an isolated event. For the electron stimulated process to occur it needs only one incident electron to interact with an adsorbed species. This is supported by the large difference between the nominal adsorbate surface coverage ($\sim 10^{15}$ adsorbates cm^{-2}) and a typical electron current density ($\sim 10^{13}$ electrons cm^{-2} s^{-1}). The possibility of multi-electron stimulation surface processes is not ruled out, merely it requires only one electron collision / excitation to initiate the reaction and to take the adsorbate / substrate system to a state more energetic than the ground state configuration.

1.3.2 The Menzel-Gomer-Redhead (MGR) model

The first mechanism for the desorption of ions by electron stimulation was that proposed independently by Menzel and Gomer [1964] and Redhead [1964]. The general model incorporates adiabatic approximations and a semi-classical description of possible excitations of an adsorbate-substrate system. The excitation is usually thought as having a valence electron promoted into one of its excited states from a bonding ground state (see figures 1-4 and 1-5). The excited adsorbate (*e.g.*, in an ionic state as shown in figure 1-4) can either escape from the surface along a repulsive ionic potential curve or it can be neutralized and possibly escape as a neutral species [Ramsier and Yates, Jr. 1991]. This excitation is considered a Franck-Condon transition as the excitation is purely electronic, occurring so fast that no nuclear rearrangement occurs during the excitation period.

Most electronic transitions start from the zero vibrational level of the ground state configuration. The equilibrium distance between the adsorbate and the substrate surface is usually the shortest when the system is in its ground state. The ground state system in figure 1-4 is designated as (M + A) where M is a metal surface atom and A is the adsorbate. The representation is changed accordingly when the desorbing species is not the whole but only a fragment of the adsorbate molecule. M becomes the complex of the substrate surface *and* the un-desorbed fragment of the adsorbate, and A becomes the desorbing adsorbate fragment at the other end of the bond rupture. Similarly, the $(M + A)^*$ is then an electronically excited antibonding state, the $(M + A^*)$ is a vibrationally excited state and the $(M^- + A^+)$ system is an ionic state. Modifications for the present system, the electron stimulated dissociative adsorption of (weakly adsorbed) ammonia on tungsten surface, will have "M" representing the adsorbate-substrate complex $\left(W \cdots NH_2\right)$ and "A" the dissociated hydrogen atom. The changes are displayed correspondingly on figure 1-4.

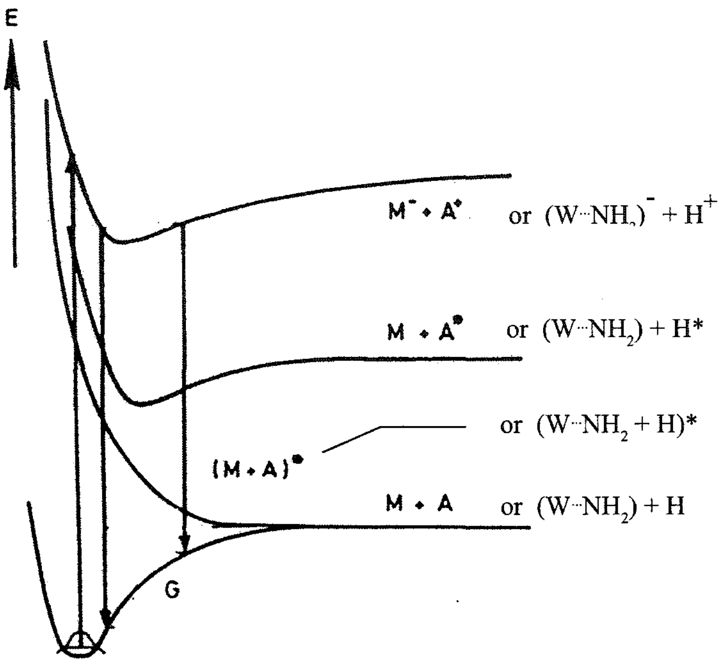

Figure 1-4 Schematic representation of the MGR model. The electronic transitions (vertical arrows) are Franck-Condon transitions.
Abscissa: distance between adsorbate and substrate; G: adsorbate ground state; (M+A)*: antibonding adsorbate state; M+A*: excited adsorbate state; M^-+A^+: ionized adsorbate state. After Madey [1994].

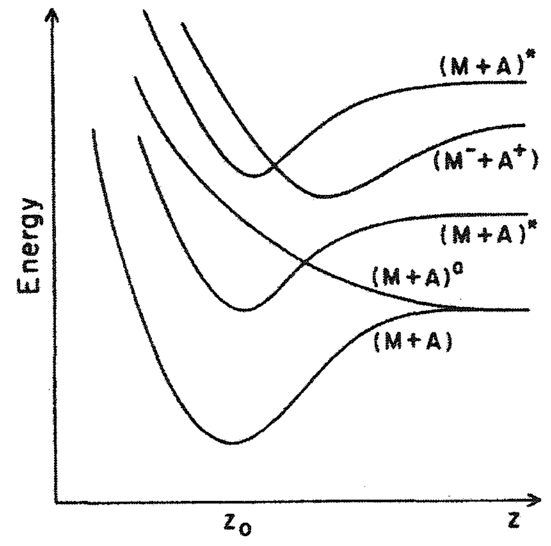

Figure 1-5 Superposition of potential energy curves from figure 1-4 to illustrate possible curve crossings in the MGR model. After Ramsier and Yates, Jr. [1991].

Applying a Franck-Condon transition means the electronic transition is vertical with respect to the reaction coordinate (figure 1-4). When an electron promotion from the ground state is vertical with respect to the reaction coordinate, the electronically excited system generally is in the repulsive state, accelerating the excited / ionized desorbate away from the surface and increasing its kinetic energy through the repulsion. The potential energy curves in figure 1-5 schematically illustrate the possible excited states of the adsorbate-substrate system after electron irradiation. It can be seen there are plenty of crossover possibilities from one excited state to another excited state (or even the ground state). The crossovers represent scenarios like Auger processes and resonant tunneling with the valence electrons of the substrate, which results in neutralization of ionic species to neutrals, or even de-excitation of those species.

The MGR model successfully explains the observed desorption of ions and ground state neutrals by electron irradiation. The incorporation of the Franck-Condon principle in the model is consistent with the collision process between electron and an adsorbate species being an isolated event. The model considers that electron tunneling from adsorbate to substrate, and from substrate to adsorbate, is fast in both directions, and explains the small overall cross-sections for electron stimulated desorption resulting from "bond healing" of broken or excited bonds by electron tunneling from the substrate. The cross-section for the stimulation is just as large as if the dissociation occurred in the gas phase, yet, because of the similarly large cross-section for relaxation by electron tunneling, the overall cross-section for desorption becomes small.

1.4 SCOPE OF THE THESIS

The purpose of this research project is to provide a detailed study of the effect of electron stimulation on the interaction of ammonia gas molecules with tungsten single crystal surfaces. The focus is on the understanding of the kinetics of the electron stimulated adsorption of ammonia on W(100) and W(110). While the kinetic studies of the ground state ammonia adsorption have been extensively studied, this is the first comprehensive research in the kinetics of the electron stimulated ammonia adsorption on tungsten. The increased full monolayer nitrogen coverage under mild conditions (non-destructive electron exposure and room temperature) highlights the importance of the better understanding of this reaction.

Being one of the most widely used methods for chemical analysis of surfaces, Auger electron spectroscopy serves as the principal analytical tool in this study. It is used to follow the progress of the reaction which requires the determination of the chemical composition of the surface layer quantitatively. Surface symmetry determination by low energy electron diffraction is performed whenever possible to help offer supporting evidence to surface coverage measurements.

The initial rate of nitrogen AES signal increase is found to be coverage-independent up to 70% of saturation coverage. Electron stimulated adsorption experiments are carried out at different ammonia pressure ranging between 1×10^{-9} and 5×10^{-7} torr, different crystal temperature from 300 to 465 K, of different electron beam current density from 0.6 to 2.9 μA mm^{-2}. The results suggest ammonia participates in the stimulated adsorption in a precursor state. The binding energy of the precursor and the cross-section for stimulated adsorption are determined.

Studies have also been focused on the effect of the angle of incidence of the electrons on the stimulated ammonia adsorption experiments. The results provide valuable insight in developing an adsorption model which includes an AES sensitivity factor for each of the dissociating ammonia species. Combining the simulated fractional coverages of the various NH_X adsorbates and the optimized AES sensitivity factors, the simulated data generated by this model agree well with the experimental data.

CHAPTER TWO

EXPERIMENTAL TECHNIQUES AND INSTRUMENTATION

2.1 SINGLE CRYSTAL SAMPLE CLEANING

The two single crystal samples, W(100) and W(110), used in this investigation were previously prepared for an earlier study in this research laboratory [Chen 1996]. The two crystals are discs sliced from high purity rods. The W(100) has a diameter of ~10 mm and a thickness of ~0.6 mm and the W(110) is ~12 mm wide and ~1 mm thick. They were mechanically polished with silicon carbide papers of 220 grit followed by 400, and then 600, and finally with diamond paste of particle size 6 and 1 μm successively. The samples were then solvent degreased in an ultrasonic bath. Thermocouples (W5%Re-W26%Re) were spot-welded on the sides of the samples. The crystal temperature was therefore determined from the junction voltage measured across the two thermocouple wires, with the reference junction immersed into an ice-water slush at zero degree Celsius.

The crystal samples were suspended on 0.01-inch tungsten wires and then mounted with stainless steel screws onto a custom-made sample holding carousel. The samples were then systematically cleaned from their common non-metal contaminants.

2.1.1 Sulphur and phosphorus

The samples were annealed at 1100 K to segregate both sulphur and phosphorus contaminants to the surface from the bulk, followed by argon ion sputtering to remove the outermost layers. The cycle of annealing-sputtering was repeated for over 130 times in three days. At the end neither sulphur nor phosphorus could be detected by AES even after 30 minutes of 1100 K annealing.

2.1.2 Carbon

Carbon contamination on the crystals was removed as carbon monoxide and dioxide by dosing oxygen gas to the sample surface which is kept at 1000 - 1400 K. The single crystals were annealed to 1300 K to segregate the carbon contaminant. After the surface segregation oxygen gas was dosed onto the hot crystal samples to allow the oxidation and desorption of the carbon contaminants.

2.1.3 Oxygen

Any oxide formed from the previous carbon cleaning procedure was decomposed by flashing the samples to as high as 2600 K.

No other impurity (*e.g.* silicon) was found. Subsequent to the optimized cleaning procedure, a clean surface of sufficient depth was available for the surface reaction investigations.

2.2 AUGER ELECTRON SPECTROSCOPY

Surface composition was determined by Auger electron spectroscopy (AES) [Woodruff and Delchar 1994]. The information is revealed in the magnitude of the measured Auger electron currents, which are affected by the back-scattering and transport through the surface region of incident electrons, the ionization cross section of core levels, the redistribution of core holes, and the transport of electrons through the surface into the vacuum [Hagstrum *et al.* 1976].

A couple of typical Auger electron spectra are shown in figures 3-1 (a) and (b) on page 42. The discussion of the details of the spectra is delayed till chapter three. In this section, the emphasis is put on the principle and method of the analytical technique.

2.2.1 The Auger process

In the present implementation of the AES technique the sample is irradiated by an electron beam (primary electrons) of energy in the keV scale. The energetic primary electrons are able to penetrate micrometres into a solid sample. The electron impact leads to an ionization, ejects core electrons of energy E_X in A atoms (for example),

$$A \rightarrow A^{+}(X) + e^{-} \qquad \ldots (2\text{-}1)$$

where $A^{+}(X)$ denotes that the hole in A is in level X.

The core hole left by the ejected electron (an excited state) is then filled by an internal, non-radiative de-excitation process in the atom. An electron of a higher energy E_Y falls into the core hole. The energy difference is carried by a third electron of energy E_Z. This Z level electron is then ejected from the atom and is called an Auger electron.

$$A^{+}(X) \rightarrow A^{2+}(Y, Z) + e^{-} \qquad \ldots (2\text{-}2)$$

where the emitted electron e^- is of kinetic energy E_{XYZ} outside the solid (*i.e.*, at a level $E_{XYZ} + \Phi$ above the Fermi level, Φ being the work function of the surface), and the atom is left doubly ionized with holes in its Y and Z levels.

The three-electron de-excitation process is called an *XYZ* Auger transition and the schematic representation of this Auger transition for surface nitrogen atom is shown in figure 2-1.

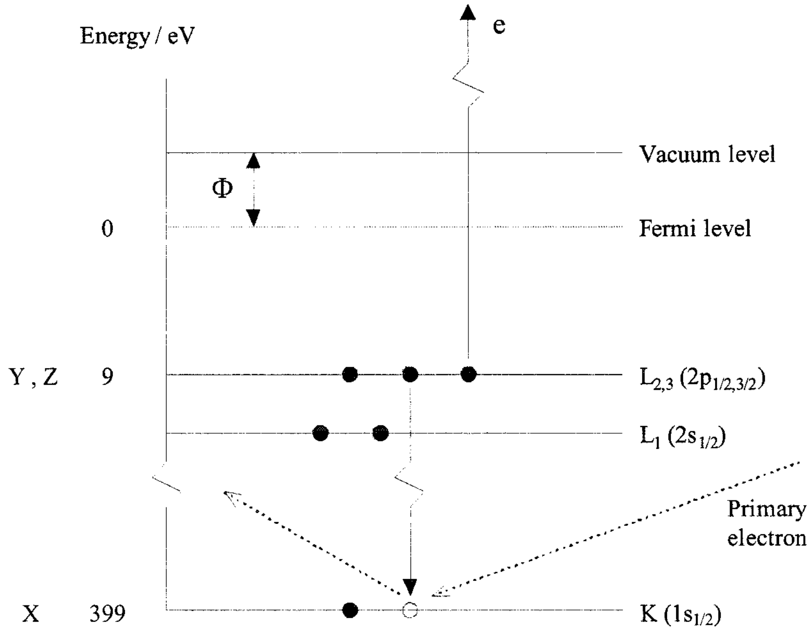

Figure 2-1 Schematic representation of an Auger process. The non-radiative XYZ Auger transition shown after primary electron excitation gives rise to the major N transition used in this study. the electronic energy levels are listed on the left as the binding energy in eV relative to the Fermi level. The X-ray and atomic notations are given on the right. The Auger electrons emitted by this process have a kinetic energy of 388 eV and are labelled N(388): $KL_{2,3}L_{2,3}$ ($1s_{1/2}$, $2p_{1/2,3/2}$, $2p_{1/2,3/2}$)

The characteristic energy of the Auger electron, E_{XYZ}, is approximated by equating the energies of the initial and final states of equation 2-2:

$$E_{XYZ} = E_X - E_Y - E_Z - \Phi \qquad \ldots (2\text{-}3)$$

where many-electron effects and final-state hole-hole interactions have been neglected. This ejected *Z* level electron thus has an energy characteristic of the element.

2.2.2 Surface sensitivity

The surface sensitivity of AES arises from the short inelastic mean free path (IMFP) of the low energy Auger electrons. In AES, a high-energy incident electron beam strikes a target, penetrates with both elastic and inelastic scattering within a depth of a couple micrometres, schematically shown in figure 2-2.

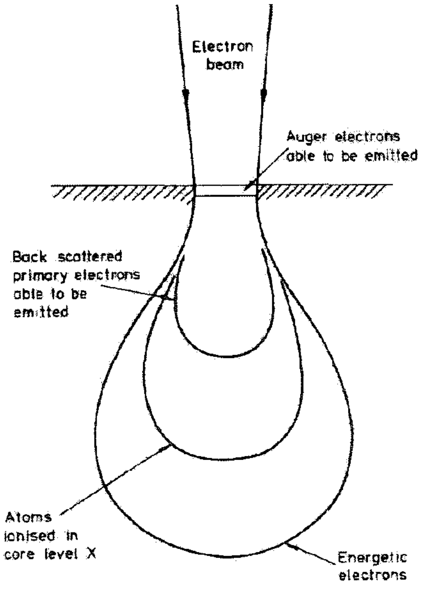

Figure 2-2 Schematic representation of electron scattering in AES. After Seah [1983].

As an Auger electron diffuses from its source in an underlayer, it may undergo numerous scattering events. Should its trajectory lead to an escape into the vacuum it can be collected with an electron spectrometer. Insignificant energy loss (in the order of a few tenths of eV) related to excitations of lattice vibrations or phonon losses would not alter the characteristic energy of the Auger electrons. However, those Auger electrons being scattered inelastically with a loss of sufficient energy will make them incapable of detection at the energy of the Auger transition and thus become part of the secondary electron background. In fact, the inelastic scattering is the basis for the surface sensitivity of the analytical technique. IMFP is defined as the characteristic distance that an electron of energy *E* travels with a probability 1/*e* of not being scattered by inelastic events that degrade its energy by more than several electron-volts [Jablonski and Powell 2002]. Experimentally such information on electron escape depth was obtained by a variety of methods [Brundle 1974, Lindau and Spicer 1974 and Powell 1974], and representative data are plotted in figure 2-3. Note that IMFP in the energy range 100 < *E* < 500 eV is very small: 5-10 Å, and is remarkably independent of material. Because of the very short escape depths for Auger electrons in this energy range AES is highly surface sensitive.

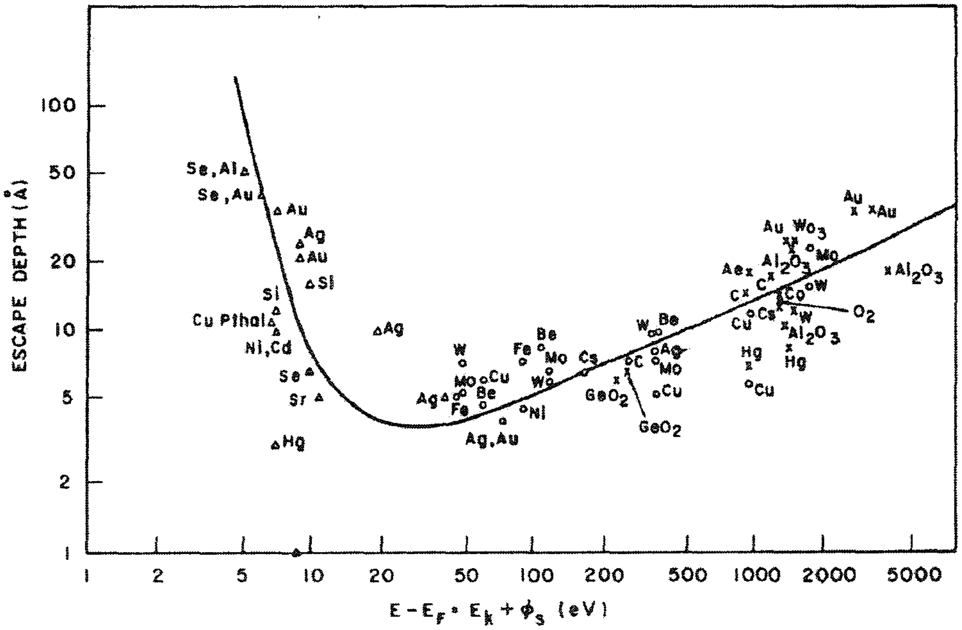

Figure 2-3 Graphs of experimentally determined electron escape depths versus electron energy for the elements indicated. After Hagstrum *et al.* [1976]

2.2.3 Energy analysis

The measurement of the kinetic energy distribution N_A (E_{XYZ}, E_P) of the emitted (Auger) electrons is the basis of this analytical tool, where E_{XYZ} is the kinetic energy of the Auger electron and E_P is the energy of the primary, ionizing electrons. The kinetic energy distribution includes a series of small peaks, the Auger peaks. Each peak corresponds to a characteristic Auger process in terms of the distinguishable core and valence energy levels involved. It is a very small component in the total distribution of electrons ejected from the solid. A primary electron beam produces a distribution of secondary and scattered electrons N_S (E_{XYZ}, E_P) outside the target, in addition to generating core holes, an elastic peak at $E = E_P$ is the most noticeable feature of this secondary and scattered electron distribution. The peaks caused by Auger emission from atoms in the surface region are barely observable on the relatively strong background of secondaries.

In this study an energy analyzer called retarding field analyzer (RFA) was used. While its structure will be discussed in section 2.4.1, its working principle is briefly discussed in this section. Its primary function is to act as a high pass filter to allow only electrons of energy higher than a certain value (the ramp voltage) to pass through it. Such electrons are then collected and measured as the Auger electron current.

When the ramp voltage is set at a given potential V_0, all electrons having energy greater than eV_0 (*i.e.*, E_0) reach the current collector at the back of the analyzer. If the electron energy distribution is $N(E)$ then the current arriving at the collector is $\int_{E_0}^{\infty} N(E)dE$, or as the highest energy electrons emitted have the primary beam energy E_P, the current is actually $\int_{E_0}^{E_P} N(E)dE$. To transform this current into the desired energy distribution $N(E)$ one differentiates the current with respect to the energy by modulating the retarding voltage V. When a measurement of the current arriving at the collector with retarding voltage V_0, and another with retarding voltage $V_0 + \Delta V$, the difference between these two currents is $\int_{E_0}^{E_0+\Delta E} N(E)dE$ and if $\Delta E = e\Delta V$ is small this equals $N_0(E_0)\Delta E$, and is thus proportional to the energy distribution required.

In practice, the retarding potential E_0 is modulated sinusoidally ($V_0 + \Delta V \sin \omega t$). Superimposed on the retarding potential is a small 10-eV modulation voltage (at about 1.4 kHz) from a signal source. The current arriving at the collector can by expressed as a sum of harmonics by the use of Taylor series expression [Woodruff and Delchar 1994]. In AES it is common to measure the amplitude of the *second* harmonic sin $2\omega t$ which can be achieved by using a phase sensitive detector. This amplitude is proportional to the differential of the energy distribution $N'(E)$, because the structure of interest in $N(E)$ is often weak (as a small peak on a large background). Differentiating removes the constant background and allows increased amplification. In addition, a broad peak in particular is more readily seen in the differentiated spectrum because it is changed into a *double peak*, each feature being narrower (see figure 2-4). In addition, the phase sensitive detector or lock-in amplifier also acts as a noise filter rejecting electron currents which do not oscillate with the imposed frequency.

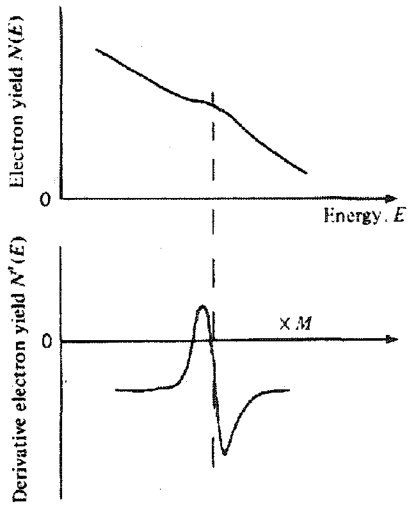

Figure 2-4 Schematic representation of the effect of taking the derivative of $N(E)$ with respect to E in the vicinity of a weak peak on a significant background. The derivative spectrum $N'(E)$ is amplified by some large factor M. After Woodruff and Delchar [1994].

2.3 LOW ENERGY ELECTRON DIFFRACTION

The microscopic surface structures of single crystal surfaces were investigated using low energy electron diffraction (LEED). In principle the diffraction pattern only provides information on the periodicity of the scattering system. However, much information can be inferred from such basic data, including the adsorbate coverage, the space group, or even the point group symmetry of the surface structure. With an interpretation of not only the diffraction pattern but also the diffracted beam intensities (which derive from the geometrical structure factor), a determination of the adsorbate-substrate registry is achievable [Armstrong 1976, Woodruff and Delchar 1994].

As with Auger electron spectroscopy, the surface sensitivity of LEED comes from the short escape depths of low energy electrons. In LEED experiments, the energy range of the electrons is generally 10-250 eV. The mean free paths for electrons in this energy range is only up to 15 Å.

When a crystal surface is bombarded with electrons at normal incidence, the electrons that scatter elastically are diffracted if their de Broglie wavelength is small enough. The de Broglie wavelength λ of electrons accelerated through a potential difference V (in V) is given by

$$\lambda / \text{Å} = h / \mathrm{p} = (150.4 / V)^{1/2} \qquad \ldots (2\text{-}4)$$

where h is the Planck constant and p is the momentum of the electrons.

The scattered electron waves meet the Laue condition for constructive interference when

$$d \sin \theta = n\lambda \qquad \ldots (2\text{-}5)$$

where d is the distance between the individual crystal planes, θ is the angle of the scattered beam relative to the normal incidence of the primary beam and λ is the wavelength of the electron. Hence if the surface atoms are orderly arranged in a periodic lattice, the surface acts as a two-dimensional grating and the interaction produces a set of discrete diffracted beams.

Much information can be obtained directly from observation and measurement of the geometrical features of the LEED pattern of diffracted beam terminations on a fluorescent screen. On an ideally uniform flat crystal surface the beam pattern represents the two-dimensional reciprocal net. One often can reconstruct from the experimental LEED pattern the direct net with the following conditions:

$$x_1 \bullet x_1^* = x_2 \bullet x_2^* = 1 \text{ and } x_1 \bullet x_2^* = x_2 \bullet x_1^* = 0 \qquad \ldots (2\text{-}6)$$

where x_1 and x_2 are the unit vectors of the real space lattice, and x_1^* and x_2^* are the unit vectors of the reciprocal lattice, respectively (figure 2-5). Based on these conditions, the size and the orientation of the real space lattice can be determined. In some cases, even the superlattices induced by reconstruction or by adsorbed monolayers and the possible presence of symmetrical domains can be revealed.

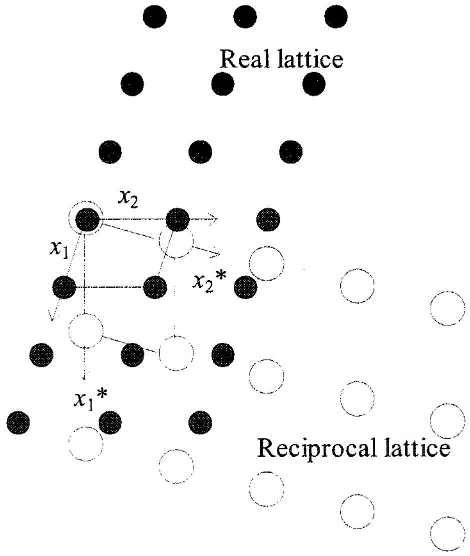

Figure 2-5 Relationship between an oblique direct lattice and its reciprocal lattice.

The determination of the specific atomic positions within the surface unit mesh or in a three-dimensional unit cell including more than one layer at the surface is called LEED crystallography. Unlike the determination of the bulk structure in X-ray crystallography, the combined problems of the atomic scattering factors and the different multiple scattering environments of each atom make *direct* Fourier transform methods not applicable in LEED structure analysis [Woodruff and Delchar 1994]. The structural determinations can only be performed by comparing experimental LEED intensity data with the results of theoretical calculations or simulations based on trial structures. When good agreement is achieved between theory and experiment the relevant trial structure is deemed to be the true structure. No LEED crystallography has been attempted in this work.

2.4 EXPERIMENTAL METHODS

The ultra high vacuum system used in this investigation is shown schematically in figure 2-6.

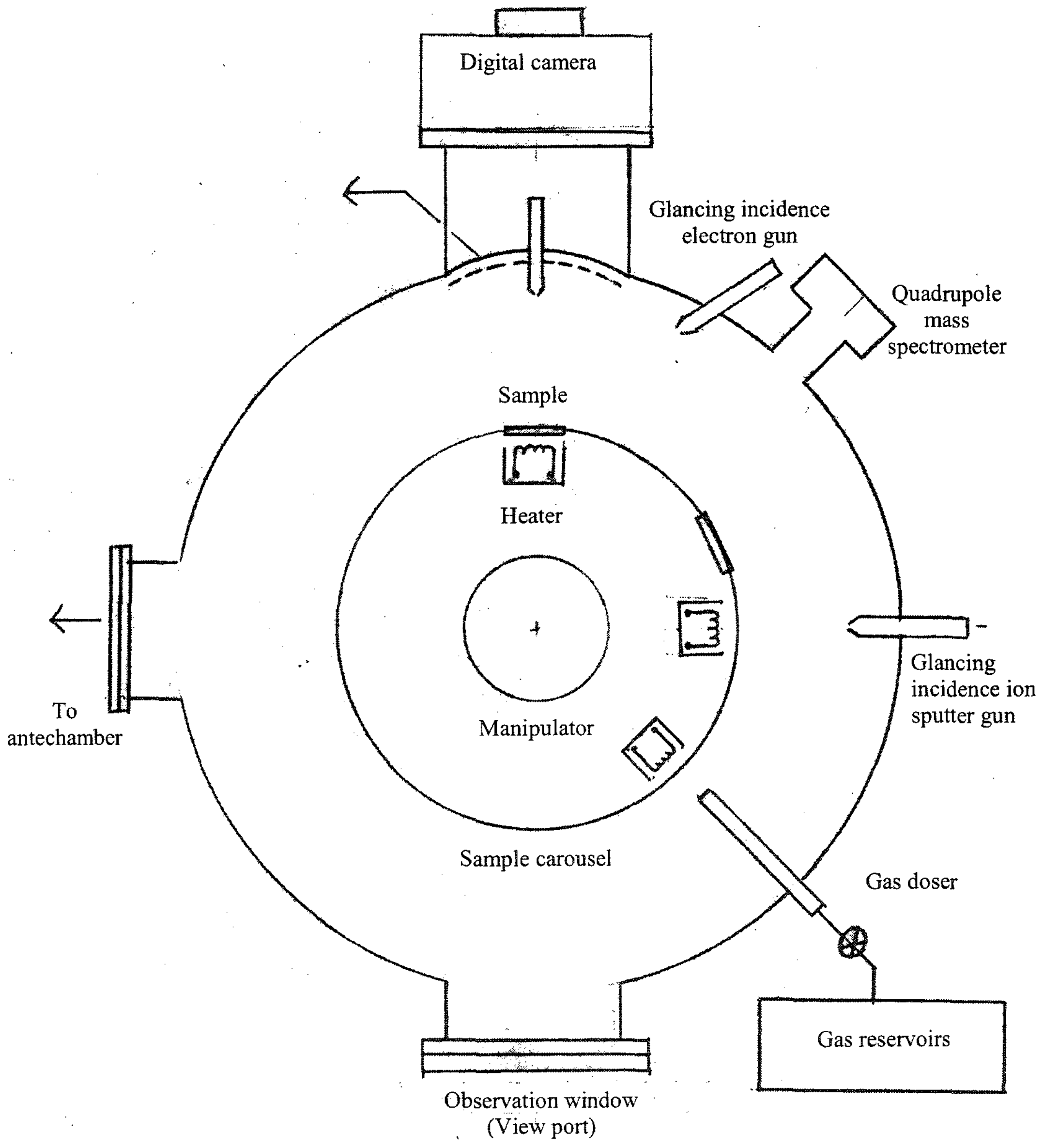

Figure 2-6 Schematic drawing of the ultrahigh vacuum system with the instruments. Not shown are a poppet valve, the pump well and a leak valve for argon admission.

2.4.1 Integrated LEED / AES retarding field electron optics

In this study, a hemispherical four-grid retarding field analyzer (OCI Vacuum Microengineering BDL 800) was used for both LEED and AES [Seah 1983, Woodruff and Delchar 1994] (figure 2-7). The first and fourth grids of the analyzer are at the potential of the crystal (ground), so that a field-free space is created. This design also shields the collector from capacitive coupling with the modulation of the other grids. The two grids sandwiched in between are connected together and have the programmed potential applied to them. The grids are made from tungsten wire mesh and are gold coated to have a chemically resistive surface with uniform work function. At the back of the analyzer is a fused silica hemisphere screen coated with indium-tin oxide to provide a transparent conductive layer and high luminosity phosphor P^{31} which fluoresces proportionately when collided by electrons. The analyzer has an acceptance angle of 100°.

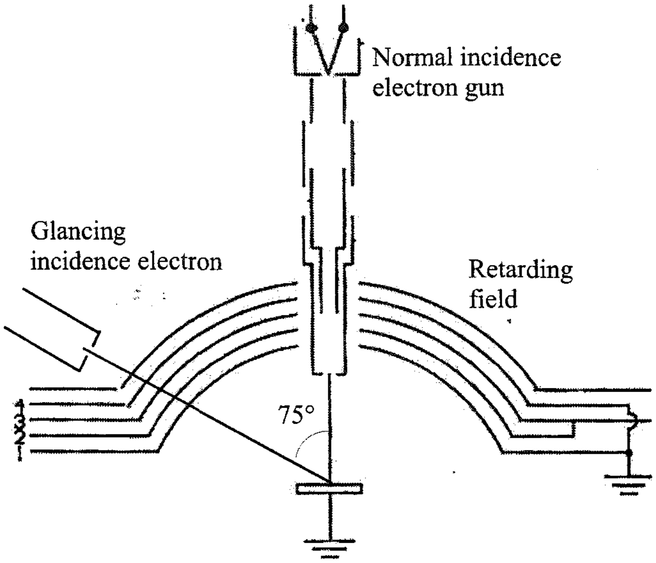

Figure 2-7 Schematic diagram of the integrated AES / LEED electron optics and the glancing incidence electron gun.

A miniature electron gun, body diameter of only 10 mm, is aligned along the central axis of the optics. The gun does not obscure the screen and does not produce stray light from the tungsten-rhenium hairpin filament, for the benefits of LEED experiments. The whole assembly is magnetically shielded by a Mu-metal [1] tube. A mechanically operated shutter is in front of the electron gun.

---

[1] Mu-metal is a nickel-iron alloy (~75% Ni, 15% Fe, plus Cu and Mo) which has extremely high magnetic permeability at low field strengths.

2.4.2 Glancing incidence electron gun for AES

There is an additional electron gun capable of irradiating a crystal sample (positioned in front of the integrated AES/LEED retarding field analyzer) with a high-energy electron beam at glancing incidence. The off-normal glancing incident angle is 75°.

2.4.3 Digital camera for LEED patterns recording

An 8-bit, 256 level grey scale digital camera (Electrim EDC-1000N) is mounted at the view port (outside the vacuum chamber) behind the phosphor-coated glass screen of the LEED electron optics. The lens of the camera is encased in a custom-built aluminium case to prevent stray light getting into the camera. The camera is computer-interfaced and is able to record frames of array spatial resolution up to 652 × 494 pixels. LEED images captured by the camera can be displayed on a computer monitor in real time.

2.4.4 Quadrupole mass spectrometer

Besides the electron optics, the vacuum chamber is also equipped with a quadrupole mass spectrometer (QMS) to monitor the gas composition. This residual gas analyzer can measure ions with mass/charge ratios in the range 1-200 amu (atomic mass units).

2.4.5 Glancing incidence ion sputter gun

A high-energy sputter gun at glancing incidence is mounted onto the vacuum chamber. When the chamber is filled with argon at low pressure, this sputter gun can be used to bombard a sample surface with a beam of argon cations of energy 2 keV and an ion current of 25 μA. The beam can be electronically rastered to avoid inducing crater formation on the sample surface.

The ultrahigh purity argon used in the sputtering experiments was used as is from the gas cylinder without further purification. Before an experiment, the argon gas was first taken from the cylinder and stored in an individual gas line. A leak valve was connected at the other end of the gas line for the gas admission into the vacuum chamber. The purity was maintained by use of a titanium sublimation pump to getter impurities.

2.4.6 Gas doser and gas handling system

A multi-orifice gas doser, which yields an enhanced gas flux at the sample surface with homogeneous distribution across the sample and to keep the background gas pressure in the ultrahigh vacuum chamber at a low level, was designed by Chen [1996] and was also used in this investigation. Six orifices (1/32" diameter) were hexagonally distributed on the front end (1/2" diameter and 1/16" thickness) of the doser. To ensure the gas fluxes before the orifices were random, a hemispherical copper sheet with a central hole was used to create a random molecular distribution before the orifices. When the sample is ~7 mm away from the gas doser, the majority of the sample surface (except the edges) can be exposed to a nice homogeneous gas flow. The gas flux is calculated from the period of dosing and the change in gas pressure measured by a 1-torr Baratron pressure transducer in a stainless steel gas reservoir of known volume.

2.4.7 Sample heating

Sample heating was performed by electron bombardment heating at the backside of the sample. A 0.005-inch diameter tungsten wire filament was located in a shielding cylinder made of tantalum. The filament was heated to the very high temperatures required for thermionic electron emission by applying a 0-12 V ac voltage and biased by a negative 0-2 kV dc voltage to accelerate the emitted electrons onto the grounded sample.

2.4.8 Pumping system

The ultrahigh vacuum condition in the system was routinely maintained by a set of five triode ion pumps with a combined pumping speed of 200 L/s. The pumping mechanism was basically a removal of gas molecules from the vacuum via an electron-impact ionization of the gas molecules and then imbedding the produced ions into a chemically active titanium cathode.

These pumps were connected directly to the chamber without any intervening traps. The pumps were located at the bottom section of the vacuum chamber and could be isolated from the top analysis section via a poppet valve. This poppet valve was usually left fully opened so the chamber was under full pumping.

When a gas pressure of 10^{-7} torr or above is needed in the vacuum chamber for sputtering or adsorption experiments, the poppet valve is tightened to reduce or stop the gas pumping in the analysis section.

A titanium sublimation pump was installed into the chamber for occasional, accelerated pumping. When in use, a high current was passed through a titanium-molybdenum alloy filament. The resistive heating preferentially evaporated the titanium and deposited it as a finely divided layer with a high surface area onto a surrounding cylinder. Gases inside the vacuum chamber then chemically reacted with the evaporated titanium (*i.e.* gettering) and were removed from the gas phase. The sublimation pump was not effective in pumping inert gases like argon and methane.

2.5 EXPERIMENTAL PROCEDURES

2.5.1 Auger electron spectroscopy

Auger electron spectra were collected in the derivative mode using the retarding field energy analyzer. For the majority of the AES measurements, the miniature electron gun integrated with the AES/LEED optics was used. The electron beam generated was at normal incidence to the crystal surface. The standard operating condition was a primary 2.0 keV, 25.0 μA electron beam of ~1 mm diameter. When the effect of the incident angle of the electron beam was studied, the electron gun at glancing incidence to the crystal surface was employed. The 75° off-normal incidence electron beam was of energy 1.5 or 2.0 keV and current 25.0 μA. The spectrometer was computer-controlled. The analogue output signal amplified by the phase-sensitive lock-in amplifier was digitized by a 12-bit analogue-to-digital converter, interfaced with a computer which stored the spectra. Appropriate energy windows were swept consecutively taking eight measurements at each ramp energy value. Because most of the interesting Auger transitions were at 100 eV and higher, the sweep resolution was programmed to 0.5 eV and the modulation voltage 10 V peak-to-peak.

2.5.2 Low energy electron diffraction

In a LEED experiment, the sample crystal was positioned at the focal point of the hemispherical, fluorescent and transparent screen. Diffracted electron beams emerging from the surface of the crystal hence travelled radially toward the screen. The grid nearest to the sample (grid #1 in figure 2-7) was grounded so that the diffracted beams follow linear trajectories in field-free space. The next two grids (#2 and #3) were linked and maintained at a potential (the retarding voltage) a few volts below the incident electron beam. This pair of grids assumed the role of an energy-selection grid: electrons which had been inelastically scattered and had lost more than a few volts would have insufficient energy to pass the grids and thus did not reach the screen. The grid that was nearest to the screen (grid #4) was grounded to separate the screen potential from the energy-selection potential (on the double grids).

The screen was biased to 3.0 kV, so that approaching electrons were accelerated rapidly towards the conductive oxide layer. Electrons which passed thought the selection grids and impinged on the screen created a glow proportional to the beam intensity. The LEED pattern recorded by the digital camera was displayed on a monitor in real time, allowing fine adjustments to the screen voltage, focus voltage and beam current of the electron optics assembly, as well as the exposure time on the camera.

2.5.3 Argon sputtering

A rastered 2 keV argon ion beam was directed at 75° to the surface normal in a standard argon environment of pressure 5×10^{-5} Torr. The ion beam current density measured with a Faraday cup was ~0.1 μA mm^{-2}.

The ion beam rastering was applied to prevent possible crater formation on the sample surface. Generally, annealing followed sputtering to heal and re-order the symmetry of the single crystal surfaces.

CHAPTER THREE

GROUND STATE ADSORPTION OF AMMONIA

3.1 INTRODUCTION

Ammonia interaction with tungsten surfaces has been extensively studied for many decades. Several reviews have been published [Yih and Wang 1979, Lambert and Bridge 1984, Raval *et al.* 1990, Rao and Rao 1991, Uebing 1998]. The purpose of this chapter is to report the experimental results acquired for ground state ammonia adsorption experiments on both W(100) and W(110) in this laboratory with the current instruments to serve as a reference for comparison with the results of the subsequent electron stimulated ammonia adsorption experiments.

3.2 EXPERIMENTAL PROCEDURES

The ammonia gas used in this investigation was ultra high electronic grade, supplied by Matheson Gas Products Inc.. The gas was introduced and stored in a stainless steel gas handling line. The gas handling line had been baked extensively before gas introduction. The ammonia gas was used as is, without further purification. The gas purity was monitored by a residual gas analyzer when it was admitted into the vacuum chamber.

In ground state adsorption studies all filaments in the vacuum system were switched off to prevent electron stimulation effects. The sample was turned to face the multi-orifice gas doser during adsorption. The gas flux was regulated to between 2×10^{14} and 5×10^{15} molecules cm^{-2} s^{-1} by adjusting the precision leak valve from the dosing line and the poppet valve to the pumping system. The background gas pressure in the chamber was about 10^{-7} torr during ammonia dosing, with nitrogen being the second most abundant species after ammonia. At the end of adsorption the sample was turned away from the dosing position and the precision leak valve was immediately turned off to stop the gas dosing. The poppet valve was opened fully to maximize the pumping speed and if necessary, a titanium sublimation getter was flashed to help decrease the gas pressure in the vacuum chamber. The background pressure quickly decreased to the low 10^{-8} torr range in the first half hour. Further pressure decrease became very sluggish because of the slow pumping speed of ammonia gas. Once adsorbed onto the internal walls of the vacuum chamber, ammonia desorbed slowly and persisted in the gas phase. No electrons were allowed to impact the sample surface until the ammonia pressure had fallen below 1×10^{-9} torr.

3.3 RESULTS AND ANALYSES

3.3.1 Ground state adsorption at room temperature

Auger electron spectra (100-600 eV) of a clean W(100) surface and after ammonia adsorption are shown in figures 3-1 (a) and (b). The Auger peaks at 150-200 eV originate in W(NNN) Auger transitions and those at 340-380 eV are from N(KLL) transitions [Childs and Hedberg (1995)]. The nitrogen Auger peak heights measured over the period from 5 to 90 minutes ammonia dosing using the multi-orifice gas doser at room temperature are shown in figure 3-2, and summarized in table 3-1. The signals changed minimally over this time interval. The peak height of individual Auger peaks was defined as the difference between the highest and the lowest signal of the peaks, as shown in figure 3-3. The peak height, which is the derivative electron yield $N'(E)$, is reported in the dimensionless arbitrary units.

Knowing that electron irradiation can stimulate ammonia adsorption on the tungsten single crystal surfaces, the AES measurements were made only after the residual ammonia partial pressure had dropped below 1×10^{-9} torr. As mentioned in the previous section, the pumping of ammonia generally required several hours and so, to minimize contamination, each data point in figure 3-2 represents a separate measurement.

The experimental results indicated the ammonia adsorption has reached saturation on the tungsten surface after five minutes active dosing with the given gas flux at room temperature. The finding agreed with the results reported by Chen [1996].

The W(110) surface exhibited similar features of saturated ammonia adsorption at room temperature in a short active dosing period. The saturation level was slightly lower than for W(100). (see table 3-1)

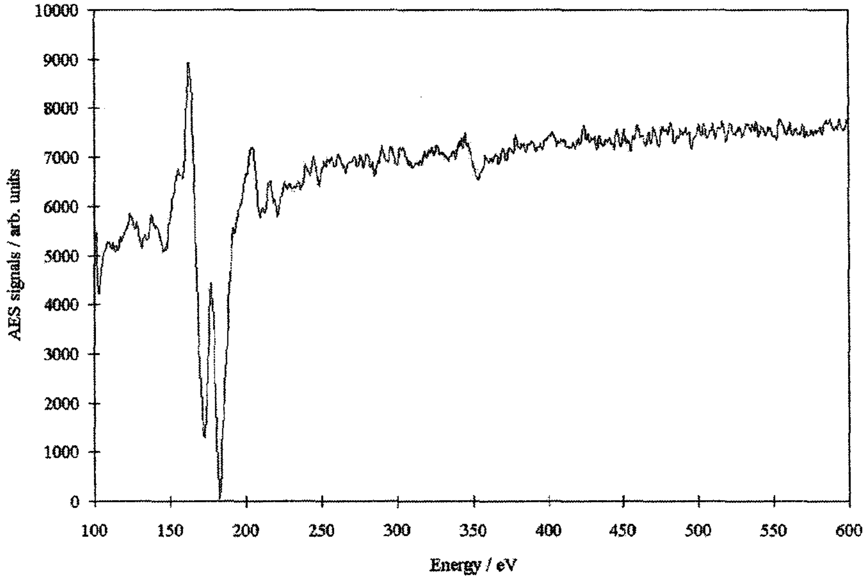

Figure 3-1 (a) An Auger electron spectrum displaying the W(NNN) peaks at 150-200 eV. The peak at ~350 eV is another W Auger transition. The sample is clean W(100).

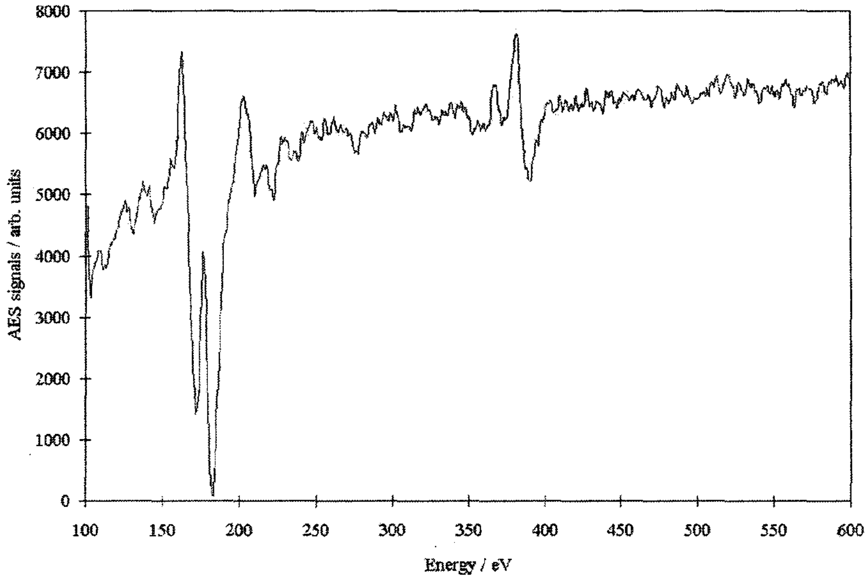

Figure 3-1 (b) An Auger electron spectrum displaying the W(NNN) peaks and the N(KLL) peak at 340-380 eV. The sample is W(100)-NH_3.

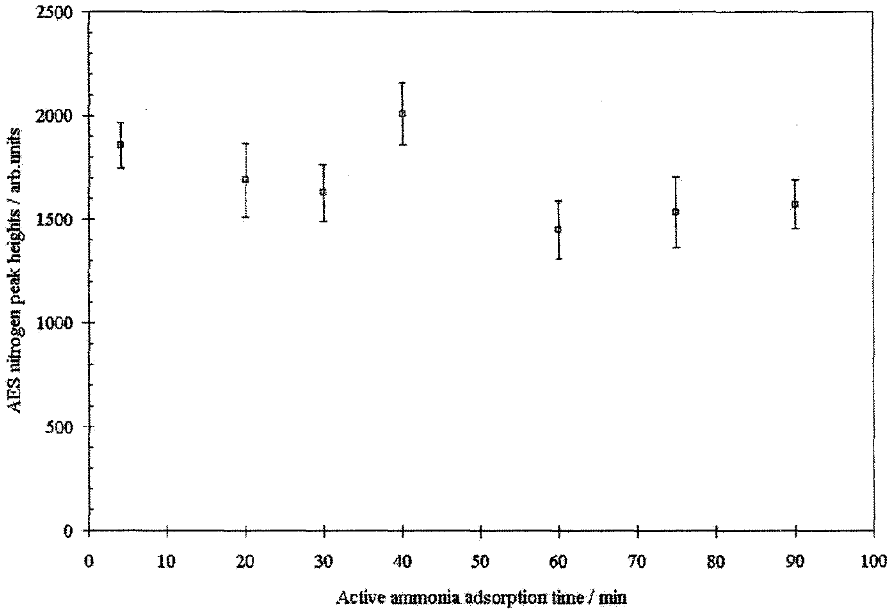

Figure 3-2 (a) The measured N(KLL) Auger peak heights *vs*. the active ammonia adsorption time on W(100) at room temperature. See text for experimental condition.

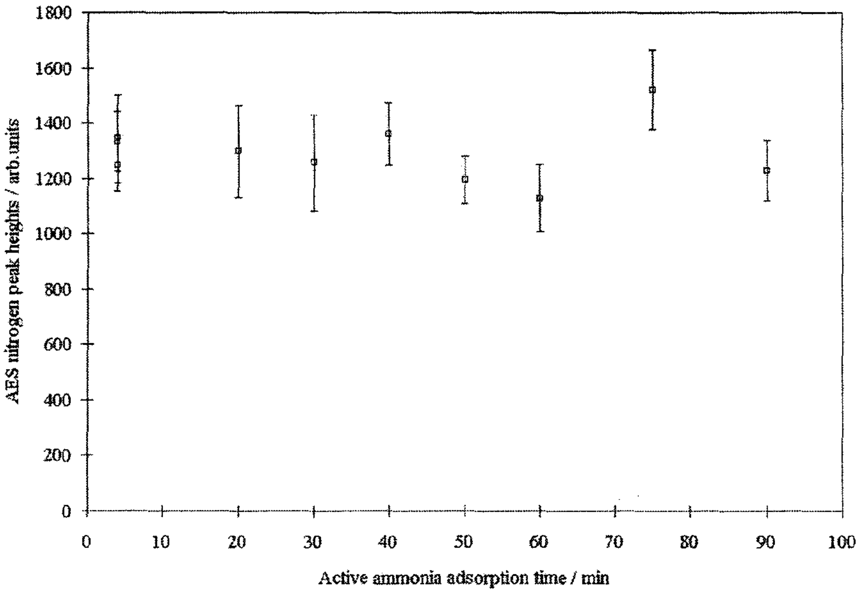

Figure 3-2 (b) The measured N(KLL) Auger peak heights *vs*. the active ammonia adsorption time on W(110) at room temperature. See text for experimental condition.

Crystal plane and crystal temperature	W_{NNN} AES peak size (arbitrary units)	N_{KLL} AES peak size (arbitrary units)	$\frac{N_{KLL}}{W_{NNN}}$ peak size ratio
W(100) @ 300 K	7970 ± 170 [1]	1680 ± 160	0.21 ± 0.03
500 K	8080 ± 190	1780 ± 190	0.22 ± 0.02
800 K	7880 ± 200	1890 ± 210	0.24 ± 0.03
W(110) @ 300 K	9110 ± 150	1290 ± 140	0.14 ± 0.02
500 K	8540 ± 230	1520 ± 200	0.18 ± 0.02
800 K	8890 ± 170	1430 ± 130	0.16 ± 0.01

Table 3-1 W(NNN) and N(KLL) AES peak sizes for the W(100) and W(110) surfaces after ammonia adsorption at room temperature, 500 and 800 K.

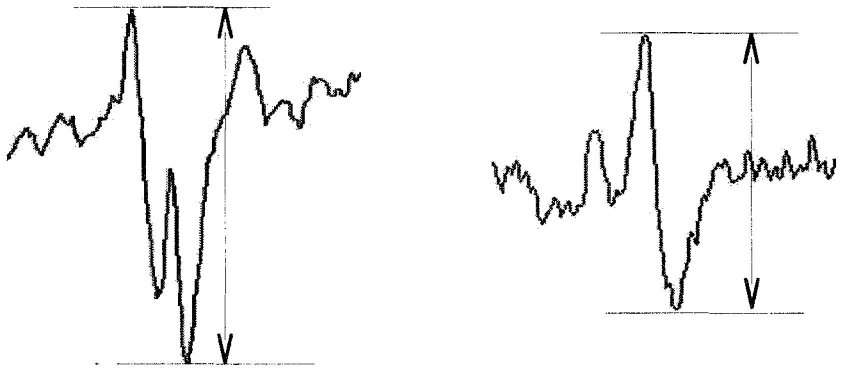
W(NNN) Auger peaks

N(KLL) Auger peaks

Figure 3-3 Peak heights definition for the W(NNN) peaks and the N(KLL) peaks.

3.3.2 Ground state adsorption at elevated crystal temperature

Adsorption of ammonia on the W(100) and W(110) surfaces was also investigated at elevated crystal temperatures of 500 and 800 K. The sample was heated and kept at the specified temperature by radiation heating at the back side as opposed to the front side that on which the gas beam impinged and AES analysis was performed. A stream of ammonia gas with a regulated gas flux (~10^{15} molecules cm^{-2} s^{-1}) was admitted with the

---

[1] The uncertainty was the standard deviation (σ_{n-1}) computed from no fewer than six measurements of the same Auger peak.

sample surface facing the gas orifice. After one to two hours of constant ammonia dosing at constant, elevated crystal temperature, the sample was rotated away from the gas orifice. Immediately the heater was switched off and the precision leak valve of the gas doser was closed. After the background pressure of ammonia was pumped down to 10^{-9} torr, Auger electron spectra were acquired from the sample surface to determine the nitrogen coverage resulting from the ammonia adsorption. The results are shown in table 3-1.

It is observed that the measured nitrogen AES signals increased slightly with crystal temperature. The increase is consistent with an increased rate of surface diffusion leading to an ammonia coverage (ground state adsorption) over a half monolayer. The observation will be discussed in section 6.4.1.

3.3.3 LEED observations

The surface symmetry of the clean sample surface and that with adsorbed ammonia were determined by LEED and recorded digitally. Both clean W(100) and W (110) surfaces show sharp (1×1) patterns, consistent with the substrate lattice symmetry (figure 3-4).

After ammonia adsorption at room temperature, the LEED patterns did not change significantly but the background became more diffuse, and streaks between beams were noted. The samples were then annealed at 600 K for 10 minutes in order to drive off the adsorbed hydrogen from the crystal surface. When the sample was cooled to room temperature, the resulting LEED patterns showed more visible streaks and a faint appearance of beams of fractional indices. In the W(100) experiment, the beams of fractional indices resembled a C(2×2) pattern, although the beams were not as sharp as previously reported [Estrup and Anderson 1968, Griffiths *et al.* 1982, Bessent *et al.* 1995]. The beams of fractional indices observed on the W(110) surface were also faint, and the symmetry patterns could not be definitively identified [Somerton and King 1979, Shamir *et al.* 1989].

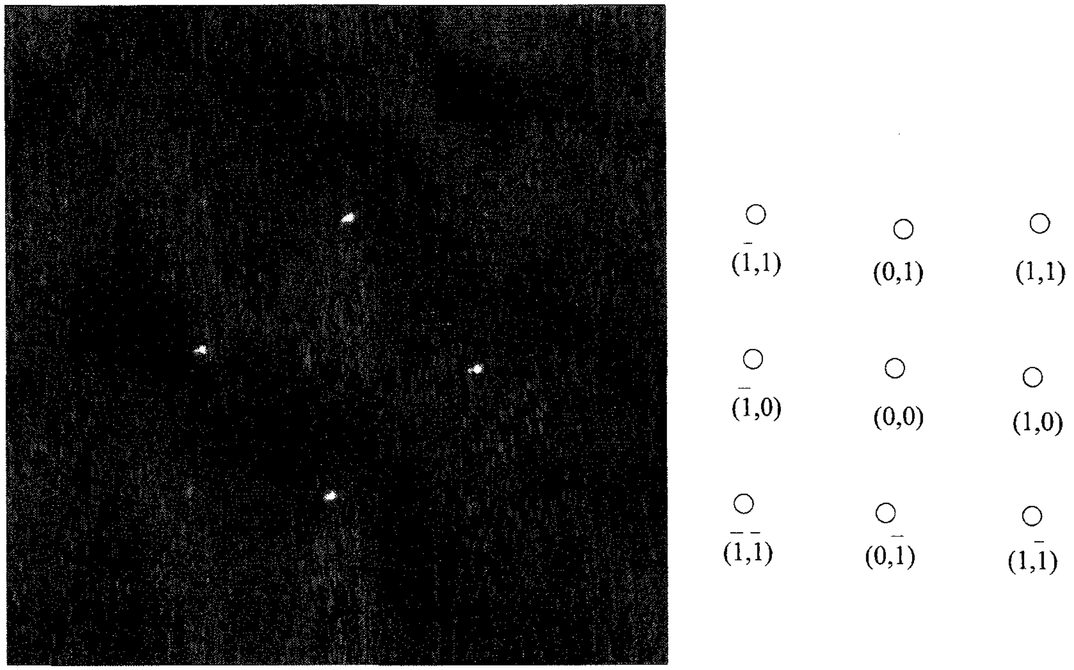

Figure 3-4 (a) LEED pattern of clean W(100) and its index. $E = 98$ eV.

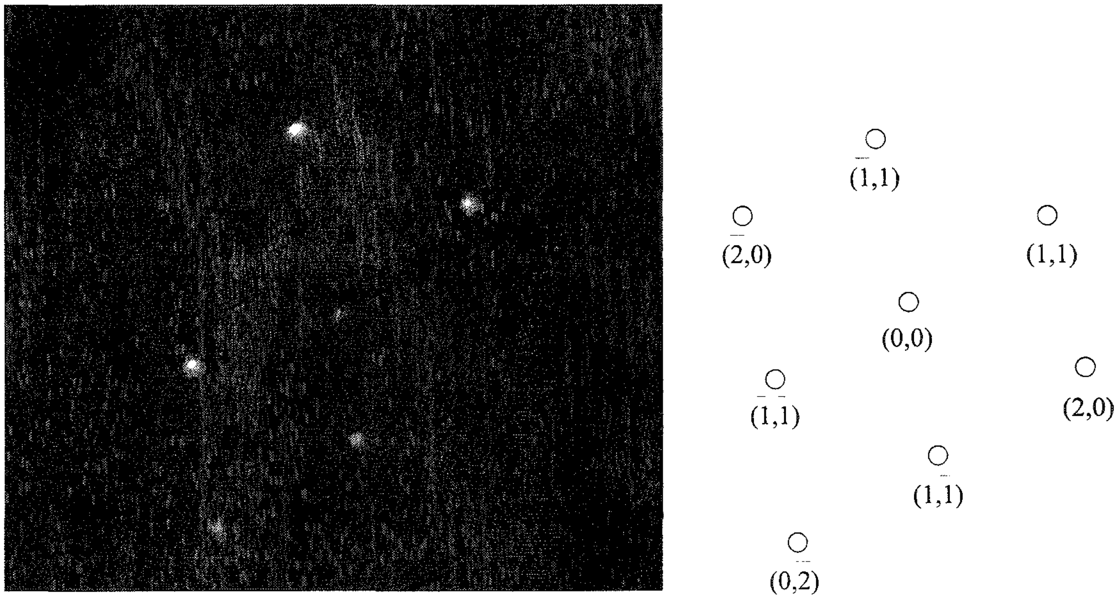

Figure 3-4 (b) LEED pattern of clean W(110) and its index. $E = 95$ eV.

The ammonia adsorbed on the W(100) and W(110) surfaces at 500 K both displayed faint beams of fractional indices on a diffuse background. Annealing at 600 K for 10 minutes did not make significant improvement in the quality of the LEED patterns.

Progressive annealing was also attempted on the two ground state ammonia adsorbed tungsten single crystal surfaces. Overlayer-underlayer transition of nitrogen adatoms (revealed by a characteristic LEED symmetry change, a P(4×1) pattern, and nitrogen AES signal change) was observed for W(100), in agreement with the results reported by Chen [1996]. On W(110), however, there was no observable change in nitrogen AES signal up to 900 K. There was a change in the LEED symmetry pattern: from the faint P(1×1) at 300 K after ammonia adsorption to a complicated P(4√2×4√2)-R90° (or C(4×8)) symmetry, which started to appear at ~650 K and faded after 900 K. No substrate surface reconstruction, adsorbate overlayer surface structure or even adsorption coverage has yet been found to fit the observed LEED pattern. The new LEED patterns, after ammonia adsorption and subsequent annealing, are shown in figures 3-5 and 3-6.

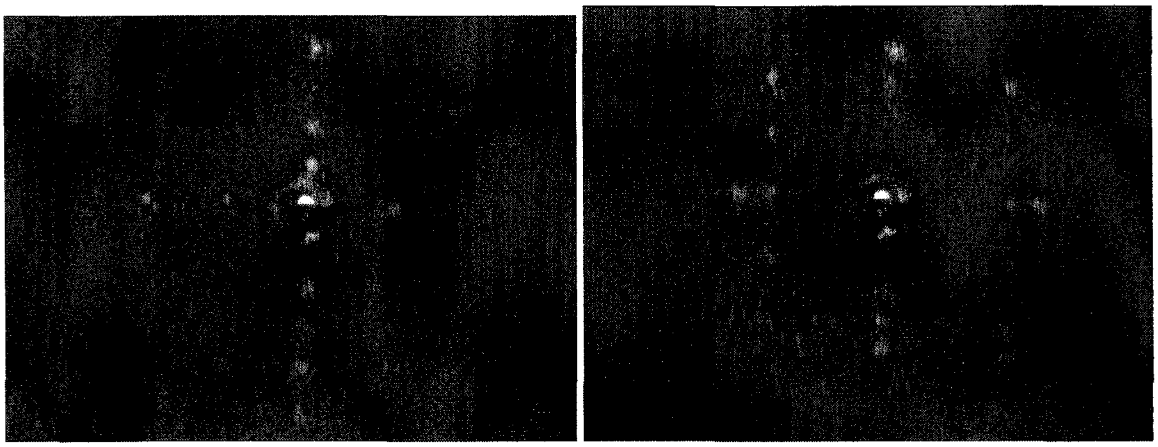

(a) $E = 38$ eV (b) $E = 70$ eV

Figure 3-5 LEED patterns of W(100) / NH_3 displaying the P(4×1) symmetry. The half covered surface has been annealed to 750 K for 10 minutes.

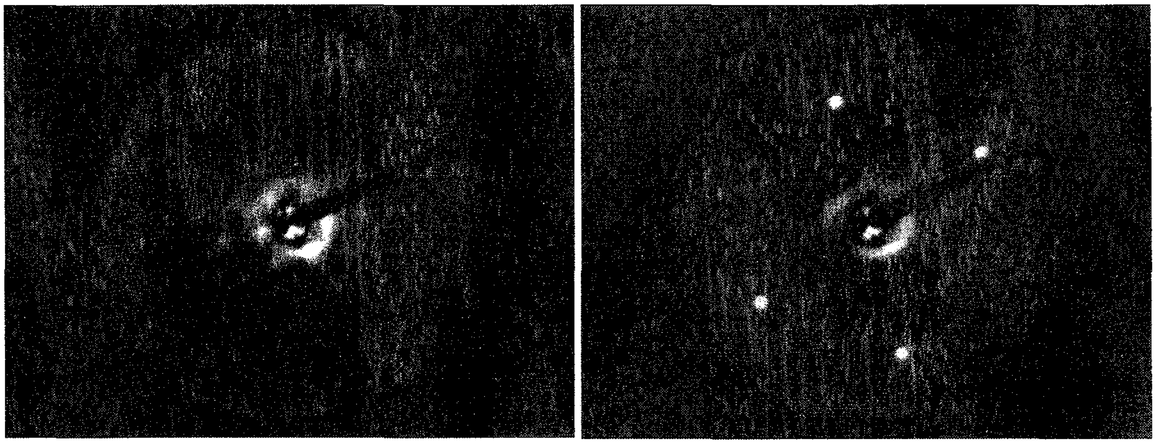

(a) $E = 33$ eV (b) $E = 89$ eV

Figure 3-6 LEED patterns of W(110) / NH_3 displaying the P(4√2×4√2)-R90° symmetry. The half covered surface has been annealed to 850 K for 10 minutes.

3.4 DISCUSSION

The ammonia adsorption behaviour on the W(100) and W(110) surfaces at 300 K are similar to those previously reported for the two crystal orientations [Estrup and Anderson 1968, Reed and Lambert 1984, Alnot *et al.* 1989, Masson *et al.* 1995] and on polycrystalline tungsten samples [Peng and Dawson 1971, Dawson 1974, Shindo *et al.* 1980, Egawa *et al.* 1981]. The saturation nitrogen uptake on W(100) at room temperature following ammonia adsorption is believed to be a half-monolayer coverage. The coverage determination is deduced from previous published results of the N_2 and H_2 thermal desorption mass spectrometry and a characteristic C(2×2) LEED pattern [Estrup and Anderson 1968, Egelhoff *et al.* 1976, Egawa *et al.* 1983].

At 300 K, there is no report of appreciable amount of bulk diffusion of nitrogen atoms, and therefore the nitrogen adatoms were believed to be all located on the topmost layer of the substrate surface.

The AES results of the ground state ammonia adsorption experiments at elevated crystal temperatures generally agreed with the results of Chen [1996]. Comparison of the AES data generated by the normal incidence and the glancing incidence (75° off-normal) electron guns led to the conclusion that on W(100), the nitrogen adatom underwent a transition to a sub-surface region in the temperature range 650 to 820 K. There was an overlayer-underlayer transition of the nitrogen adatoms, probably with a reconstruction of the substrate surface.

The AES data on W(110) revealed, unlike those on W(100), the nitrogen adatom only partially diffused toward the bulk upon annealing [Chen 1996]. The same analyses of comparing the AES signals generated by the normal incidence and the glancing incidence electron beam implied the tungsten atoms on W(110) are more heavily covered than on W(100). Chen proposed this result could be interpreted as only some of the adsorbed nitrogen diffused underneath upon annealing, while the remainder stayed on the topmost layer. In fact, in the N/W(110) system the nitrogen atoms were described as being “partially sandwiched” into the underlayers by Somerton and King [1979].

3.5 CONCLUSION

In this chapter the basic results of the ground state adsorption of ammonia on W (100) and W(110) were presented. The adsorption is a dissociative process in which the NH_3 molecule is torn apart and the fragments NH_2 and H are individually adsorbed on the crystal surfaces. At or above room temperature there is no report of molecular chemisorption of ammonia. The chemisorption only proceeds in a dissociative manner. The adsorbates are NH_2, or if further dissociated, NH or N.

The saturated coverage of ammonia via this ground state adsorption is a half-monolayer on W(100). Since the dissociation process involves the participation of a pair of neighbour vacant surface sites, the statistical maximum coverage is limited to only one ammonia adsorption for every pair of surface sites. No such pair of neighbour vacant sites is available once the adsorption reached half-monolayer coverage. This is a fundamental result for the subsequent understanding of the processes which lead to saturation ammonia coverage.

CHAPTER FOUR

ELECTRON STIMULATED ADSORPTION OF AMMONIA

4.1 INTRODUCTION

In this chapter the effect of electron irradiation on the crystal surface during ammonia adsorption is presented. A discussion of the general procedure for an electron stimulated ammonia adsorption experiment on W(100) or W(110) will be discussed. The data collected for the kinetics investigation, primarily the time-dependence of the nitrogen coverage on the sample surface, will be analyzed. The key parameters valuable for the study will be emphasized and their interpretation in the ammonia adsorption scheme will be defined.

4.2 EXPERIMENTAL METHOD

The adsorption experiments were designed so that the electron beam serves two purposes simultaneously, both the electrons for the stimulated ammonia adsorption process and the primary electrons for AES surface composition determination.

The tungsten single crystal sample was first flashed to 2200 - 2600 K to desorb any background contaminant adsorption. Its surface cleanliness was checked with AES after the crystal temperature had fallen to room temperature again. Flash cleaning was repeated until no contaminants were observed in the AES spectrum. The sample was then kept in front of the electron gun. An electron bombardment heater at the back of the single crystal could be used to maintain the sample at a temperature higher than room temperature.

The filament in the electron gun was properly degassed and kept at the AES standard operating current of 25.0 μA, with a shutter closed to avoid electron irradiation of the crystal prematurely. With the poppet valve adjusted to limit the pumping and prevent the displacement-desorption of gases from the ion pumps due to pumping large amounts of ammonia, ammonia was leaked into the vacuum chamber via the leak valve. The single crystal faced the AES optics, away from the opening. The leak valve opening was continuously adjusted to fill the vacuum chamber to the designated pressure rapidly and then to keep a constant pressure dynamically. The ammonia partial pressure and the gas composition in the vacuum chamber were continuously monitored by the residual gas analyzer. Even though ammonia is sticky and its pressure response is slow, care was taken to avoid overfilling ammonia into the vacuum chamber. Neither the single crystal nor the residual gas analyzer faced the gas doser directly. The ammonia pressure measured thus is believed to be the homogeneous ammonia pressure perceived by the crystal. The ammonia filling procedure up to the designated pressure generally took a few minutes.

With the crystal temperature and the ammonia pressure in the vacuum chamber stabilized, the electron gun shutter was opened and a timer started simultaneously. The surface composition was then continuously monitored by AES and the measured peak heights of the tungsten and nitrogen peaks were plotted against the electron irradiation time (figure 4-1 for W(100) and 4-2 for W(110)). The important features of a typical nitrogen AES signal evolution graph are discussed in the next section.

The adsorption experiment was complete when the recorded nitrogen AES signals stopped changing with the electron irradiation time. Then, the electron gun shutter was closed, the leak valve for ammonia gas dosing was closed and the poppet valve fully opened to resume maximum pumping in the vacuum chamber.

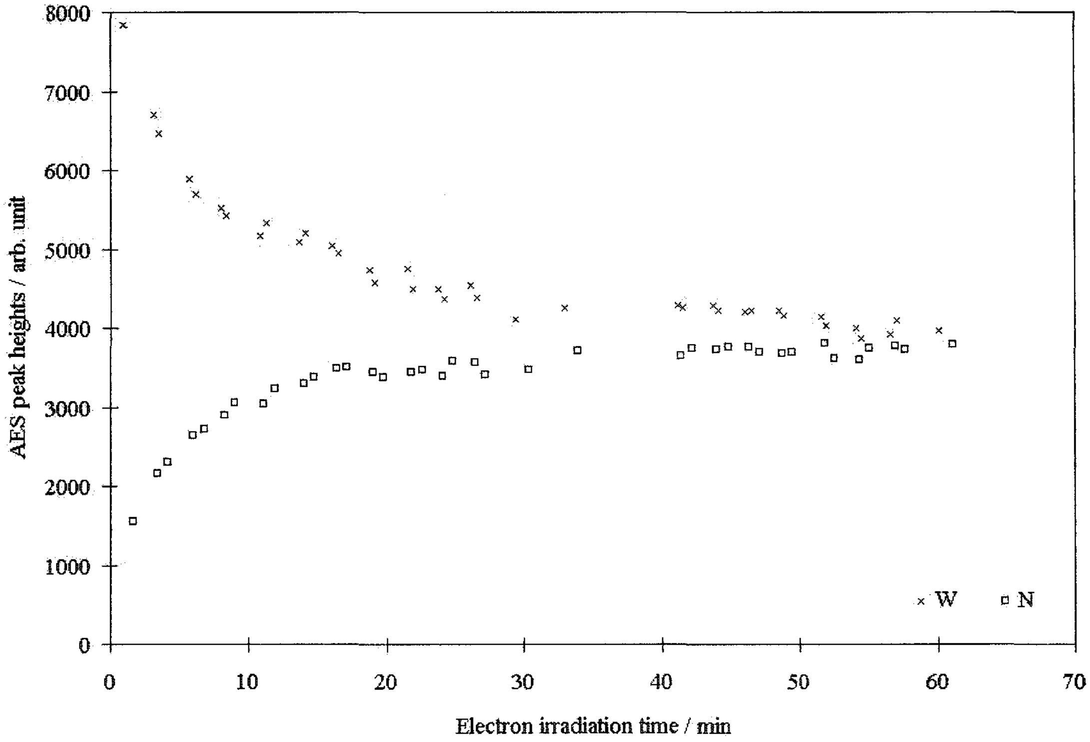

Figure 4-1 A typical AES signal evolution graph is shown for W(100) at room temperature with 5.0×10^{-7} Torr ammonia pressure, and normal incidence electrons at 2.0 keV and 25.0 μA.

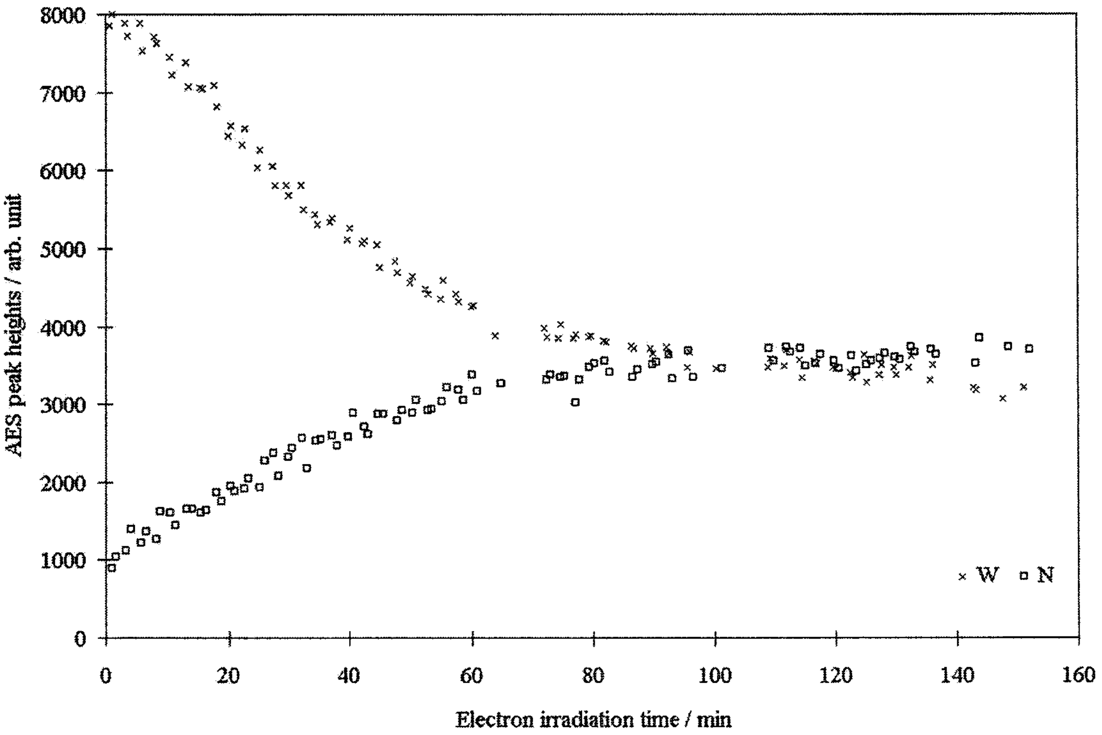

Figure 4-2 A typical AES signal evolution graph is shown for W(110) at room temperature with 5.0×10^{-7} Torr ammonia pressure, and normal incidence electrons at 2.0 keV and 25.0 μA.

4.3 KEY INFORMATION IN A NITROGEN AES SIGNAL EVOLUTION GRAPH

In figures 4-1 and 4-2 the increase of nitrogen AES signal as ammonia is adsorbed and the corresponding decrease of the W AES signals with electron irradiation time are displayed. The tungsten AES signal decrease is a result of the substrate surface getting covered by ammonia. The tungsten atoms become second layer atoms and the Auger electron signal is attenuated. The W AES signal decrease reflects the increase of the nitrogen AES signal.

Important features of the evolution graphs are the ground state ammonia coverage at time zero; the nitrogen saturation coverage; and the initial rate of nitrogen AES signal increase. They are shown in figure 4-3 and will now be discussed in detail.

4.3.1 Ground state ammonia adsorption coverage at time zero

The back-extrapolated *y*-intercept of the nitrogen AES signal evolution graph (figure 4-3) is not zero at the beginning of the adsorption experiment. The measured signal is understood as the coverage of ammonia adsorbed onto the crystal sample during the few minutes of exposure when the vacuum chamber is being filled with ammonia. The shutter of the electron gun is closed when ammonia is filling into the vacuum chamber. The crystal sample is exposed to ammonia without electron irradiation at that time and thus it is ground state ammonia adsorption. The ground state ammonia coverage is therefore represented by the *y*- intercept in the nitrogen AES signal evolution graph, at the zero time of electron irradiation.

The value observed for this intercept is indeed consistent with the value observed for ground state adsorption in chapter three.

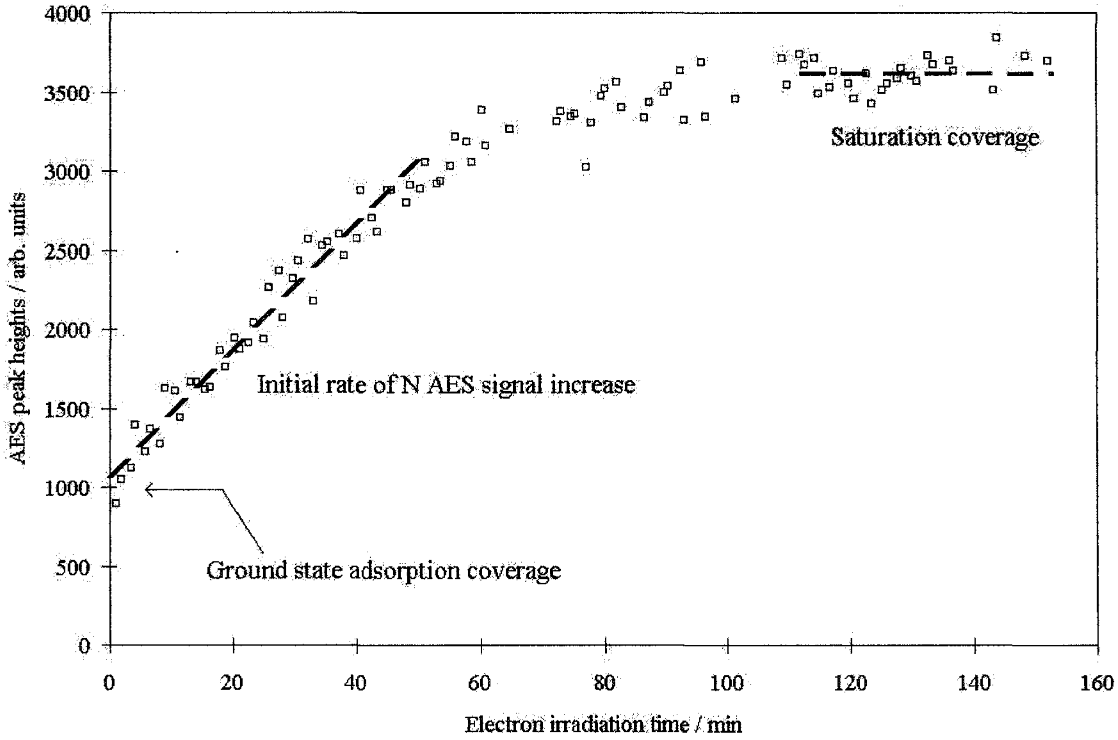

Figure 4-3 The N AES signal data of the evolution graph in figure 4-2.

4.3.2 Saturation coverage of ammonia

The saturation coverage of ammonia refers to the maximum surface concentration of ammonia the crystal surface can accommodate. Saturation is represented by the final maximum nitrogen AES signals measured at the end of the stimulated ammonia adsorption experiments (figure 4-3). At the completion of the adsorption process, the nitrogen AES signals stop increasing with the electron irradiation time and remain at a constant level between 3600 - 4000 units (at room temperature). This is referred to as a full monolayer of nitrogen. Upon prolonged electron stimulation, it is thought the dissociatively adsorbed ammonia has completely degraded to bare nitrogen adatoms. Griffiths *et al.* [1982] reported nitrogen adatoms adsorb on the four-fold hollow sites on W(100), and the coverage thus represents a nitrogen surface concentration of 1.0×10^{15} atoms cm^{-2}.

LEED studies for saturated ammonia adsorbed on the W(100) and W(110) surfaces at 500 K both displayed faint fractional beams on a diffuse background. Annealing at 600 K for 10 minutes did not make significant improvement in the quality of the LEED patterns.

4.3.3 Initial rate of nitrogen AES signal increase

The determination of the ammonia adsorption rate is the most important one in the investigation of the adsorption kinetics. In this project, the ammonia coverage is measured by AES, therefore the rate of the nitrogen AES signal increase is interpreted as the ammonia adsorption rate. The initial rate of stimulated ammonia adsorption, ν, is thus defined as the rate of change of the nitrogen AES signal over a period of electron irradiation time at the beginning of the adsorption experiment.

$$\nu = \frac{\Delta \text{ signal}}{\Delta \text{ time}} \qquad \ldots (4\text{-}1)$$

Throughout the thesis, this adsorption rate is reported as arbitrary units of AES signal per minute irradiation time (*i.e.*, arb. units per min.)

Referring to the nitrogen AES signal evolution graph in figure 4-3, typical of many others shown in later chapters, it is observed generally that the nitrogen AES signal, or the ammonia coverage, increases linearly with the electron irradiation time. While the linearity makes the defined adsorption rate determination much simplified, it is in contradiction with the usual behaviour in which the adsorption rate decreases with increasing coverage as the number of available sites decreases. Thus in a simple example this follows a $(1-\theta)$ dependence, where θ is the fractional coverage of the adsorbate. Adsorption starts when a gas molecule arrives at the substrate surface. If the gas molecule lands on an appropriate surface site, a significant interaction is developed between the two. So adsorption is accompanied by occupation of vacant surface sites. The adsorption rate therefore decreases, typically in a $(1-\theta)$ or $(1-\theta)^2$ fashion, for non-dissociative and dissociative adsorption respectively. The coverage-independence of the adsorption rate is certainly worthy of investigation.

4.4 PROJECT DEVELOPMENT

The important parameters in the investigation of the electron stimulated ammonia adsorption kinetics have been discussed. They are acquired from the nitrogen AES signal evolution graphs during the adsorption in different experimental conditions. In the following chapters the dependence of the stimulated adsorption rate on each experimental variable will be studied individually. These controlled parameters will now be introduced.

The general scheme for the electron stimulated adsorption of ammonia onto a tungsten surface site, *, can be expressed as in equation 4-2:

$$NH_3(g) + * + e \rightarrow \underset{*}{N}H_3(a) + e \qquad \ldots (4\text{-}2)$$

From this equation it is understandable that the investigation should cover the dependence of the stimulated ammonia adsorption rate on the concentration of the various species involved in the process: the ammonia gas pressure, the surface coverage (the concentration of available surface sites) and the electron beam current density. The temperature of the crystal surface and the orientation of the electron beam relative to the surface are expected to play important roles in the kinetics of the reaction too. The effect of each experimental controllable is examined in the following chapters:

(a) The effect of the ammonia gas pressure, in chapter five;
(b) The effect of the temperature of the crystal surface, in chapter six;
(c) The effect of the electron beam current density, in chapter seven; and
(d) The effect of the incident angle of the electron beam relative to the surface, in chapter eight.

CHAPTER FIVE

AMMONIA PRESSURE EFFECTS ON THE KINETICS OF THE STIMULATED AMMONIA ADSORPTION

5.1 INTRODUCTION

The collision frequency of ammonia molecules with the surface,

$$Z = \frac{P}{\sqrt{2\pi mkT}}\ , \qquad \ldots\ (5\text{-}1)$$

is proportional to the ammonia pressure (P). This collision frequency can directly affect the rate of adsorption of ammonia (ν_{ads}),

$$\nu_{ads} = k_{ad}\, P\, S\, (1\text{-}\theta), \qquad \ldots\ (5\text{-}2)$$

where in this simplified equation, k_{ad} is the adsorption rate constant, S is the sticking probability of ammonia and (1-θ) is the probability that an adsorption site is vacant.

In the electron stimulated adsorption of ammonia, the gas phase ammonia molecules must first become adsorbed onto the surface before they get a chance to be stimulated by electron irradiation. The probability of having a gas phase ammonia molecule reaching a vacant surface site and simultaneously be stimulated by an incident electron is negligibly small. The scenario resembles a tri-particle reaction (electron, ammonia molecule and a vacant site). The reversible pre-adsorption of ammonia molecules followed by electron stimulation is therefore a more reasonable Rideal-Eley bimolecular mechanism.

Electron stimulation of gas phase ammonia molecules, followed by the adsorption of the excited molecules, has been ruled out from making a contribution to the stimulated adsorption [Ermrich 1965, Chen 1996]. Hence the concentration of ammonia molecules which are non-permanently adsorbed has a major role in determining the rate of electron stimulated adsorption of ammonia on our tungsten single crystal surfaces.

In this chapter, the effects of the ammonia pressure on the electron stimulated ammonia adsorption on W(100) and W(110) will be described. The coverage-independence of the adsorption rate will be discussed and an adsorption model involving the concept of ESA active sites and chemisorption sites will be introduced.

5.2 EXPERIMENTAL PROCEDURES

Electron stimulated ammonia adsorption experiments at various ammonia pressures were conducted. The clean crystal sample, at room temperature, was positioned in front of the electron gun with the shutter closed. Ammonia was back-filled into the vacuum chamber from the leak valve to a specific ammonia pressure, which was measured by QMS. When the designated ammonia pressure was reached, the shutter of the electron gun was opened. Immediately the crystal sample was irradiated with an electron beam of 25.0 μA current in the ammonia environment and the electron stimulated adsorption of ammonia began.

The surface composition was continuously monitored by AES and the measured nitrogen and tungsten AES signals were recorded. These data were plotted against the electron irradiation time in an AES signal evolution graph. During the experiment the gas composition in the vacuum chamber was continuously monitored to determine if contaminants (oxygen, carbon oxides or water vapour) were getting into the chamber along with the ammonia gas flux. The adsorption experiment was terminated when the nitrogen and tungsten AES signals stopped changing with electron irradiation time for an extended period, which indicated the achievement of saturated coverage.

5.3 RESULTS

The nitrogen AES signal evolution graphs acquired for stimulated ammonia adsorption experiments at room temperature and different ammonia pressures are shown in figure 5-1 for W(100) and figure 5-2 for W(110). The coverage-independent initial nitrogen AES signal increase can be seen in these graphs. The values of the ground state adsorption ammonia coverage, the stimulated adsorption saturation coverage, and the adsorption rate are summarized in tables 5-1 and 5-2 for the W(100) and W(110) stimulated adsorption experiments respectively.

The coverage by ground state ammonia adsorption, revealed by the AES signal intercept at zero electron irradiation time, did not suggest a relationship with the ammonia pressure. The final saturation nitrogen AES signals were also not dependent on the ammonia pressure in the stimulated ammonia adsorption experiments. The ground state and saturation coverages were similar for all the experiments for a variation in pressure over more than two orders of magnitude for W(110). However, the rate of electron stimulated ammonia adsorption did show pressure dependence.

Figures 5-1 N AES signal evolution graphs of electron stimulated ammonia adsorption experiments on W(100) at room temperature and different ammonia gas pressure: (a) 1.0×10^{-7} torr, (b) 7.5×10^{-8} torr, (c) 5.0×10^{-8} torr, (d) 3.5×10^{-8} torr, (e) 2.0×10^{-8} torr, (f) 1.0×10^{-8} torr, and (g) 5.0×10^{-9} torr. The electron beam is at normal incidence, of beam energy 2.0 keV and beam current 25.0 μA.

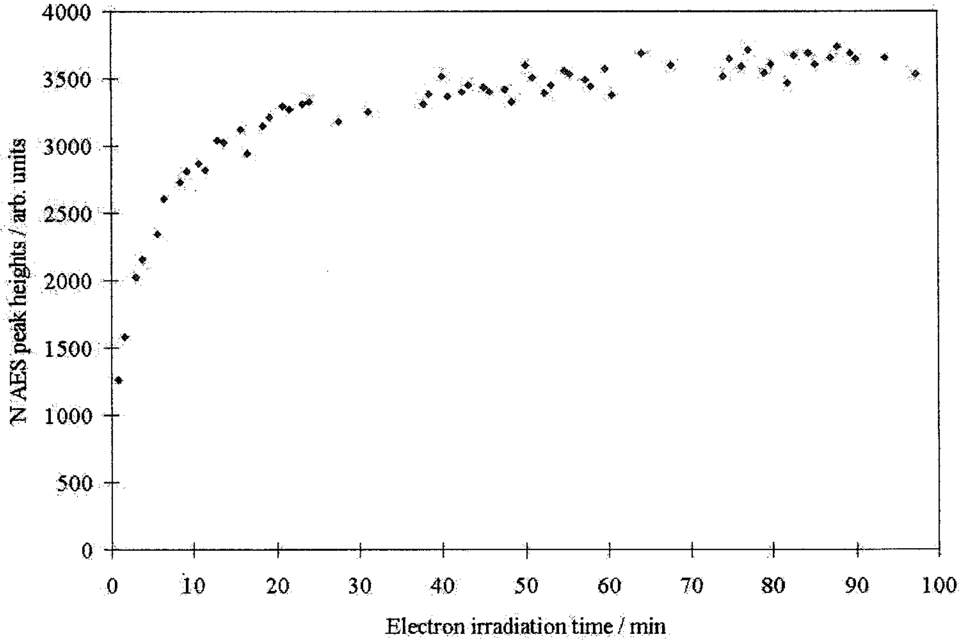

Figure 5-1(a) P(NH_3) = 1.0×10^{-7} torr.

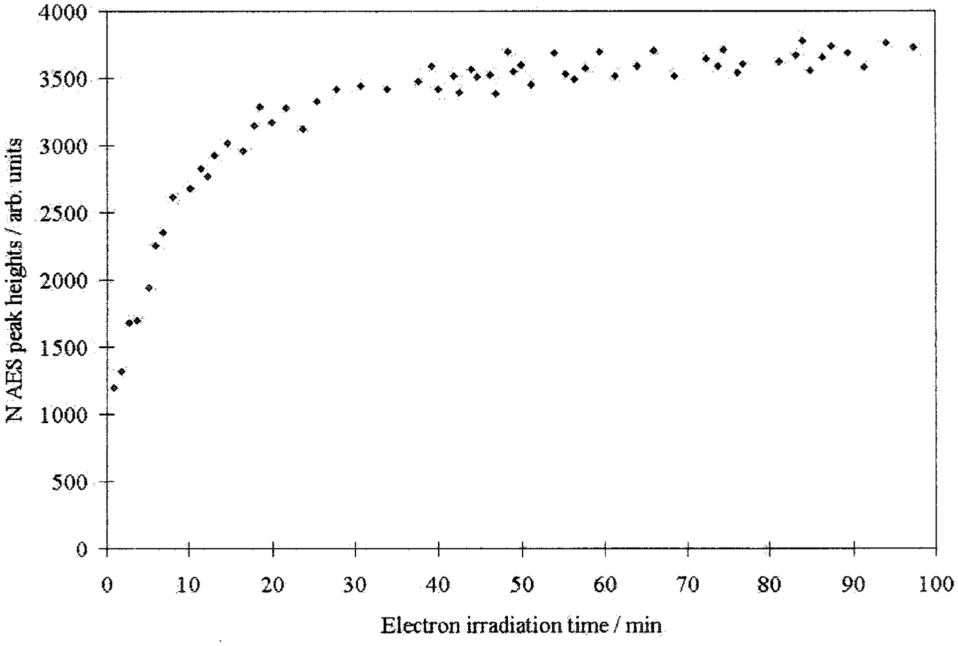

Figure 5-1(b) P(NH_3) = 7.5×10^{-8} torr.

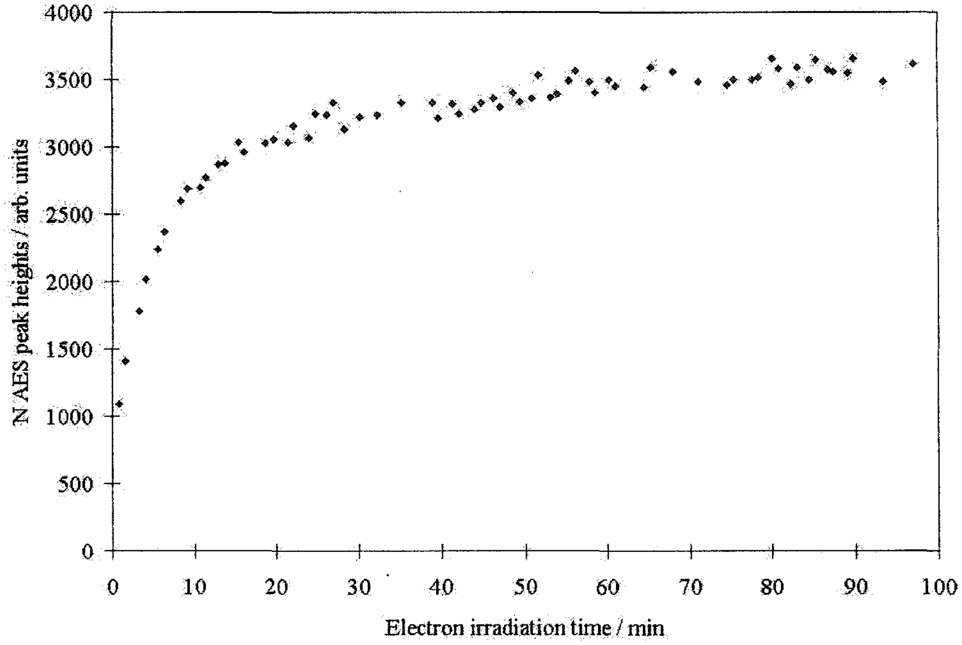

Figure 5-1(c) P(NH_3) = 5.0×10^{-8} torr.

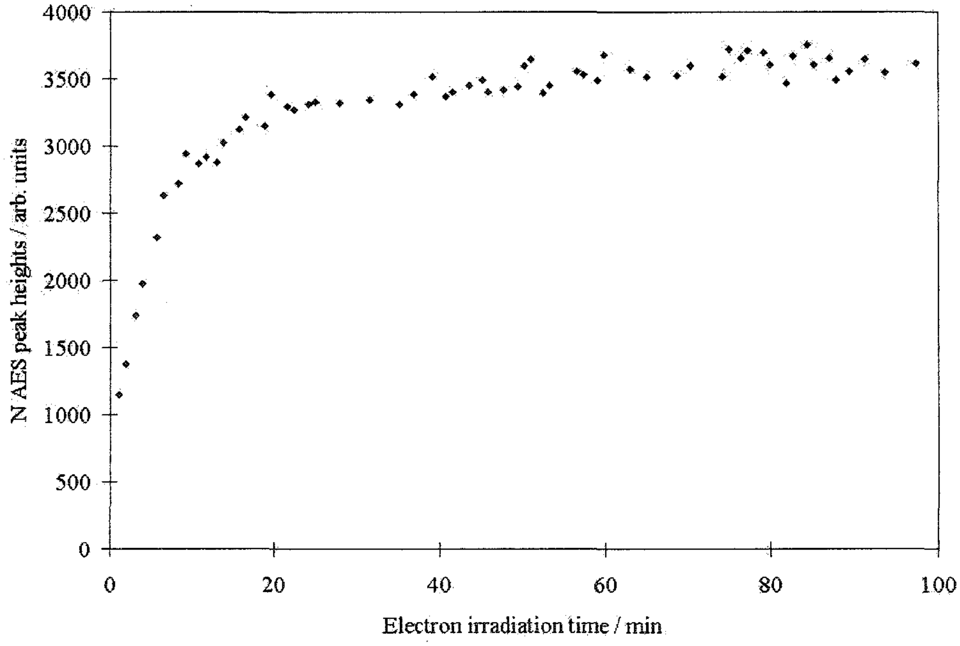

Figure 5-1(d) P(NH_3) = 3.5×10^{-8} torr.

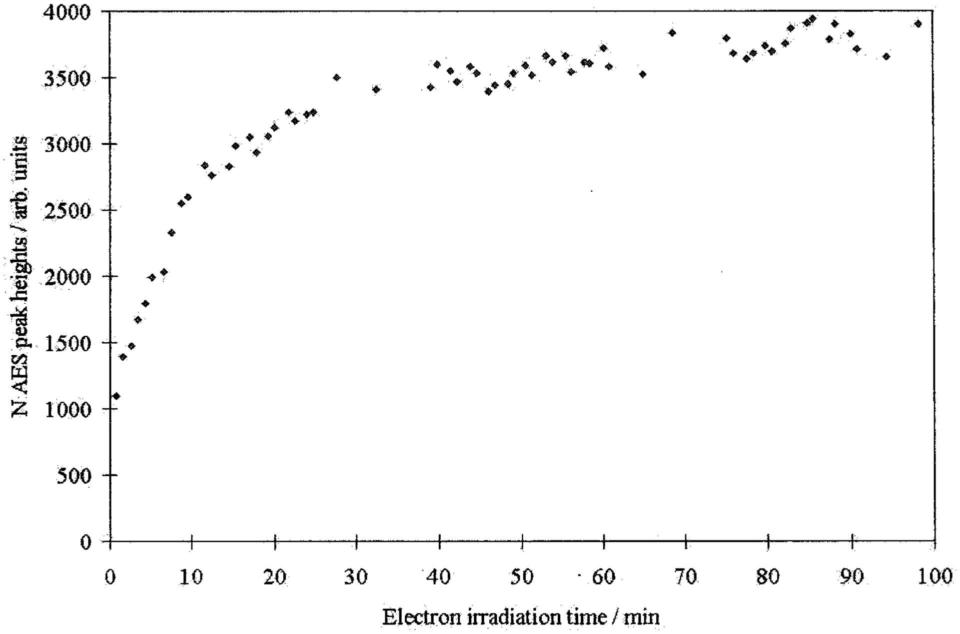

Figure 5-1(e) P(NH_3) = 2.0×10^{-8} torr.

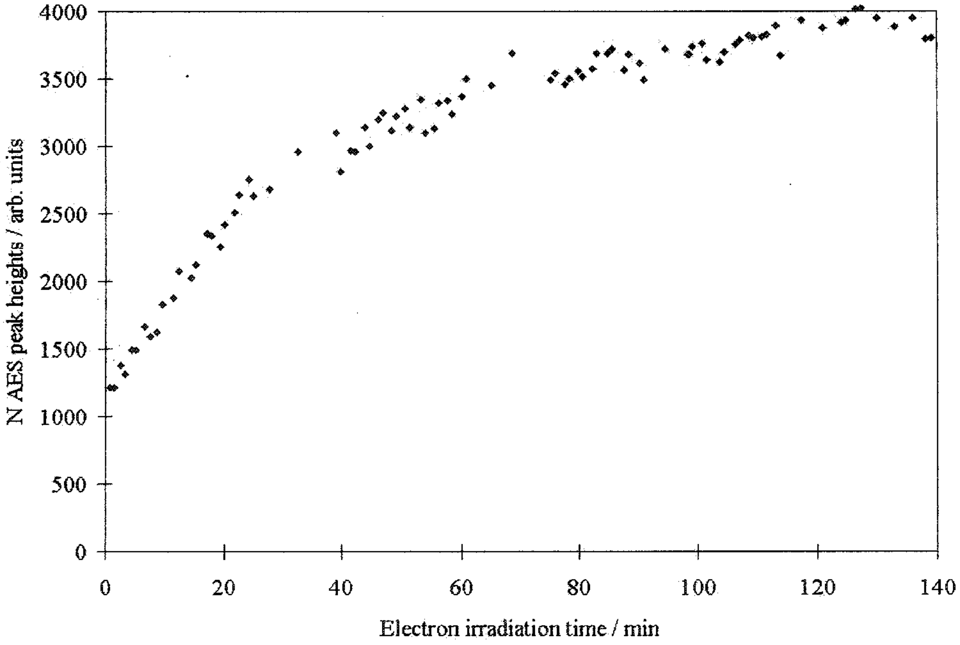

Figure 5-1(f) P(NH_3) = 1.0×10^{-8} torr.

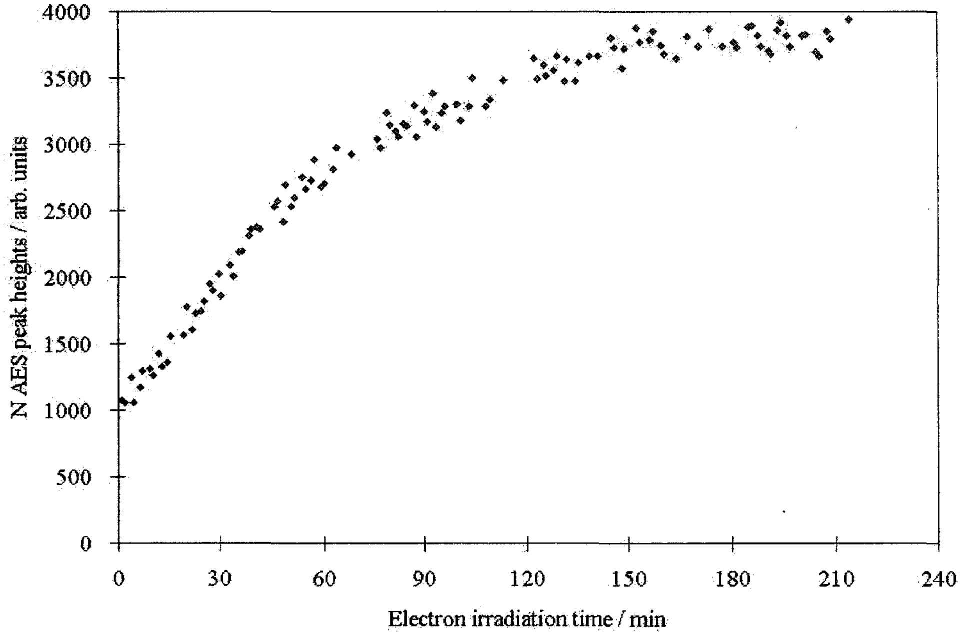

Figure 5-1(g) $P(NH_3) = 5.0\times10^{-9}$ torr.

Figures 5-2 N AES signal evolution graphs of electron stimulated ammonia adsorption experiments on W(110) at room temperature and different ammonia gas pressures: (a) 5.0×10^{-7} torr, (b) 3.0×10^{-7} torr, (c) 1.0×10^{-7} torr, (d) 7.0×10^{-8} torr, (e) 3.0×10^{-8} torr, (f) 1.5×10^{-8} torr, (g) 5.0×10^{-9} torr, and (h) 1.7×10^{-9} torr. The electron beam is at normal incidence, of beam energy 2.0 keV and beam current 25.0 μA.

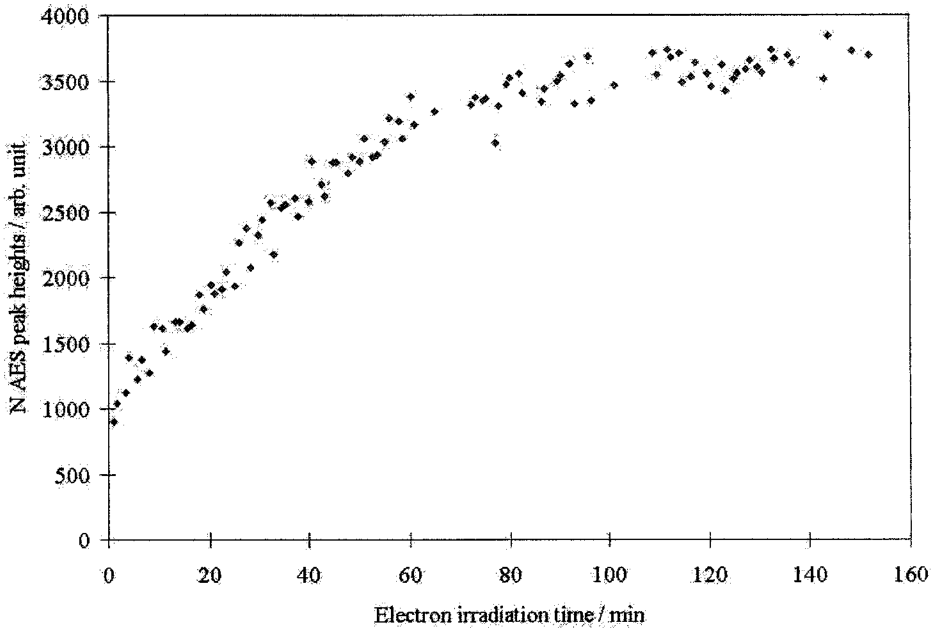

Figure 5-2(a) $P(NH_3) = 5.0\times10^{-7}$ torr.

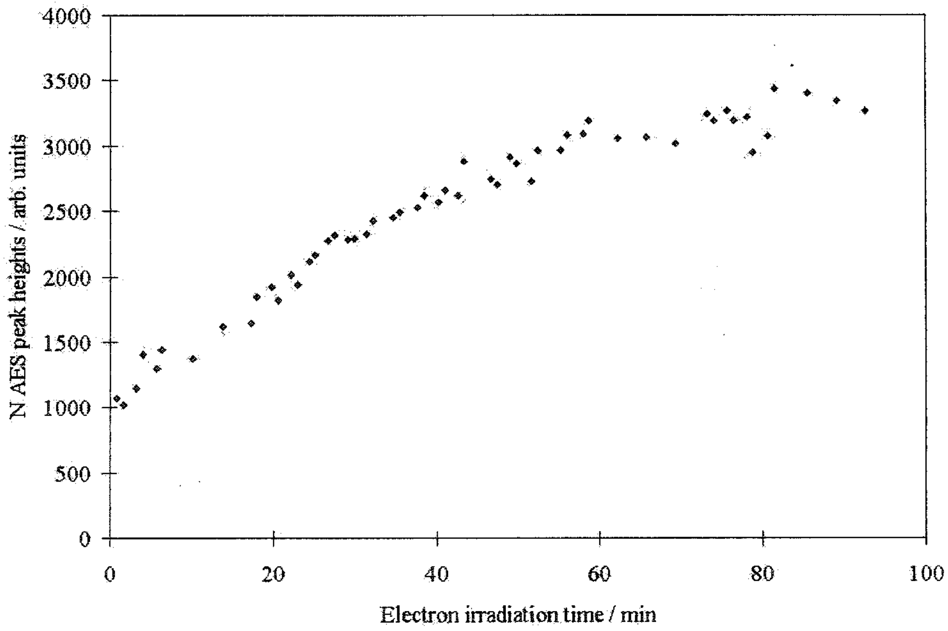

Figure 5-2(b) $P(NH_3) = 3.0\times10^{-7}$ torr.

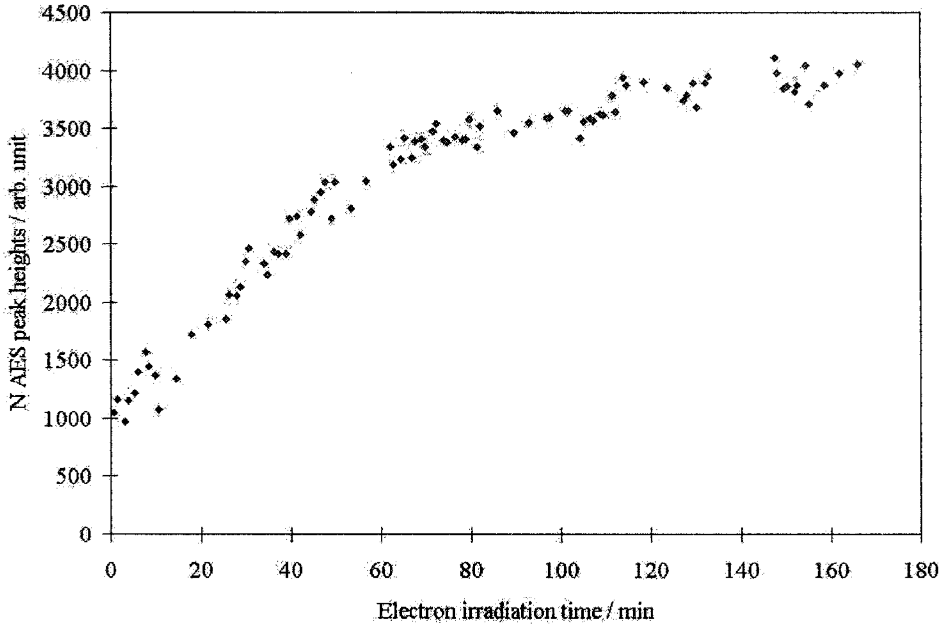

Figure 5-2(c) P(NH_3) = 1.0×10^{-7} torr.

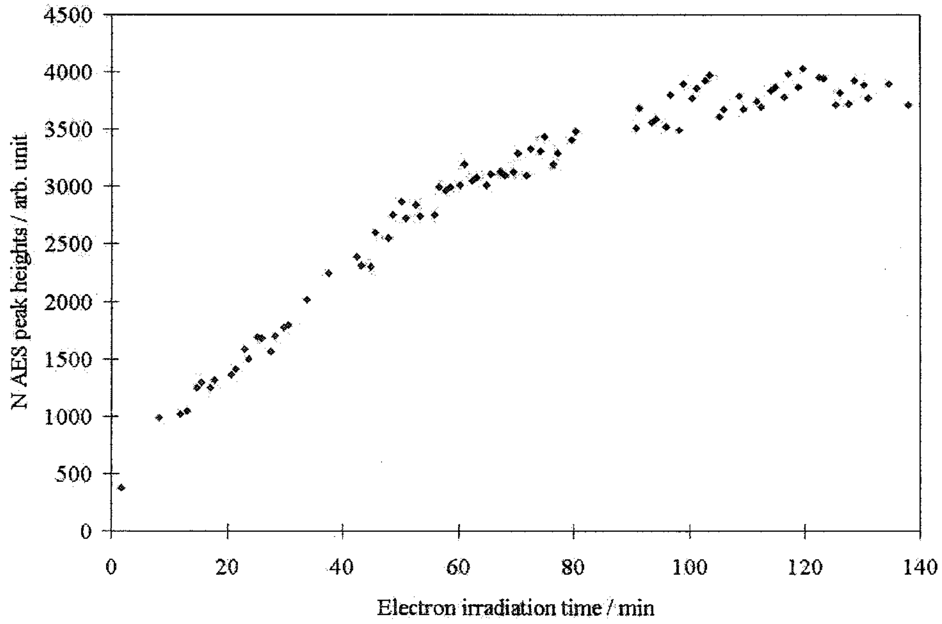

Figure 5-2(d) P(NH_3) = 7.0×10^{-8} torr.

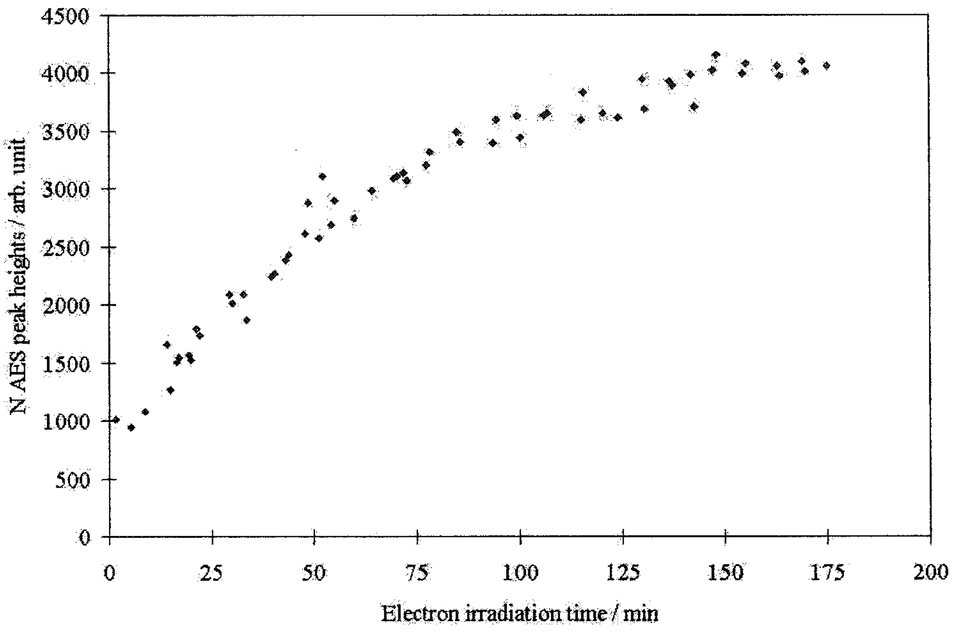

Figure 5-2(e) $P(NH_3) = 3.0\times10^{-8}$ torr.

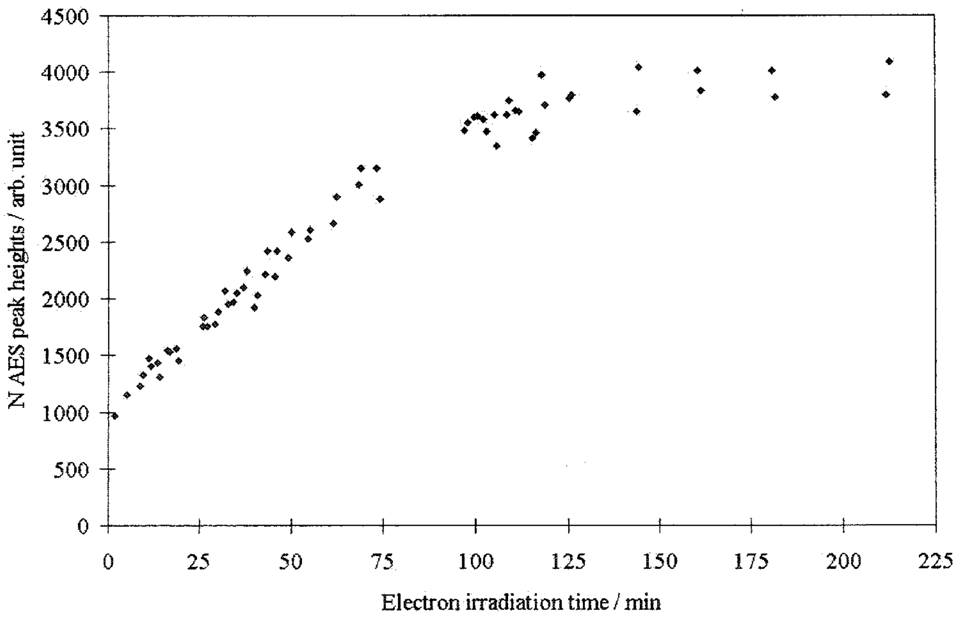

Figure 5-2(f) $P(NH_3) = 1.5\times10^{-8}$ torr.

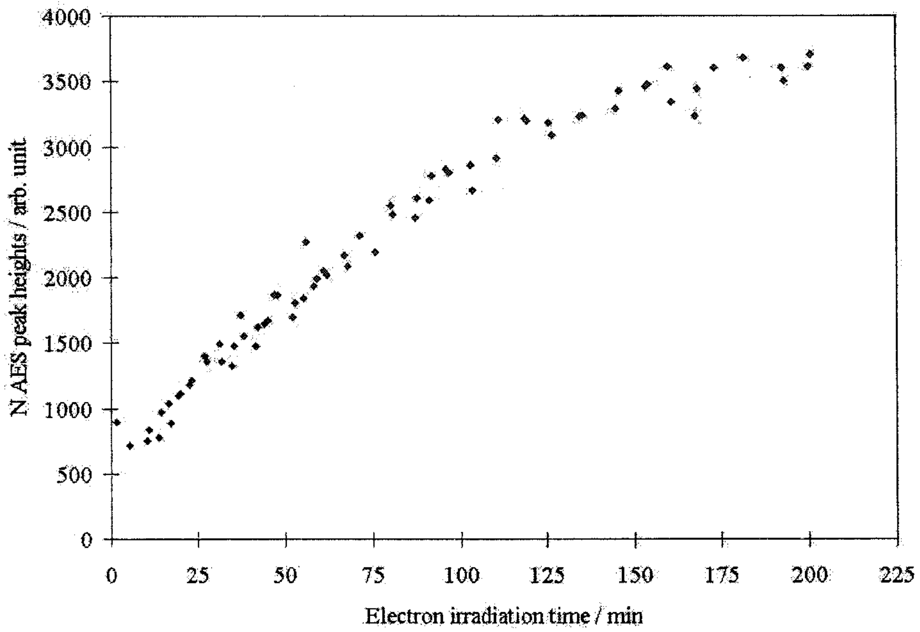

Figure 5-2(g) P(NH_3) = 5.0×10^{-9} torr.

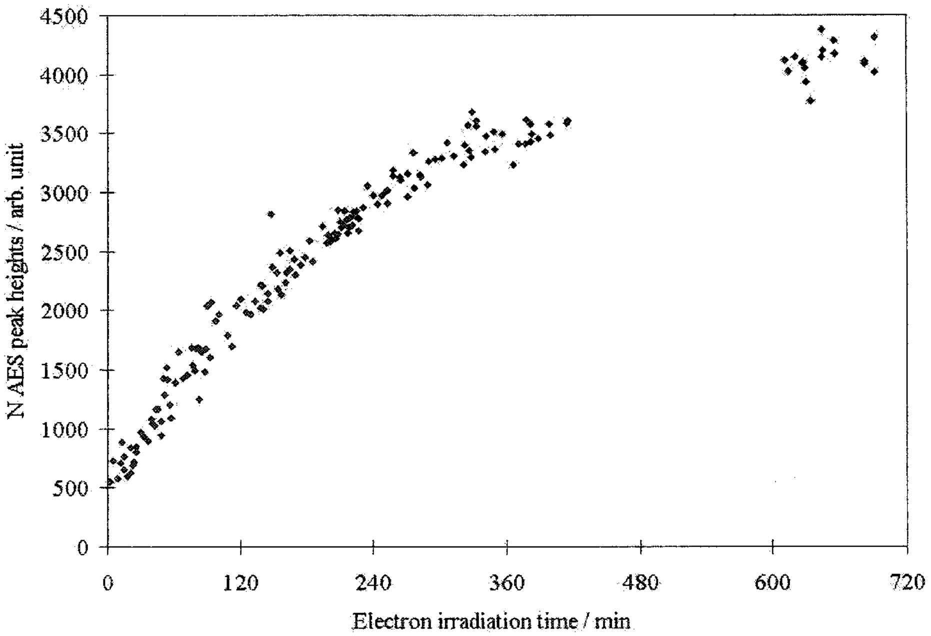

Figure 5-2(h) P(NH_3) = 1.7×10^{-9} torr.

Pressure / torr	GS ads NH_3 coverage / arb. units	Saturation NH_3 coverage / arb. units	Initial adsorption rate / arb. units per min.
1.0×10^{-7}	1220 ± 110	3640 ± 80	223 ± 27
7.5×10^{-8}	1060 ± 80	3680 ± 75	198 ± 17
5.0×10^{-8}	1200 ± 100	3580 ± 70	205 ± 22
3.5×10^{-8}	1100 ± 130	3600 ± 90	191 ± 14
2.0×10^{-8}	1090 ± 80	3830 ± 100	165 ± 10
1.0×10^{-8}	1150 ± 100	3920 ± 80	65 ± 5
5.0×10^{-9}	1020 ± 60	3800 ± 90	31 ± 3

Table 5-1 The values of ground state adsorbed (GS ads) NH_3 coverage, stimulated adsorption saturation NH_3 coverage, and initial rate of stimulated NH_3 adsorption in the W(100) adsorption experiments, at room temperature.

Pressure / torr	GS ads NH_3 coverage / arb. units	Saturation NH_3 coverage / arb. units	Initial adsorption rate / arb. units per min.
5.0×10^{-7}	1120 ± 40	3660 ± 90	36.9 ± 1.1
3.0×10^{-7}	1120 ± 35	—	37.5 ± 1.2
1.0×10^{-7}	1020 ± 50	—	38.6 ± 1.5
7.0×10^{-8}	500 ± 40	3825 ± 110	44.1 ± 1.4
3.0×10^{-8}	1000 ± 60	3975 ± 130	31.8 ± 1.4
1.5×10^{-8}	1030 ± 35	3880 ± 145	28.4 ± 0.8
5.0×10^{-9}	645 ± 40	—	23.1 ± 1.0
1.7×10^{-9}	715 ± 35	—	9.8 ± 0.2

Table 5-2 The values of GS ads NH_3 coverage, stimulated adsorption saturation NH_3 coverage, and initial rate of stimulated NH_3 adsorption in the W(110) adsorption experiments, at room temperature.

Figure 5-3 shows how the initial electron stimulated adsorption rate for W(100) increases with the gas pressure in the low ammonia pressure region (up to $\sim 3\times10^{-8}$ torr). The relationship was broken at high ammonia pressure region (3×10^{-8} - 1×10^{-7} torr) when the rate stopped increasing with the ammonia pressure. The reaction order with respect to ammonia pressure at low pressure was found to be 1.1 ± 0.3. This determination relied only on three data points (5.0×10^{-9}, 1.0×10^{-8} and 2.0×10^{-8} torr) and should be treated with

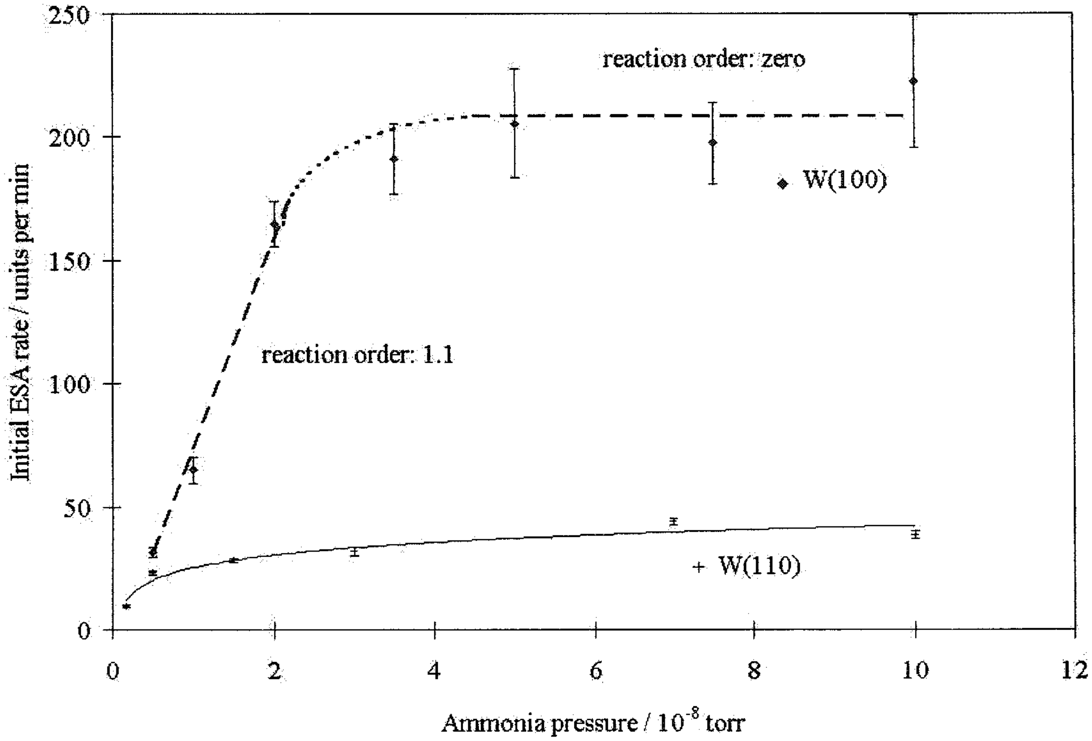

Figure 5-3 Relationship between the initial rate of stimulated NH_3 adsorption on W(100) and the ammonia pressures. The two linear trend lines give the reaction orders. Data on W(110) of the same range of pressure, at the bottom of the graph, are included for comparison. Its full data set is shown on figure 5-4.

care, but is consistent with a direct relationship between the stimulated adsorption rate and the ammonia pressure.

The maximum rate of electron stimulated adsorption of ammonia measured in the high-pressure range ($3.5\times10^{-8} - 1.0\times10^{-7}$ torr) was equivalent to ~ 9×10^{11} atoms cm^{-2} s^{-1} at the given experimental conditions (normal incidence electron beam of 2 keV energy and 25 μA current, crystal at room temperature). The value was calibrated with a reference standard of a full monolayer of nitrogen atoms (10^{15} atoms cm^{-2}) corresponding to 3720 units of nitrogen AES signal.

As a result of the low ESA rate on W(110), more data of nitrogen AES signal could be collected during the initial stage of the adsorption experiments. Smaller uncertainties were thus acquired upon least squares data fitting.

The data from the W(110) stimulated adsorption experiments showed the initial adsorption rate increased with the ammonia pressure up to about 1×10^{-7} torr (figure 5-4).

There is no accurate linear proportionality between the initial rate and the gas pressure as seen in the W(100) experiments. The reaction order with respect to the gas pressure was progressively decreasing and became zero at ~ 10^{-7} torr.

Referring to figure 5-3 the ESA rate on W(110) was much slower than that on W (100) for comparable gas pressure. In fact, the maximum ESA rate on W(110) was only about 20% of that on W(100) under similar experimental conditions.

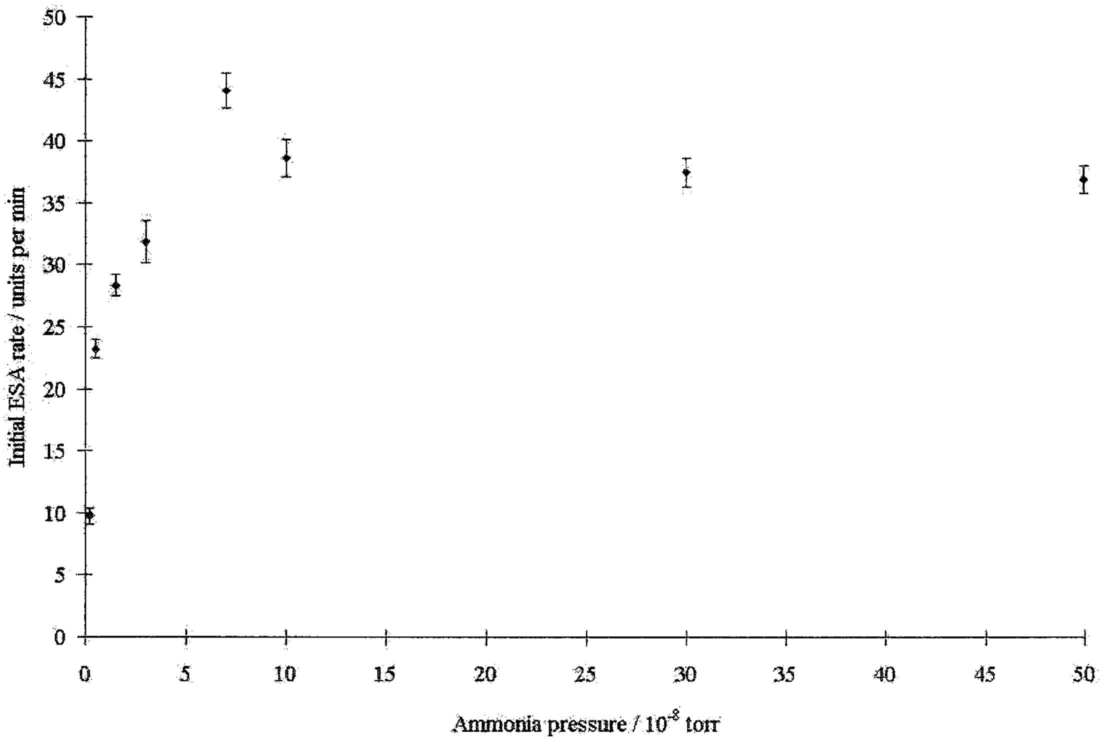

Figure 5-4 Relationship between the initial rate of stimulated NH_3 adsorption on W(110) and the ammonia pressures.

5.4 DISCUSSION

5.4.1 Initial electron stimulated adsorption rate

The numerous examples in figures 5-1 and 5-2 have all demonstrated the initial rate of the nitrogen AES signal increase was constant and coverage-independent up to about 70 % of the saturation level. The observation is consistent and reproducible.

The rarity of a coverage-independence in the adsorption rate was discussed in chapter four. Generally the adsorption rate decreases as the surface becomes more occupied with the adsorbates. The surface concentration of vacant sites, where adsorption occurs, determines the adsorption rate. As the adsorption continues, these vacant sites become occupied with the adsorbates and are not available for further adsorption. Adsorption rates therefore commonly decrease in a $(1-\theta)$ or $(1-\theta)^2$ fashion, θ being the fractional coverage of the adsorbates. Non-dissociative adsorption takes up one surface site for adsorption of each molecule from the gas phase and thus its adsorption rate decreases in a $(1-\theta)$ fashion. Dissociative adsorption which takes up two surface sites for one molecule (*i.e.*, $A_2 + 2^* \rightarrow 2\underset{*}{A}$) has an adsorption rate which correspondingly follows a $(1-\theta)^2$ relationship.

The coverage independence of the stimulated adsorption rate demands that the rate not be affected by occupation of surface sites. Specifically it requires that the surface sites where electron stimulation happens do not become permanently occupied with adsorbates after the stimulated adsorption. By this argument an adsorption mechanism relying on two different kinds of surface sites can be proposed.

5.4.2 ESA active site – chemisorption site model

In this adsorption mechanism there are two kinds of surface sites, the ESA active sites and the chemisorption sites. The ESA active sites are where the electron stimulated dissociation of ammonia molecules takes place. The chemisorption sites are where the dissociated products chemisorb on the crystal surface. After ammonia molecules are dissociated on the activation sites, they rapidly diffuse away from the ESA active sites. This surface diffusion process regenerates a vacant ESA active site and is the key to keep the overall stimulated adsorption rate constant and independent of the adsorbate coverage. The diffused adsorbates are finally chemisorbed onto the chemisorption sites.

Before the beginning of electron irradiation, the W(100) crystal surface had already adsorbed up to a half monolayer of ammonia via ground state adsorption. The electron stimulated adsorption in our discussion therefore began from this ammonia half-covered surface. It is not anticipated that further gas phase ammonia molecules could reside on this crystal surface for an extended period. There is no report of molecular ammonia adsorption on tungsten at room temperature. On the ESA active sites ($*_{act}$) a reversible adsorption of ammonia leads to an equilibrium:

$$NH_3(g) + *_{act} \rightleftharpoons NH_3{-}*_{act} \qquad \ldots (5\text{-}3)$$

where $NH_3{-}*_{act}$ denotes an ammonia molecule reversibly bound to an ESA active site. The ammonia molecules, when stimulated by electron irradiation, dissociate.

$$NH_3{-}*_{act} \xrightarrow{e} NH_2{-}*_{act} + H \qquad \ldots (5\text{-}4)$$

where $NH_2{-}*_{act}$ denotes the NH_2 fragment left on the ESA active site. The hydrogen atom is ejected. Since hydrogen atoms do not compete with nitrogen atoms for adsorption sites on tungsten surfaces, the whereabouts of these hydrogen atoms are not investigated.

The electron stimulated dissociation is followed by the surface diffusion of NH_2 away from the ESA active site to a chemisorption site, $*_{ad}$.

$$NH_2{-}*_{act} + *_{ad} \longrightarrow NH_2{-}*_{ad} + *_{act} \qquad \ldots (5\text{-}5)$$

Through the surface diffusion, the ESA active site is made vacant again. The reactions in equations 5-3 to 5-5 can then be repeated and the stimulated adsorption rate is left unchanged with the increasing adsorbate coverage.

For simplicity, in the following discussion $NH_3{-}*_{act}$ will be referred as NH_3(act).

In this proposed mechanism, it is assumed that no significant stimulated adsorption happens on the chemisorption sites. If these chemisorption sites can also participate in the electron stimulated dissociation process, the overall adsorption rate must become coverage-dependent. As the stimulated adsorption continues, the surface concentration of vacant chemisorption sites must decrease and the adsorption rate will decrease correspondingly.

5.4.3 Zero order behaviour

The reaction orders with respect to ammonia pressure decrease to zero in the stimulated adsorption experiments on W(100) at $\sim 3\times10^{-8}$ torr and W(110) at $\sim 8\times10^{-8}$ torr, figures 5-3 and 5-4 respectively.

As the ammonia pressure increases from a low value, the concentration of the NH_3(act) increases (equation 5-3) and so does the ESA rate (equation 5-4, as seen in the low pressure range in figures 5-3 and 5-4). When the ammonia pressure is increased to the specified values on each crystal surface, the ESA active sites in equation 5-3 become saturated. There are no more ESA active sites available to accommodate an increased number of ammonia molecules when the gas pressure is further increased. [NH_3(act)] reaches its maximum value. Therefore, at the high-pressure range in figures 5-3 and 5-4, the ESA rate becomes insensitive to the ammonia pressure and results in the observed zero order behaviour.

Similar change to zero reaction order at high gas pressure was reported in the studies of electron stimulated nitridation of NH_3/Si(100) [Tarasova *et al.* 1994]. No explanation was given, however.

5.4.4 Concentration of the ESA active sites and the chemisorption sites

The stimulated adsorption rate in this mechanism is limited by the surface concentration of available ESA active sites which will be constant so long as the diffusion rate of the dissociated products away from the sites is fast. In this way we can understand the constant initial adsorption rate. The adsorption rate will decrease when the surface is significantly occupied to an extent that the diffusion of NH_2 across the surface becomes slow relative to the stimulated adsorption rate.

The present AES results do not allow the determination of the specific atomic positions of the ESA active sites and chemisorption sites. The few LEED results attempted during the electron stimulated adsorption process show only the substrate (1×1) pattern. The LEED frames were diffuse, presumably the result of a lack of long-range order in the presence of 10^{-7} torr ammonia pressure.

The surface concentrations of the ESA active sites and chemisorption sites are yet to be determined. It is believed electron stimulation increases the ammonia coverage from a half monolayer to a full monolayer. This suggests that the surface concentration of the chemisorption sites can be half the atomic density of the crystal surface.

Occupation of ESA active sites by ammonia to any appreciable extent should have effectively increased the ground state adsorption. The adsorption is going to increase with the gas pressure. Since the ground state adsorption coverage shows no detectable increase with pressure, the concentration of such sites must be very small. Given the sensitivity of AES is approximately 1% of a monolayer of adsorbate, the maximum surface concentration of ammonia in the ESA active sites must be less than 1% ML, or 10^{13} cm^{-2} on the tungsten crystal surfaces [Briggs and Seah 1983, Woodruff and Delchar 1994].

The identity of the ESA active sites with such low concentration on a single crystal surface is not obvious. Assuming there has been no reconstruction of the surface structure, the ESA active sites may be special sites created within the adsorbed layer. However, if the ESA active sites are continuously created upon adlayer reconstruction, this will lead to an adsorbate coverage dependence of the ESA rate. This is in contrast to the idea developed from the proposed model that the concentration of ESA active sites remains constant regardless of the change in the surface coverage of adsorbates.

5.4.5 Ammonia coverage by ground state adsorption

Ground state adsorption in the increasing ammonia pressure environment was represented by the back-extrapolated *y*-intercepts in the nitrogen AES signal evolution graphs. In the series of stimulated adsorption experiments, the ammonia pressure (10^{-9} - 10^{-7} torr) was not shown to affect the ground state ammonia uptake. The nitrogen AES signals were in the range of 1000-1200 arbitrary units in the stimulated adsorption experiments on W(100), table 5-1. There was a wider range of 500-1100 arbitrary units on W(110), table 5-2, but there was no pattern of monotonic change.

This ground state ammonia coverage is a measure of the ammonia adsorbed during the few minutes when ammonia was filling into the vacuum chamber. The ammonia pressure was increasing from practically zero to the experimental value during this time. If the pressure-independence is interpreted as the crystal surface being saturated with ammonia by ground state adsorption, the Auger signals of ~1200 units (on W(100)) are low compared to the saturated ground state ammonia coverage (~1680 units) reported in chapter three. The disagreement is also observed in the W(110) data (~1000 units compared to ~1290 units).

The ground state ammonia adsorption experiments in chapter three were performed with a dynamically regulated gas flow impacting directly on the crystal surface. Substituting the values of the gas flow in the equation of collision frequency at a surface (equation 5-1, with the ideal gas law assumption), the equivalent ammonia pressures in the ground state adsorption experiments were between 4×10^{-7} and 1×10^{-5} torr.

It is therefore understandable the ammonia uptake by ground state adsorption before electron irradiation was possibly not up to the saturation level. The adsorption time was shorter, and the ammonia pressure was generally lower.

The apparent pressure-independence of the ground state ammonia coverage in the stimulated adsorption experiments has yet to be fully understood.

5.4.6 Saturation coverage by stimulated adsorption

The saturated ammonia coverage resulting from electron stimulated adsorption was shown to be unaffected by the ammonia pressure in these experiments, as would be expected. The final nitrogen AES signals were of similar sizes (~ 3800 arb. units) on both orientations. This meant that the surface concentrations of nitrogen were similar on the two surfaces for saturated adsorption. At room temperature diffusion of adsorbates toward the bulk of the tungsten sample was negligible. The nitrogen adsorbates were kept on the topmost layers on both (100) and (110) surfaces. Phase transitions of these adsorbed nitrogen atoms from overlayer to underlayer were reported to happen only at temperature higher than ~620 K [Chen 1996].

Unlike the initial ground state ammonia coverage, this saturated coverage should only be limited by the available adsorption sites on the sample surface, and hence not affected by the ammonia pressure. It simply took a longer time to reach this saturation level in the lower pressure adsorption experiments (2.5 hours at 5×10^{-9} torr over 25 minutes at 1×10^{-7} torr). The similar nitrogen AES signals measured on both crystal surfaces suggested this saturation coverage was not affected by the difference in the geometric factors on the two orientations of the tungsten substrate.

5.5 CONCLUSION

In this chapter the effects of the ammonia pressure on the electron stimulated ammonia adsorption on both W(100) and W(110) have been presented. The extrapolated values for ground state adsorption were not affected by ammonia pressure. The saturated ammonia uptake by electron stimulated adsorption was also unaffected by the ammonia pressure.

A consistent observation of linear nitrogen AES signal increase with respect to the electron stimulated adsorption time was noted. This pattern of AES signal increase was seen as equivalent to a coverage-independent stimulated ammonia adsorption rate. The independence was seen from 10^{-9} to 10^{-7} torr of ammonia pressure. The unconventional coverage-independence of the adsorption rate was explained with an "ESA active site – chemisorption site" model proposal which incorporated a concept of classifying the surface sites into ESA active sites and chemisorption sites. Ammonia molecules were adsorbed onto the ESA active sites and then were dissociated by electron stimulation. The adsorbates quickly relocated to a different chemisorption site via rapid surface diffusion. This regenerated the ESA active site for further stimulated ammonia dissociation. By not permanently occupying the ESA active sites, the stimulated adsorption rate became independent of the adsorbate coverage. The overall stimulated adsorption rate was only limited by the rate of surface diffusion of the dissociated adsorbates from the ESA active sites to the chemisorption sites. This seemed to occur when the adsorbate coverage increases past 70% of final saturation values.

The stimulated ammonia adsorption on W(100) at room temperature was found to have a reaction order of 1.1 ± 0.3, with respect to the ammonia pressure, at low pressures. At ammonia pressure higher than $\sim 3\times10^{-8}$ torr, the reaction order became zero. The zero order behaviour was also observed in stimulated adsorption experiments on W(110) with pressure higher than 8×10^{-8} torr. The zero order behaviour can be explained by a complete occupation of ESA active sites by ammonia at or above the specified gas pressure. In fact, the surface concentration of the ESA active sites was deduced to be smaller than 1% ML (see section 5.4.3).

Discussions about the roles of ammonia and ESA active sites, and the change of reaction order are continued in the next two chapters, which describe the effects of the crystal temperature and the electron beam current density on the stimulated adsorption rates.

CHAPTER SIX

CRYSTAL TEMPERATURE EFFECTS ON THE KINETICS OF THE STIMULATED AMMONIA ADSORPTION

6.1 INTRODUCTION

Generally reaction rates are dependent on temperature. The temperature effects on heterogeneous reactions involving gas molecules can be more subtle. In addition to altering the rate constant of a surface reaction, a change in temperature may also affect the concentration of the reactants on a sample surface.

The electron stimulated ammonia adsorption process is not a simple reaction. The rate-limiting step of the complex reaction scheme is thought to be the electron stimulated dissociation of an ammonia molecule in an ESA active sites into a strongly adsorbed NH_2,

$$NH_3(act) \xrightarrow{e} NH_2(ad) + H \qquad \ldots (6\text{-}1).$$

The concentration of the ammonia will be determined by an equilibrium with vacant surface sites and ammonia gas.

$$NH_3(g) + * \rightleftharpoons NH_3(act) \qquad \ldots (6\text{-}2).$$

If the electron stimulated dissociation is the slow, rate-determining step, saturation of the ESA active sites with ammonia can lead to the zero order pressure dependence discussed earlier. The equilibrium constant is expected to be temperature-dependent, given the exothermic nature of the adsorption process. An elevated sample temperature should shift the equilibrium toward the reactants, *i.e.*, the gas phase, and therefore lower the surface concentration of the ammonia molecules in the ESA active sites.

Grosman and Löffler [1983] measured the rates of ammonia decomposition, *without* electron stimulation, on polycrystalline tungsten wires between 900 and 2200 K. They claimed their data fit accurately to a Langmuir-Hinshelwood rate expression,

$$R = k_0 KP / (1+KP) \qquad \ldots (6\text{-}3),$$

where the reaction rate constant,

$$k_0 = A_0 \exp (-E_0 / RT) \qquad \ldots (6\text{-}4),$$

and the adsorption constant for ammonia,

$$K = A_K \exp (-E_K / RT) \qquad \ldots (6\text{-}5),$$

where E_0 and E_K are the activation energy for reaction and the heat of adsorption of ammonia, respectively. Their interpretation put the values of E_0 and E_K equal to each other. This value of E_K is important to us because it equalled to the desorption energy of ammonia from the sample surface. Their determined E_K value fell in the range of 38.0 - 44.4 kcal mole^{-1}, which was in good agreement with other published results [McAllister and Hansen 1973, Dawson 1974].

Alnot *et al.* [1989] showed that the ammonia decomposition on W(100) was strongly dependent on the surface temperature. They showed that the surface nitrogen coverage decreased with increasing crystal temperature. At 500 K, even after 20 minutes of adsorption with a gas flux of ~10^{12} molecules cm^{-2} s^{-1} the saturation coverage was not reached. The adsorption of ammonia was said to be the rate-limiting step, at this high surface temperature.

These earlier results pertain only to ground state ammonia adsorption on tungsten. There has been no previous investigation into the temperature dependence of ESA.

The rate-limiting step of the electron stimulated ammonia adsorption, the stimulated N–H bond dissociation, is not a thermally activated process. In principle the rate of this reaction step is not affected by temperature. The surface concentration of ammonia, however, depends on the temperature and hence the overall electron stimulated adsorption rate is still a function of the crystal temperature.

In order to study the temperature effects on the kinetics of the electron stimulated ammonia adsorption on tungsten single crystal surfaces, many adsorption experiments were performed at different crystal temperature. The thermocouples spot-welded on the crystals and a high precision millivoltmeter allow an accurate control of crystal temperature (± 3 K). The ammonia gas admitted into the vacuum chamber from the precision leak valve of the stainless steel gas handling line is at room temperature. It is therefore assumed that the ammonia gas inside the vacuum chamber, before it collides with the hot crystal surfaces, is also at room temperature.

6.2 EXPERIMENTAL PROCEDURES

Electron stimulated ammonia adsorption experiments on W(100) and W(110) were conducted at varying crystal temperatures from room temperature (300 K) to 470 K.

6.2.1 Experiments at 465 K and different ammonia pressure

In order to obtain a better understanding of the ESA active sites and the ammonia adsorbates introduced in chapter five, electron stimulated ammonia adsorption experiments on W(100) were performed at a higher temperature (T = 465 K, $P(NH_3) = 8.8\times10^{-8} - 1\times10^{-6}$ torr) to complement the experimental results in the previous chapter (T = 320 K, $P(NH_3) = 5\times10^{-9} - 1\times10^{-7}$ torr).

The adsorption experiments began with a clean tungsten crystal sample facing the electron gun and the retarding field energy analyzer. The shutter in front of the whole electron optics assembly was closed to block any premature electron irradiation of the sample surface. The electron gun was switched on to the standard operating condition, yielding a beam current of 25.0 μA. The filament behind the sample was switched on to heat the sample by radiation. The accelerating voltage was not applied because: *(i)* the crystal temperatures necessary for the experiment was low and achievable by radiation heating alone; and *(ii)* the applied potential difference tended to affect the AES data acquisition. The peak shapes of the spectra became distorted for reasons which are not fully understood. The crystal temperature was continuously monitored with the spot-welded thermocouples. The voltage across the heater filament was continuously adjusted to regulate the crystal temperature to 465 ± 3 K.

Once the crystal temperature was kept constant at 465 K, the sample was exposed to pure ammonia by back-filling the vacuum chamber through the precision leak valve connected to the gas handling system. The ammonia pressure inside the chamber was continuously measured by QMS. The gas composition was checked by QMS as well to guard against contamination such as from oxygen and water vapour. Once the ammonia pressure approached the experimental pressure, the leak valve of the gas handling system was closed to reduce the ammonia admission and stabilize the ammonia pressure inside the vacuum chamber dynamically.

Electron irradiation on the sample surface began when the shutter was opened, and a timer started simultaneously to measure the electron exposure time. The surface composition, particularly the nitrogen coverage, was continuously monitored by AES. The acquired nitrogen and tungsten AES signals were plotted against the electron irradiation time. At times the AES energy window was increased in order to check the carbon and oxygen contamination levels on the surface.

Because of a slow stimulated adsorption rate, the adsorption experiments were not carried out to saturation. The experiments were stopped after sufficient nitrogen AES data had been collected to determine the initial rate of stimulated adsorption. At the end of the adsorption experiments, the heater was switched off, the crystal sample was turned away from the electron beam, and the leak valve for ammonia admission and the shutter in front of the electron gun were closed.

6.2.2 Experiments at 1×10^{-7} torr and different crystal temperature

After the completion of the stimulated adsorption experiments at 320 and 465 K, adsorption experiments at six other crystal temperatures within the range were carried out in 1×10^{-7} torr of ammonia. The kinetic data acquired in these experiments bridged the gap between the data of the experiments performed over a range of ammonia pressures at the two ends of the temperature range. Electron stimulated adsorption experiments at crystal temperatures of 460 K and below had a reasonable adsorption rate. Saturated adsorption could be achieved in a reasonable period.

Stimulated adsorption experiments on W(110) at 3×10^{-7} torr ammonia pressure and 300, 365, 410 and 468 K crystal temperatures were performed in a similar manner.

6.3 RESULTS

6.3.1 Experiments at 465 K and different ammonia pressure

Nitrogen AES signal evolution graphs acquired in the stimulated adsorption experiments are shown in figures 6-1 (a)-(g). At relatively high pressure, 3×10^{-7} to 1×10^{-6} torr, figures 6-1 (a)-(d), the shape of the electron stimulated adsorption profile was similar to those observed at room temperature. At lower pressure, a new feature was observed. There was an initial "induction period" during which there was no increase of nitrogen AES signal even with electron stimulation (figures 6-1 (e)-(g)). After a period of zero growth rate, the increase of nitrogen AES signals with electron irradiation time returned to the generally observed behaviour with a relatively constant adsorption rate over the adsorption time (and adsorption coverage). The length of the induction period increased with decreasing ammonia pressure.

Overall the ammonia uptake in the ground state adsorption stage was higher (1300-1650 units) than observed at room temperature adsorption (1000-1200 units). It matched the observation reported in chapter three. The ground state coverage at 465 K did not show any systematic variation with the ammonia pressure.

The data for the initial rates of adsorption as a function of pressure at 465 K are plotted in figure 6-2 (a). For lower gas pressure the rate reported was that following the induction period. The rate of stimulated ammonia adsorption on W(100) at 465 K was found to increase linearly with ammonia pressure. A comparison of the pressure dependence of the ESA rates at 465 and 320 K is shown in figure 6-2 (b).

At 465 K, the adsorption rates were much lower than those at 320 K. The large difference in the adsorption rates was remarkable because the crystal temperature difference was but 150 K. In the 465 K experiments with ammonia pressure lower than 8.8×10^{-8} torr the adsorption rate was simply not measurable. The rate difference was actually understated because the difference of ammonia pressure has not yet been

Figure 6-1 N AES signal evolution graphs for electron stimulated ammonia adsorption on W(100) at 465 K and different gas pressure: (a) 1×10^{-6} torr, (b) 5×10^{-7} torr, (c) 4×10^{-7} torr, (d) 3×10^{-7} torr, (e) 2×10^{-7} torr, (f) 1×10^{-7} torr & (g) 8.8×10^{-8} torr. The electron beam was at normal incidence, of beam energy 2.0 keV and beam current 25.0 μA. The linear N AES signal increases and the induction periods are highlighted.

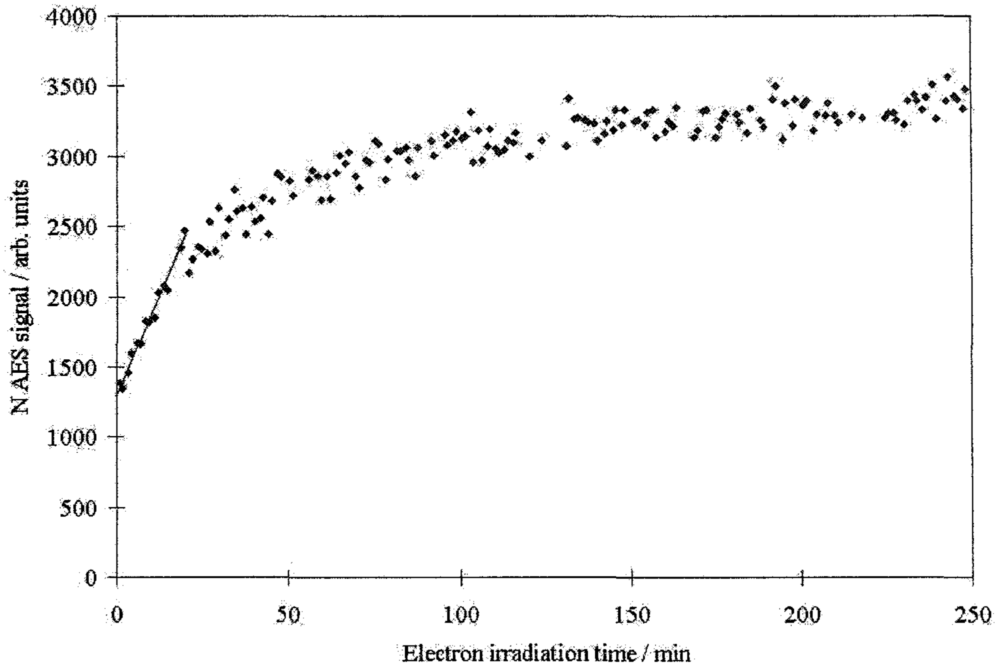

(a) P(NH_3) = 1×10^{-6} torr

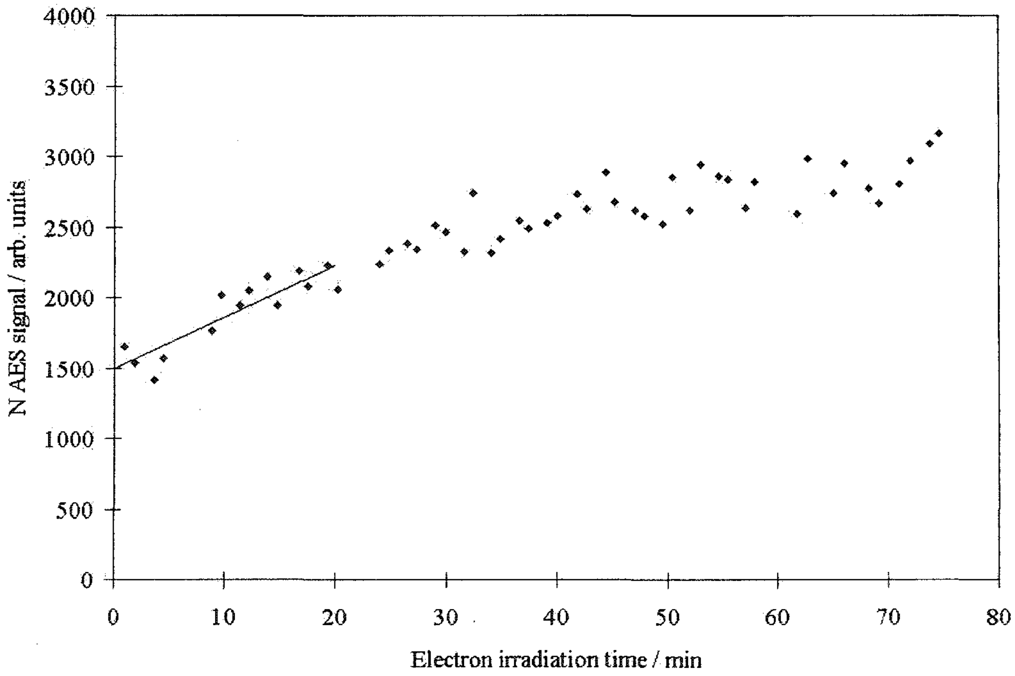

(b) P(NH_3) = 5×10^{-7} torr

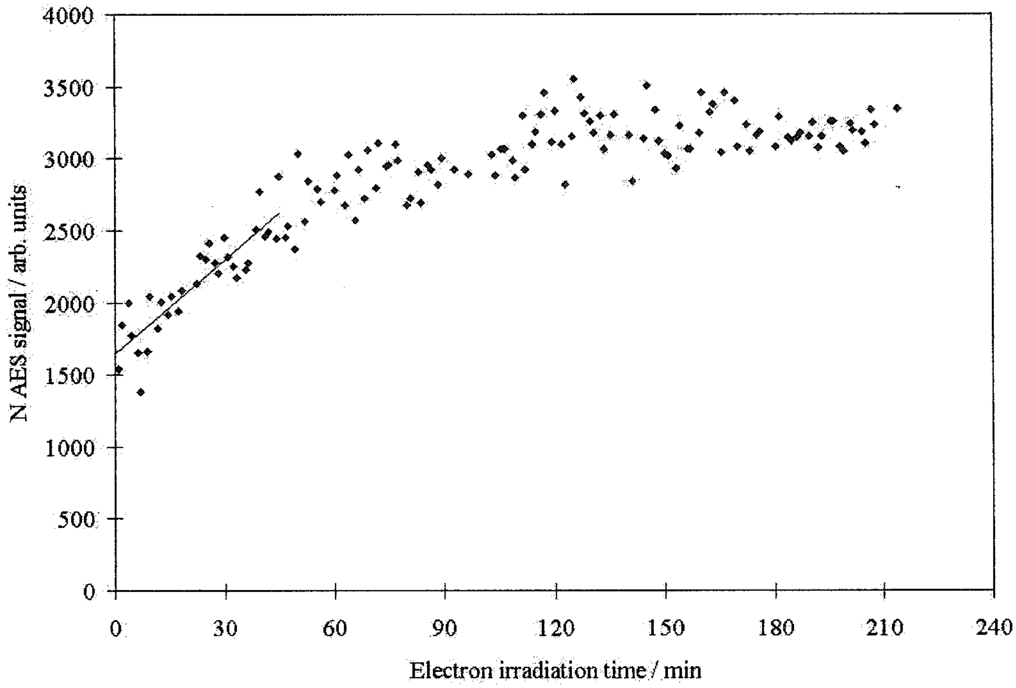

(c) P(NH_3) = 4×10^{-7} torr

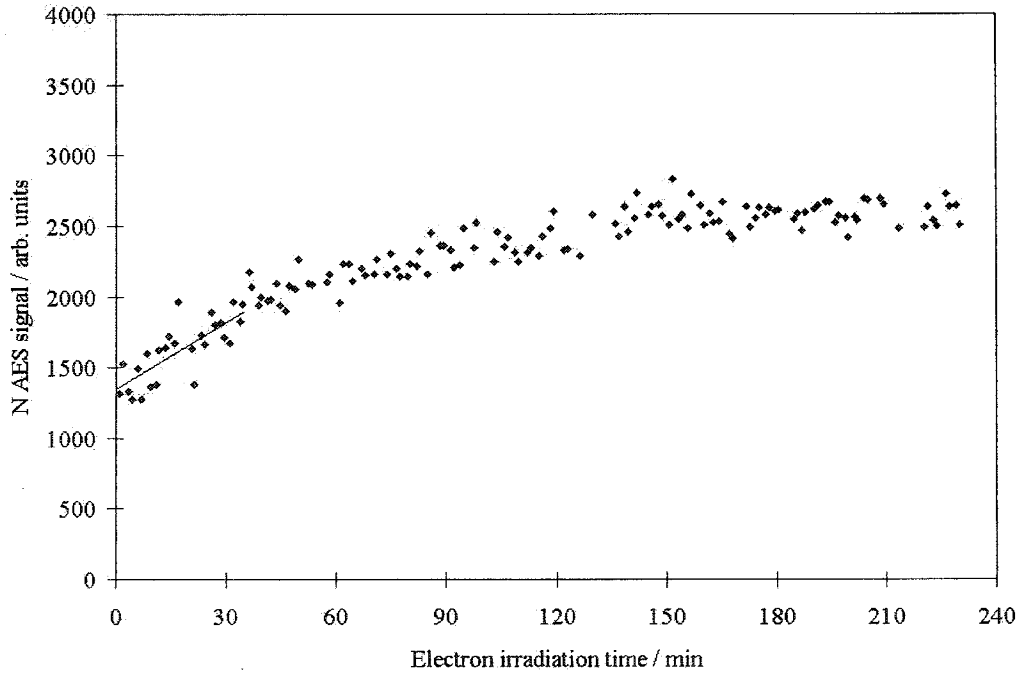

(d) P(NH_3) = 3×10^{-7} torr

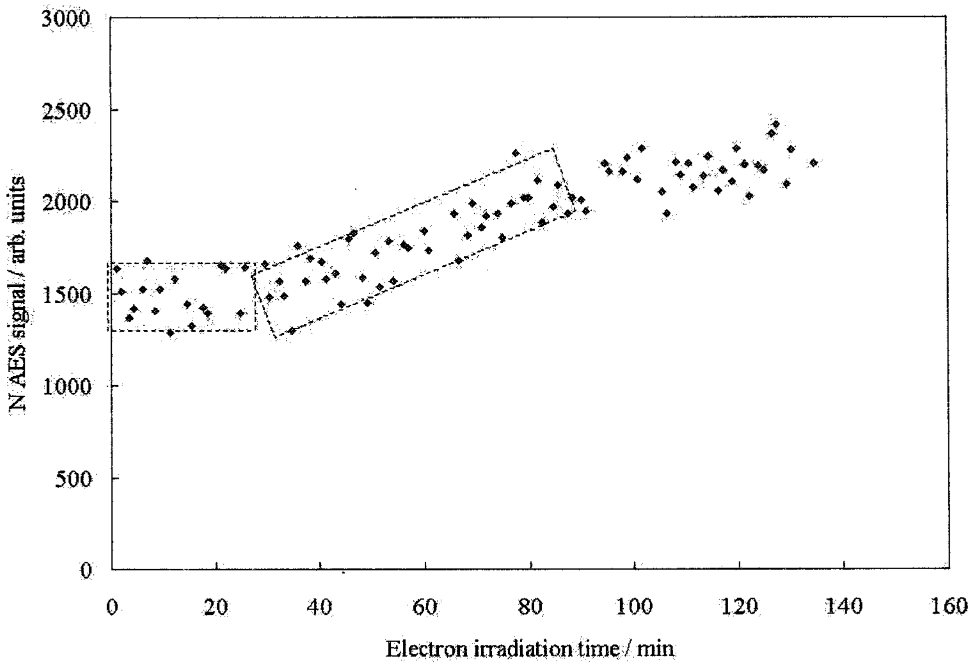

(e) P(NH_3) = 2×10^{-7} torr

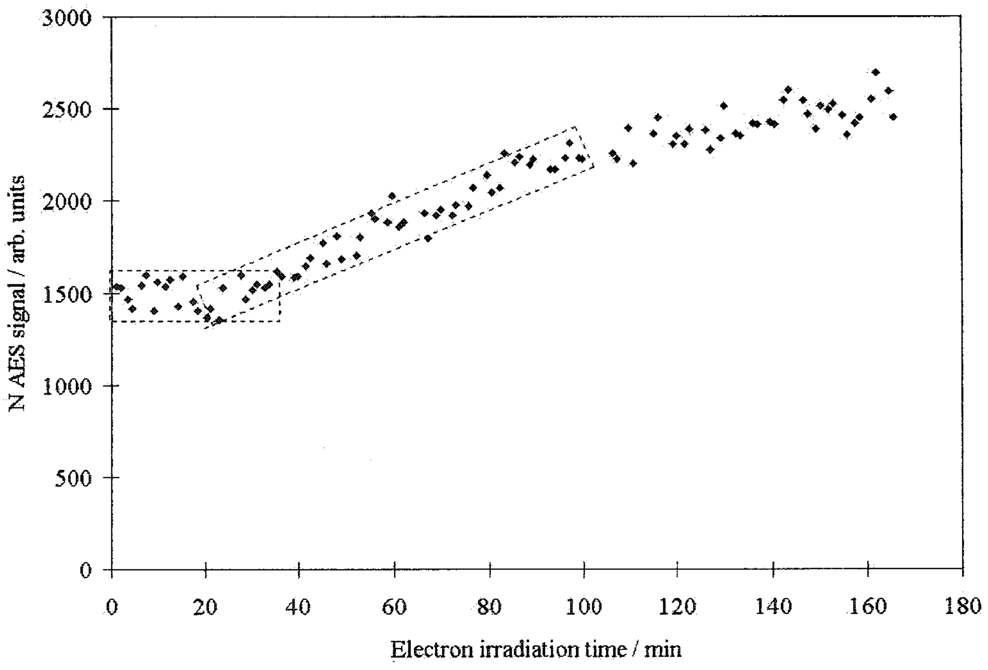

(f) P(NH_3) = 1×10^{-7} torr

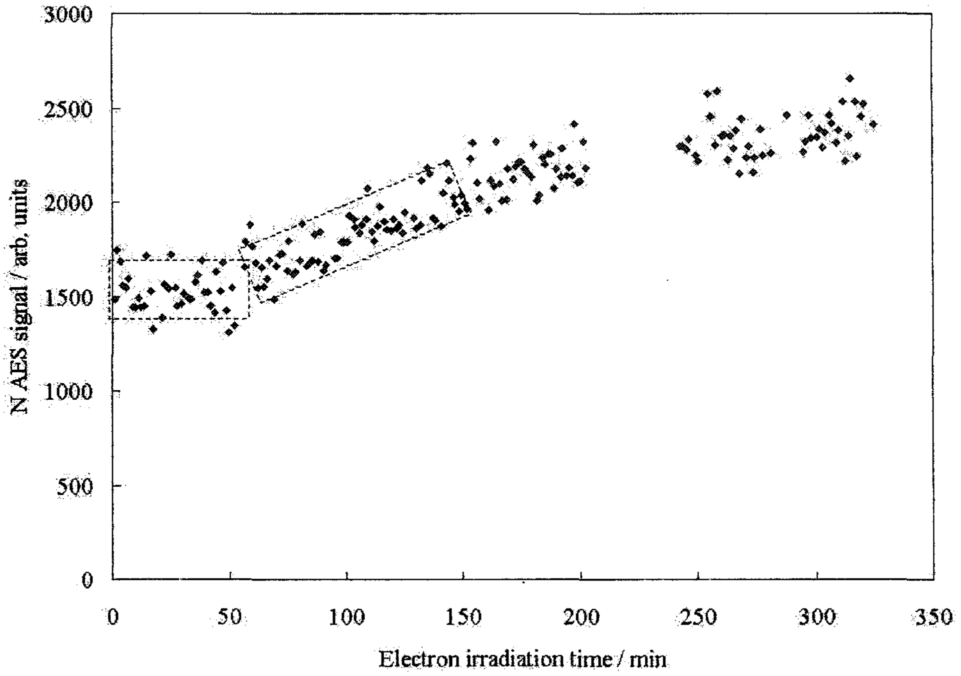

(g) P(NH_3) = 8.8×10^{-8} torr

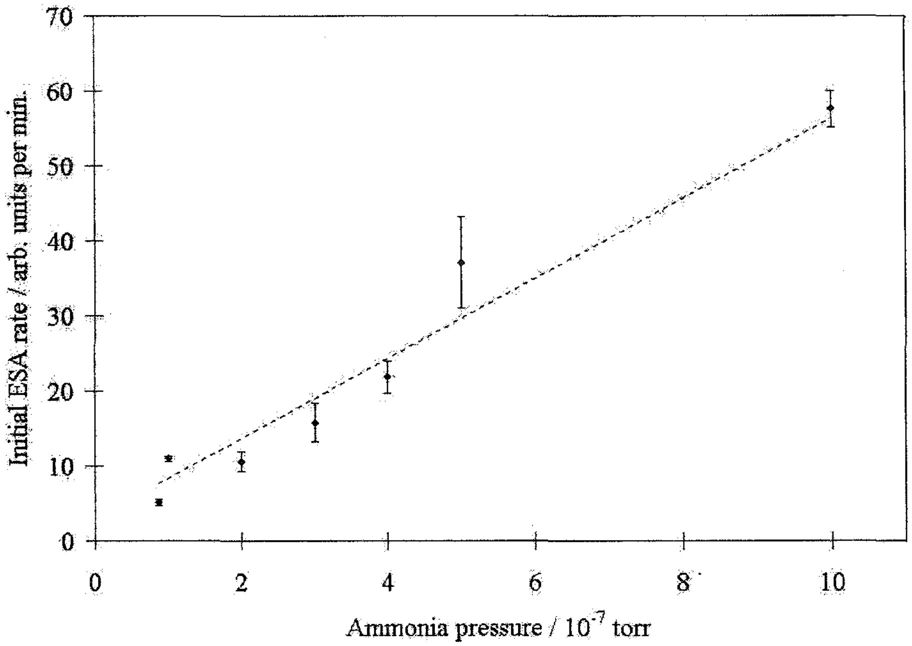

Figure 6-2 (a) The relationship between the initial rates of stimulated NH_3 adsorption on W (100) at 465 K *vs*. the ammonia pressures. A linear trend line was fitted to the data.

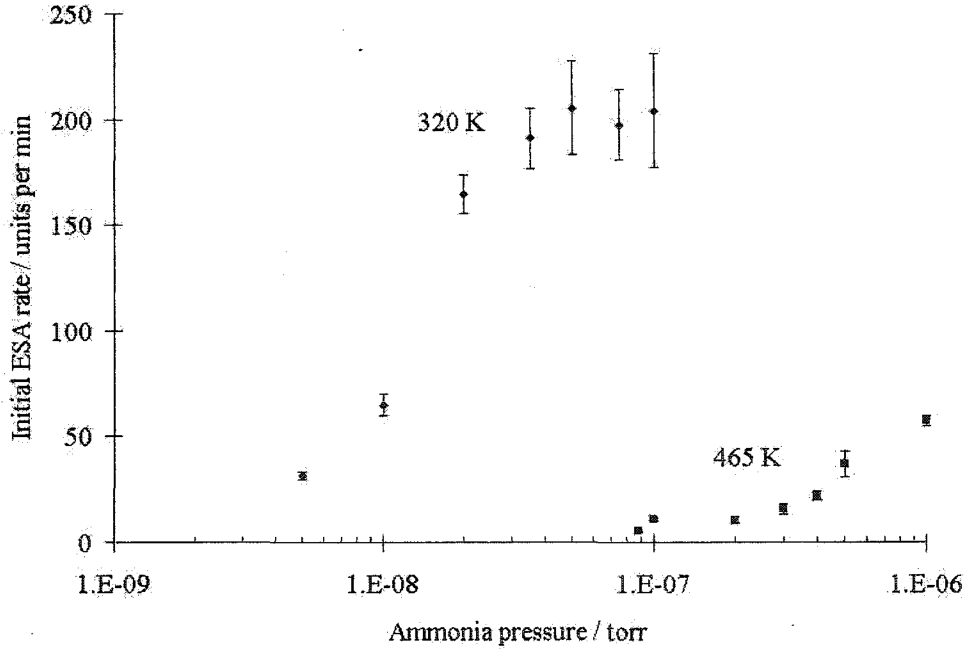

Figure 6-2 (b) The initial rates of stimulated ammonia adsorption on W(100) at 320 and 465 K *vs*. ammonia pressure was plotted together for comparison.

considered. It was established in chapter five that the stimulated adsorption rate increased with the ammonia pressure. Yet the 465 K experiment at 1×10^{-6} torr showed an adsorption rate an order of magnitude smaller than the 320 K experiment at 1×10^{-7} torr, an order of magnitude lower pressure. Given that the adsorption rate on W(100) was an approximately linear function of pressure at both temperatures we estimate a two order of magnitude decrease in adsorption rate at 465 over 320 K. The data collection for the saturation ammonia coverage was incomplete. Other than an adsorption experiment at very high ammonia pressure (1×10^{-6} torr), the stimulated adsorption rates were so slow that after over five hours of stimulated ammonia adsorption at 8.8×10^{-8} torr a saturated ammonia adsorption on the sample surface still was not achieved. The acquired kinetic data from the stimulated adsorption experiments at 465 K are summarized in table 6-1.

At 465 K the adsorption rate continuously increased through 1×10^{-6} torr. This displayed a major contrast with the 320 K experiments, when the adsorption rates reached a maximum value after a certain ammonia pressure was surpassed.

P(NH_3) / torr	GS adsorption NH_3 coverage / arb. units	Induction period / min	Apparent final NH_3 coverage / arb. units	Post-induction ESA rate / units per minute
1×10^{-6}	1290 ± 45	—	3360 ± 95	57.6 ± 2.4
5×10^{-7}	1500 ± 70	—	—	36.5 ± 5.3
4×10^{-7}	1650 ± 60	—	3180 ± 125	21.9 ± 2.1
3×10^{-7}	1350 ± 55	—	—	15.8 ± 2.6
2×10^{-7}	1490 ± 190	20–30	—	9.6 ± 1.3
1×10^{-7}	1500 ± 140	30–40	—	11.0 ± 0.4
8.8×10^{-8}	1540 ± 160	50–60	—	5.2 ± 0.4

Table 6-1 Experimental data for electron stimulated ammonia adsorption on W(100) at 465 K and different ammonia pressures. The normal incidence electron beam is of energy 2.0 keV and current 25.0 μA. Ground state adsorption coverage data for the three lowest ammonia pressures were the nitrogen AES signals of the induction periods preceding the signal increase.

6.3.2 Experiments at 1×10^{-7} torr and different crystal temperature

The nitrogen AES signal evolution at seven different crystal temperatures are shown in figure 6-3 (a)-(g). Once again we observe a coverage-independent adsorption rate over a significant coverage range.

However, the coverage independent rates are temperature dependent and the time required for saturated ammonia adsorption increases with the crystal temperature. The final nitrogen uptake seems to decrease slightly with increasing crystal temperature; the variation was small and not clearly monotonic. The ground state ammonia coverage (the y-intercept values), adsorbed before electron irradiation, did not show monotonic variation with the crystal temperature. The ground state ammonia adsorption coverage, the saturation ammonia coverage and the initial stimulated adsorption rates at various crystal temperatures are given in table 6-2. The relationship between the crystal temperature and the initial adsorption rates on W(100), at 1×10^{-7} torr ammonia pressure are plotted in figure 6-4.

For comparison, the initial rates of stimulated ammonia adsorption on W(110) at 3×10^{-7} torr and different crystal temperature between 300 and 468 K are plotted in figure 6-5. The four data points demonstrate a similar behaviour to that observed for W(100) with a decreasing initial adsorption rate with an increasing crystal temperature.

No induction period was observed in any of the four electron stimulated ammonia adsorption experiments on W(110).

Figure 6-3 N AES signal evolution graphs for electron stimulated ammonia adsorption experiments on W(100) in 1×10^{-7} torr ammonia, and varying crystal temperature: (a) 460 K, (b) 450 K, (c) 440 K, (d) 430 K, (e) 410 K, (f) 380 K, and (g) 320 K. The electron beam was at normal incidence, of beam energy 2.0 keV and beam current 25.0 μA.

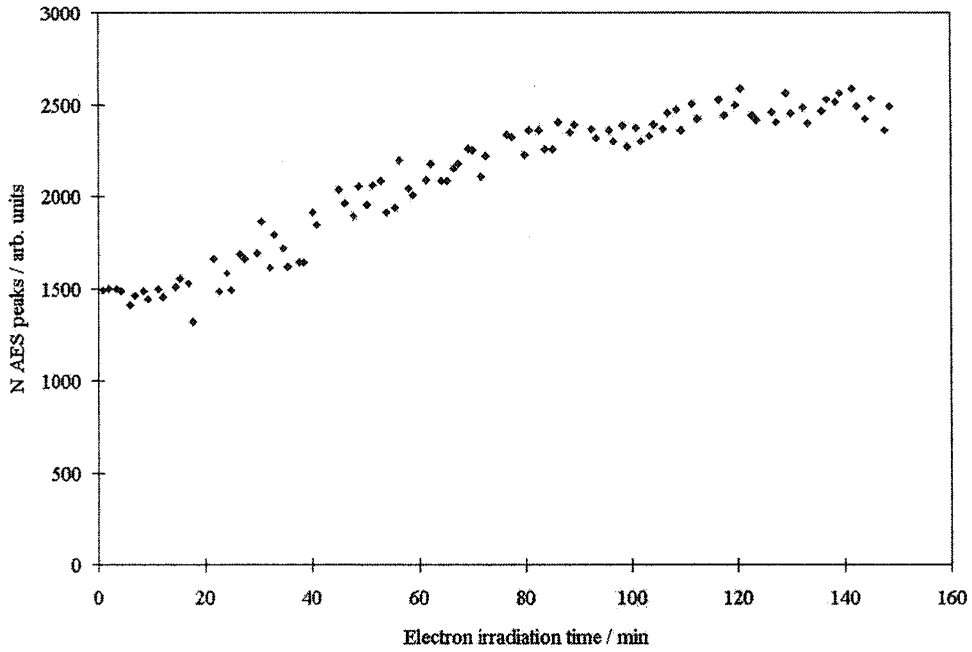

Figure 6-3(a) T = 460 K

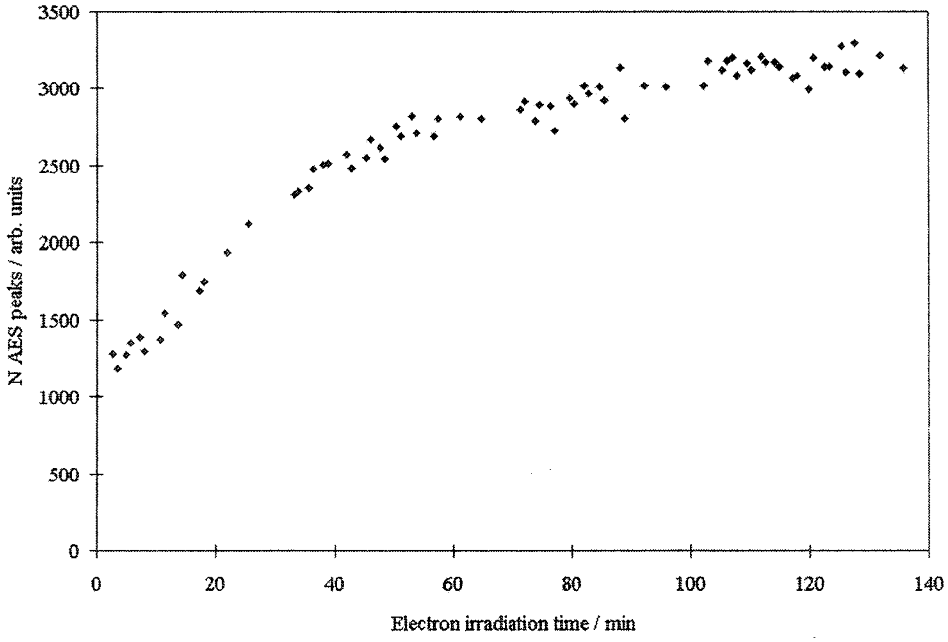

Figure 6-3(b) T = 450 K

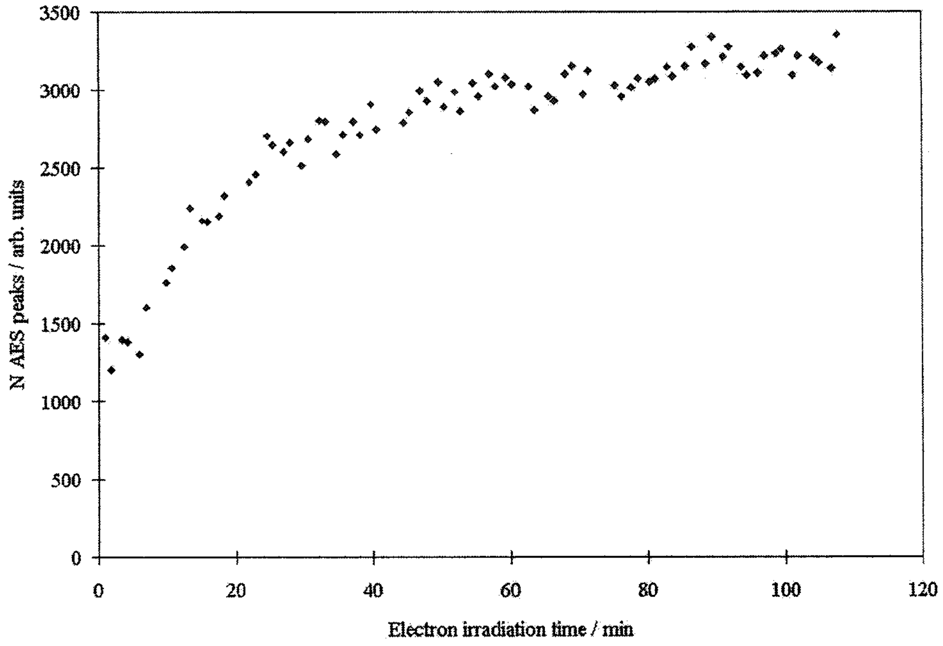

Figure 6-3(c) T = 440 K

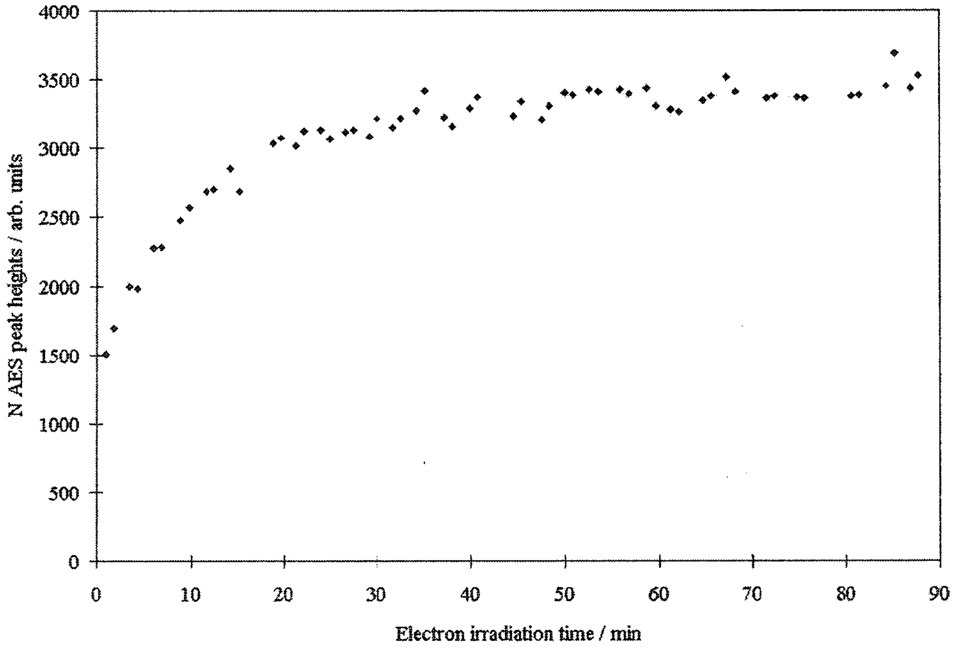

Figure 6-3(d) T = 430 K

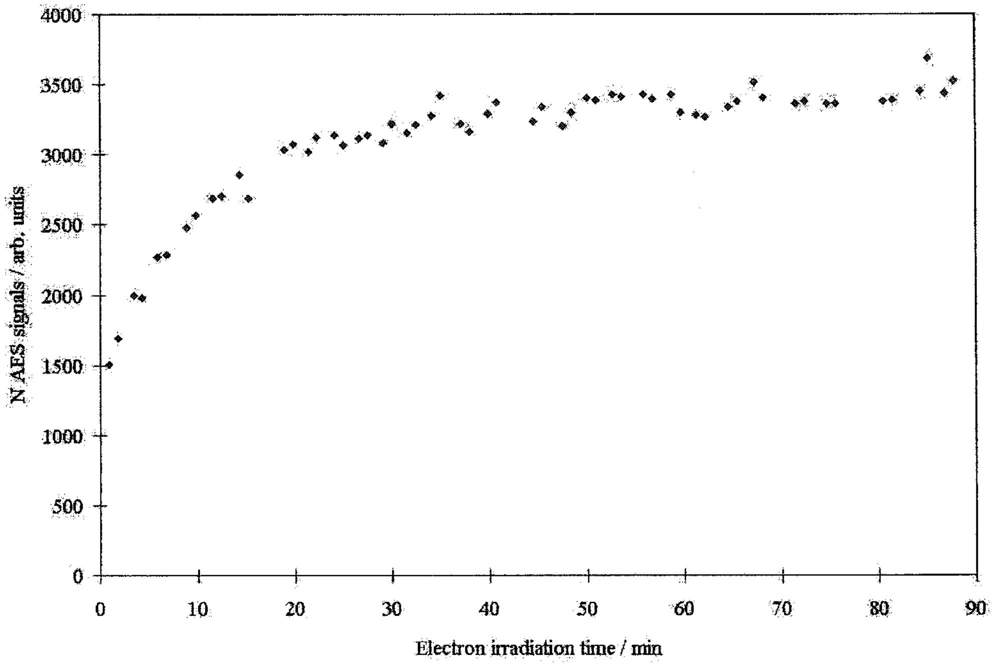

Figure 6-3(e) T = 410 K

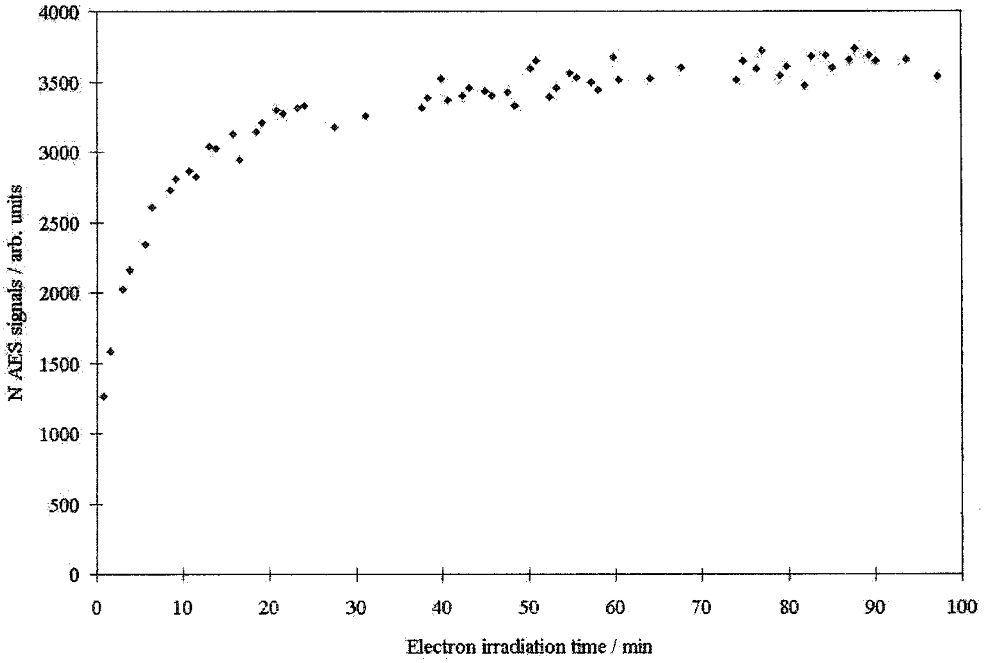

Figure 6-3(f) T = 380 K

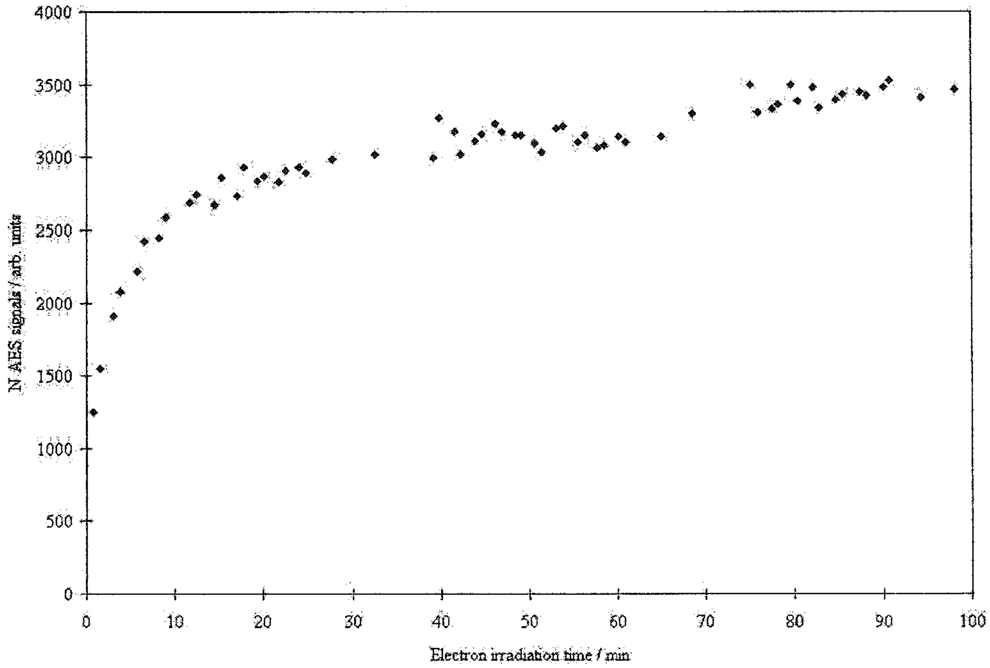

Figure 6-3(g) T = 320 K

Crystal temperature / K	GS ads. NH_3 coverage / arb. units	Apparent final NH_3 coverage / arb. units	Initial ESA rate / Arb. units per minute
465	1500 ± 140	—	11.0 ± 0.4
460	1500 ± 60	2480 ± 125	14.4 ± 1.6
450	1100 ± 30	3050 ± 170	37.0 ± 1.3
440	1150 ± 70	3170 ± 130	67.5 ± 7.2
430	1310 ± 60	3460 ± 85	124 ± 10
410	1480 ± 60	3450 ± 105	119 ± 11
380	1220 ± 60	3510 ± 120	170 ± 20
320	1140 ± 80	3650 ± 130	228 ± 19

Table 6-2 Experimental data for electron stimulated ammonia adsorption on W(100) in 1 $\times 10^{-7}$ torr ammonia and at specified crystal temperature. The normal incidence electron beam is of energy 2.0 keV and current 25.0 μA.

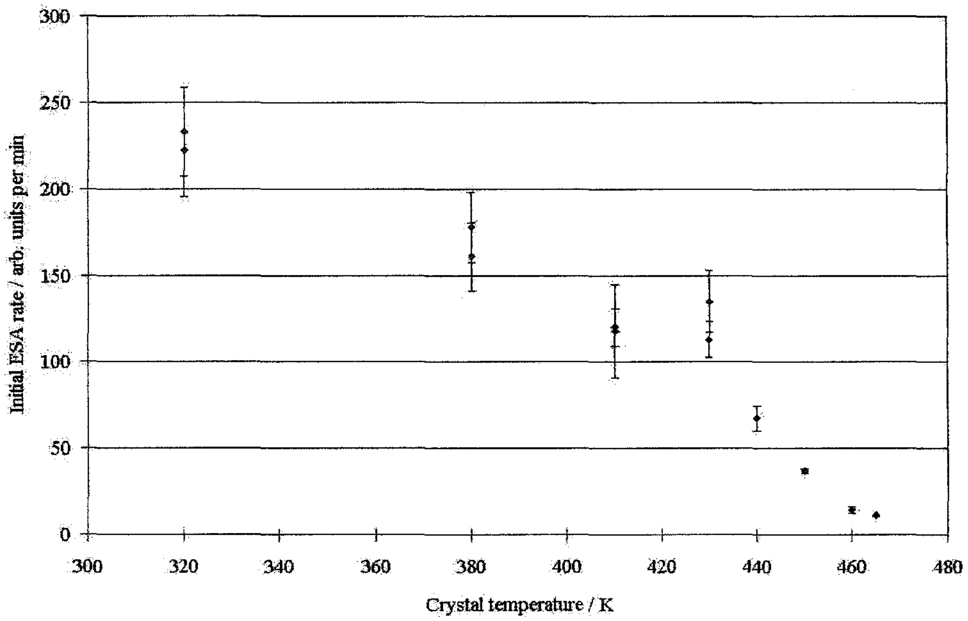

Figure 6-4 The initial rates of stimulated NH_3 adsorption on W(100) at different crystal temperatures. $P(NH_3) = 1\times10^{-7}$ torr.

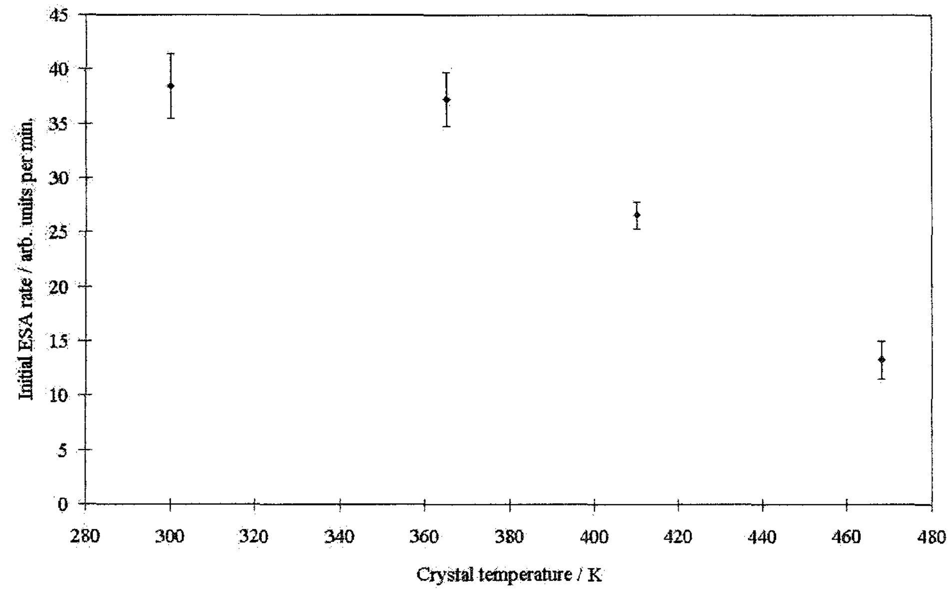

Figure 6-5 The initial rates of stimulated NH_3 adsorption on W(110) at different crystal temperatures. $P(NH_3) = 3\times10^{-7}$ torr.

6.4 DISCUSSION

The electron stimulated ammonia adsorption on W(100) and W(110) are affected by crystal temperature in a similar fashion. The effect of temperature on the ground state ammonia adsorption coverage will first be discussed, followed by an analysis of the temperature effects on the initial adsorption rates. The origin of the induction period will also be discussed. A discussion of the apparent saturation coverages will conclude this section.

6.4.1 Ground state adsorption coverage

The ground state ammonia adsorption is achieved via thermal dissociation of an N–H bond of an ammonia molecule on the tungsten crystal surfaces. Generally bond breaking is facilitated by high temperature, which helps overcome the activation energy involved. On this argument alone the ground state adsorption coverage should increase with the crystal temperature, until every other site is occupied. Ideally this adlayer structure leaves no pair of neighbouring vacant sites on the surface, which is required for the formation of the transition state in ground state ammonia adsorption (see figure 1-2).

Strictly speaking such a limitation is of kinetic origin. Thermodynamically it is favourable to have a full monolayer adsorption of nitrogen. However, after reaching a half monolayer coverage, the ground state adsorption is severely hindered by surface diffusion of adsorbate to free up the necessary pairs of neighbouring vacant sites. Take a C(2×2) ordered, half-covered NH_2/W(100) surface as an example (figure 6-6). The generation of a pair of neighbour vacant sites requires a NH_2 particle to jump into a neighbour vacant site, which is surrounded by three NH_2 adsorbate particles. This surface diffusion is repulsive and the surrounding adsorbates repel this NH_2 particle back into its original position. However, when the newly generated pair of sites is consumed by ground state dissociative adsorption of an ammonia molecule, the diffused NH_2 particle is trapped into its new position. An adsorption coverage beyond half monolayer could be achieved in this way. The repulsive surface diffusion of NH_2 particle into a crowded site is an activated process, facilitated by high crystal temperatures.

In the results reported by Peng and Dawson [1971], the thermal desorption mass spectrometry results on the ammonia adsorption on a polycrystalline tungsten wire at temperature 200 - 700 K displayed a steadily increasing surface nitrogen concentration as the temperature of interaction was increased (figure 6-7).

Referring to table 6-2, the ground state adsorption coverage at 460 and 465 K (~1500 units) is truly higher than those at 320 and 380 K (~1200 units). While the accuracy was limited by the extrapolation of data scattered greatly, qualitatively the trend predicted is observed in the experimental data.

It should be pointed out that in the stimulated adsorption experiments which showed the high ground state coverage were also the ones showing an induction period.

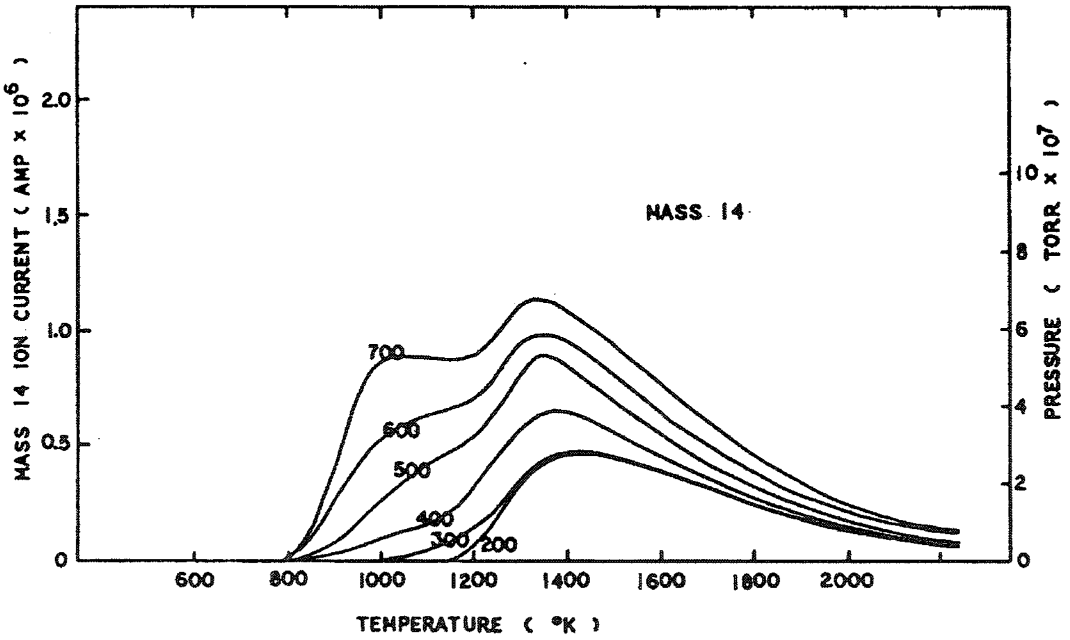

Figure 6-7 Nitrogen desorption spectra from adsorption of ammonia at 10^{-4} torr for 10 min at temperatures between 200 and 700°K. After Peng and Dawson [1971].

6.4.2 Initial stimulated adsorption rate

The initial rate of the stimulated adsorption was found to decrease with an increasing crystal temperature (see figure 6-4 and table 6-2). This decrease must be attributed to a decrease in concentration of the ammonia in the ESA active sites.

The W(100) adsorption data are represented in an Arrhenius plot (figure 6-8). The graph does not give a straight line throughout all the data. There seems to be two separate segments with the break point at about 0.0023 K^{-1} reciprocal temperature (or 430 K in crystal temperature). At the high temperature end a trend line can be drawn with a definite positive slope. At the low temperature end, the data are much less sensitive to the crystal temperature.

The Arrhenius plot for the data on W(110) is shown in figure 6-9 for comparison. Unlike the plot of W(100), there is not an obvious break. The four data points between 300 and 470 K are weakly sensitive to the crystal temperature, similar to the low crystal temperature data on W(100).

6.4.3 Precursor state ammonia

Common understanding of the Arrhenius plot is that the determination of the activation energy of the reaction is the product of the negative of the slope and the gas constant *R*.

$$\Delta E_{\text{act}} = -\ \text{slope} \times R \qquad \ldots (6\text{-}6)$$

The high temperature range (430 – 465 K) of the Arrhenius plot in figure 6-8 shows a definitive positive slope. Upon substituting this slope value in equation 6-6 it gives an apparent activation energy of -120 ± 11 kJ mol^{-1}. Certainly the electron stimulated ammonia dissociation cannot have negative activation energy. In fact the energy value determined is yet more evidence for the existence of the ammonia on an ESA active site. It is the binding energy for ammonia on these sites. A similar treatment

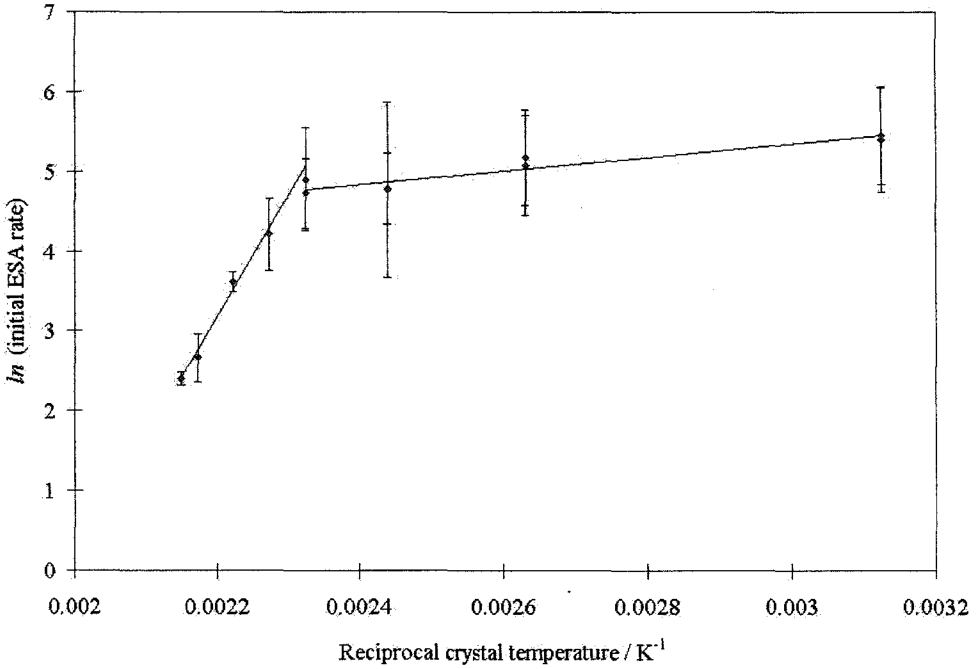

Figure 6-8 The Arrhenius plot for ESA of ammonia on W(100) at P(NH_3) = 1×10^{-7} torr. ΔE_{act} were found as -120 and -7 kJ mol^{-1}. See text for details.

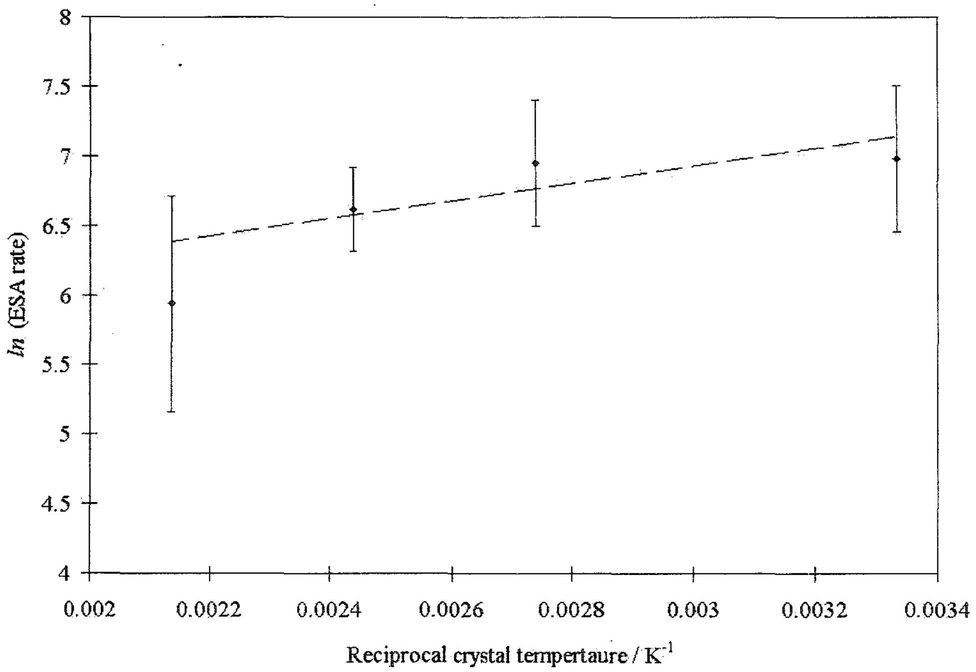

Figure 6-9 The Arrhenius plot for ESA of ammonia on W(110) at P(NH_3) = 3×10^{-7} torr. ΔE_{act} were found as -6 kJ mol^{-1}. See text for details.

to the slope in the low temperature range yields a lower apparent activation energy -7 ± 11 kJ mol^{-1}. This value is the binding energy of ammonia in another adsorption state.

The binding energy of 120 kJ mol^{-1} is quite high. This adsorbed ammonia has to be in a chemisorbed state. This leads to a belief that the ammonia molecule is adsorbed onto the tungsten surface via the lone pair electrons of its nitrogen atom (figure 6-10). No hydrogen bond can be of such high bonding energy.

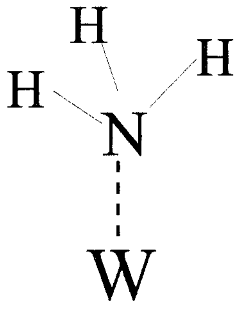

Figure 6-10
Illustration of a N-W bonded ammonia molecule.

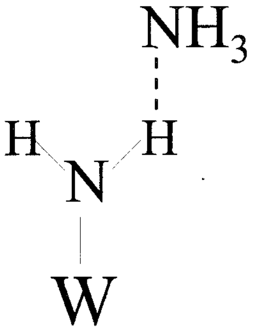

Figure 6-11
Illustration of a hydrogen-bonded ammonia precursor.

As stated earlier, in our Arrhenius plot the linear trend line only covers the high temperature interval from 430 to 465 K. The stimulated adsorption rate only dropped significantly when the crystal temperature increased over ~430 K (reciprocal temperature of 0.0023 K^{-1}). This observation suggests the desorption of this N-W bonded ammonia is not significant at crystal temperature lower than 430 K. It implies that for a pressure of 10^{-7} torr when the crystal temperature is lower than 430 K, there is a saturated adsorption of such N-W bonded ammonia on the crystal surface. The desorption energy is only revealed when the saturation is relaxed at temperature higher than 430 K.

On the other hand, the smaller energy value determined from the low crystal temperature data is likely the binding energy of a hydrogen-bonded, physisorbed precursor state ammonia, NH_3(pc) (figure 6-11). Given the weak interaction between the

NH_3(pc) and the adlayer, the precursor state ammonia will have a freedom of diffusing on the surface within its residence time.

When it reaches a vacant ESA active site, it becomes an ammonia molecule in the ESA active site.

$$NH_3(pc) + *_{act} \xrightarrow{\text{diffusion}} NH_3(act) \qquad \text{... (6-7)}$$

A similar calculation for the W(110) data gives a binding energy of 6 ± 5 kJ mol^{-1} (figure 6-9). The value is very similar to that calculated from the low crystal temperature data on W(100). Therefore it is concluded that this binding energy value is that of a hydrogen-bonded ammonia precursor on W(110). The analysis is reasonable because the hydrogen-bonded ammonia precursors are adsorbed on the adlayer, instead of on the substrate surface itself. The binding energy is determined by the interaction between the adsorbate (NH_3) and the adsorbent (NH_2(ad)), and therefore should not be significantly affected by a difference in the crystal orientation.

The one binding energy value that is going to be affected by the crystal orientation is the N-W bonded ammonia on ESA active sites. The ammonia molecules directly interact with the substrate. Dawson and Hansen [1968] reported in their field emission study that W(110) had a higher work function over any other orientation. The rate of ammonia decomposition was slowest on this most densely packed, highest work function ⟨110⟩ plane. Now it is similarly observed that the ESA rate is slower on W(110) than it is on the W(100). Mentioned in chapter five, the maximum ESA rate at room temperature on W(110) is only 20% of that on W(100). On W(110) there is no observation of an acute rate decrease in the 430-470 K temperature range such as that seen on W(100). This leads to a speculation that the desorption energy of the N-W bonded ammonia in ESA active sites on W(110) is higher than that on W(100).

6.4.4 Induction period

During the initial 10 - 15 minutes of electron irradiation, the nitrogen AES signals did not increase in the stimulated adsorption experiments on W(100) with a high crystal temperature and a low ammonia pressure. The observation was reproducible when the crystal temperature was kept at either 460 or 465 K, and the ammonia pressure kept at 2.0 $\times 10^{-7}$ torr or lower (figures 6-1 (e)-(g) and 6-3 (a)). The length of the induction period seemed to increase with an increasing crystal temperature and a decreasing gas pressure.

It is a general impression that adsorption rates are fastest at the very beginning of the reaction, when the reactants are highest in concentration and not yet depleted by the reaction into products. In fact, this is observed in most other electron stimulated ammonia adsorption experiments at different ammonia pressure and crystal temperature on both W (100) and W(110). The induction period observation, however, is inconsistent with this pattern. The atypical observation of the induction period is thought to be related to the extreme experimental conditions of high crystal temperature and low ammonia pressure, both of which would give a low, yet non-zero, stimulated adsorption rate.

One possible explanation for this observation is that the ESA active sites are actually being generated at the crystal surface during the induction period. So before the number of ESA active sites become sufficient in number, electron stimulated adsorption of ammonia will not happen at a measurable rate, under conditions where this rate would otherwise be small. However, this means that the concentration of ESA active sites is time-dependent, which is contrary to the constant concentration required in the current model to give a constant ESA rate. This casts further doubts on the ESA active site - chemisorption site model beyond the ability to structurally or quantitatively identify both sites. This issue will be further discussed in chapter nine

6.4.5 Apparent final nitrogen coverage

The apparent final nitrogen coverage from electron stimulated ammonia adsorption on tungsten decreases with an increasing crystal temperature in the range 300 – 465 K. In the 460 K experiments, the nitrogen AES signals stayed within 2480 ± 125 units for the last 30 minutes of electron bombardment. The value is far less than the expected saturation coverage value, ~3600 units, acquired in the 320 K adsorption experiments. This suggests the final nitrogen AES values in the experiments with higher crystal temperatures are simply not reflecting a sample surface saturated with ammonia.

The stimulated adsorption rates were already slow in the high temperature experiments. The temperature did not favour the adsorption of ammonia, which is to undergo electron stimulated dissociation. In addition, as the adsorbate coverage increased, the total number of ESA active sites would eventually decrease and thus the rate of electron stimulated adsorption would become very slow. At the high crystal temperature experiments, the rate might simply become immeasurable before the surface reached saturation.

6.5 CONCLUSION

The crystal temperature effects on the kinetics of the electron stimulated ammonia adsorption on tungsten have been studied. It was found the initial rate of stimulated adsorption decreased with an increasing crystal temperature and the adsorption rate became immeasurable when the crystal temperature increased beyond 470 K on both W (100) and W(110).

The ground state ammonia adsorption (pre-electron irradiation) was found to increase with the crystal temperature. Elevated temperature facilitated the N–H bond dissociation and the surface diffusion of adsorbates to open up pairs of neighbouring vacant sites, which were critical in the chemisorption of ammonia on the tungsten surface.

The induction period observation on the stimulated adsorption experiments of extreme ammonia pressure and crystal temperature condition was highlighted.

On the W(100) surface, a binding energy of 120 ± 11 kJ mol^{-1} was determined for ammonia in the ESA active sites from an Arrhenius plot of the data. The molecule was thought to be bonded to the crystal surface through the nitrogen atom. There was a weaker, hydrogen bonded precursor state of binding energy 7 ± 11 kJ mol^{-1} and 6 ± 5 kJ mol^{-1} on W(100) and W(110) respectively.

The apparent final ammonia coverage, on the other hand, decreased with increasing crystal temperature. The adsorption rate approaching saturation simply became very slow and eventually immeasurable. This apparent final ammonia coverage should not be construed as the saturation coverage of stimulated ammonia adsorption.

CHAPTER SEVEN

EFFECTS OF ELECTRON BEAM CURRENT DENSITY ON THE KINETICS OF THE STIMULATED AMMONIA ADSORPTION

7.1 INTRODUCTION

In the previous chapters the effects of the ammonia pressure and the crystal temperature on the adsorption kinetics have been discussed. The remaining experimental controllables are those pertaining to the electron beam.

An electron beam impinging on a gas-covered surface may lead to:

(*i*) Desorption of ions and neutrals, or

(*ii*) Dissociation of the molecules on the surface.

The first process is electron stimulated desorption (ESD). It is an established analysis technique and has been extensively reviewed [Menzel 1995, de Segovia 1996, Burns *et al.* 1996]. The second process is the one of direct relevance to the overall reaction. The electron stimulated dissociation of ammonia leads to its dissociative chemisorption.

Estrup and Anderson [1968] studied the effect of an electron beam on ammonia adsorption on W(100). Their LEED results showed an ammonia-covered C(2×2) NH_2 pattern could change into a P(1×1) pattern upon electron beam irradiation. It was assumed the electron beam dissociated the NH_3 into NH_2 + H, as in the reaction scheme in equation 4-2. In this chapter we will discuss the effect of electron beam current density and examine the effect of beam orientation in the next chapter.

7.2 EXPERIMENTAL METHODS

The electron beam current dependence of the rate of the stimulated adsorption process was investigated with the crystal at room temperature. The ammonia pressure in the vacuum chamber was maintained dynamically at 1.0×10^{-7} torr.

7.2.1 Electron beam current density determination

The variation of the electron beam current was controlled by adjusting the filament voltage of the electron gun. Because the beam voltage and the focus voltage were not changed, the size of the electron beam was kept primarily the same from a beam current of 5 to 25 μA. The beam profile was measured with a Faraday cup in the vacuum chamber. The full width at half maximum (FWHM) value did not change with the beam current. This simplified the analysis, eliminating the need for corrections in the subsequent AES measurements of the nitrogen coverage. The AES measurements were conducted at a standard operating beam current of 25.0 μA.

7.2.2 Surface analysis

With the beam current at 25.0 μA, the standard AES analysis value, the flash-cleaned crystal sample was irradiated by the electron beam in the ammonia environment. AES measurements of surface composition were continuously and simultaneously taken during the ammonia adsorption process. The measured nitrogen AES signals were plotted against the electron irradiation time. The initial N AES signal increase rate, the ground state ammonia coverage and the saturation coverage were determined.

In the stimulated adsorption experiments with electron beam current other than 25.0 μA (the standard AES operating current), the electron beam could only serve to stimulate the ammonia adsorption. No simultaneous AES surface composition analysis was possible.

Following electron beam irradiation of the sample in ammonia gas at, for example, 10.0 μA beam current for 10 minutes, the nitrogen surface concentration was determined at the standard 25.0 μA current. However this analysis could not be performed in the presence of ammonia gas since this would lead to further adsorption. The problem is similar to that discussed in chapter three when investigating ground state ammonia adsorption. It typically would take five to six hours to reduce the ammonia pressure to below 10^{-9} torr using ion and titanium sublimation pumps. This procedure would limit data acquisition to one point for one interaction time at the chosen beam current per day. A method was developed to improve the efficiency of data collection whereby several isolated spots on the crystal surface were exposed for different lengths of time. Then following a single prolonged pump down the nitrogen surface concentration was determined at each point.

It is perhaps worth pointing out that even after the effect of electron irradiation on ammonia adsorption was reported in the 60's [Anderson and Estrup 1968, Estrup and Anderson 1968], there were still researchers who conducted AES measurements on their ammonia adsorbed tungsten samples without specifically reducing the ammonia pressure in advance [May *et al.* 1969, Shindo *et al.* 1980, Reed and Lambert 1984]. Their AES results of the ammonia coverages were likely to be higher than the true coverages.

7.2.3 Experimental procedure for beam currents < 25.0 μA

Shortening the overall experiment time was achieved by a careful experimental design. The lengthy ammonia pumping was still strictly observed to maintain the integrity of the coverage determination, yet the frequency of such pumping was reduced.

Four positions far apart on the crystal surface were selected. Each was 4¼ mm away from its two adjacent neighbours and 6 mm away from its opposite one (figure 7-1).

The clean crystal sample again was exposed to ammonia in the vacuum chamber. The crystal was translated by the XYZ-precision manipulator to align the first selected position to the electron gun. With the shutter opened, this position of the crystal was

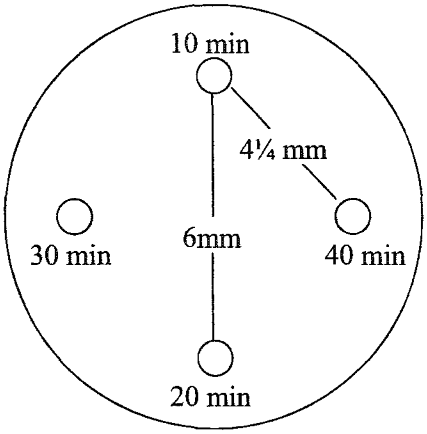

Figure 7-1 Schematic drawing showing the four selected positions on the crystal samples for stimulated ammonia adsorption of different periods.

irradiated by electrons at the specific beam current, for a certain time (*e.g.*, 10 minutes). During this period, the other areas of the crystal surface, including the other three selected positions, were left exposed to ammonia without electron stimulation. At the end of the irradiation period, the shutter in front of the electron gun was closed to conclude the stimulated ammonia adsorption on this part of the sample. The crystal was re-positioned to align the second selected position to the electron gun, and the stimulated ammonia adsorption was performed for a longer period (*e.g.*, 20 minutes). The procedure was repeated until all four selected areas had completed their stimulated adsorption periods with different lengths of electron irradiation time.

The residual ammonia was then pumped out to make AES measurements for the four positions. This experimental design therefore reduced the number of ammonia evacuations from four to one and hence saved three days for every such four experiments.

The stimulated ammonia adsorption experiments were conducted extensively on W(110), for which the adsorption rate was low at room temperature. The range of electron beam current investigated was from 5 to 25 μA. The experiments were not successfully carried out on the W(100) surface, at least not in the same range of beam current. The adsorption rate on W(100) was too fast for this method. In about 15 minutes of electron irradiation the surface approached saturation coverage. The time separations between data points would have been too short to yield reliable results of acceptable uncertainty. Substantially lowering the electron beam current would have slowed down the stimulated adsorption rate. However, the signal-to-noise ratio of each measurement became smaller, as in the low beam current data on the W(110) surface. At the end, the W(100) experiment results were not included, although the results were qualitatively similar – the stimulated adsorption rate increased with the beam current density.

7.3 RESULTS

The measured nitrogen AES signals at the selected spots on the crystals were plotted against the electron irradiation time. The nitrogen AES signals were observed to increase linearly with time in the previous experiments at 25.0 μA and hence a linear trend line was employed to fit the AES data in each adsorption experiment. The results are shown in figure 7-2 for W(110). With only four data points in each graph for its adsorption rate determination, the uncertainty was large, particularly in the low beam current experiments when the nitrogen AES signals were small. The beam currents, the converted beam current densities and the corresponding initial rate of stimulated adsorption are shown in table 7-1.

The calculated initial rates of stimulated ammonia adsorption at each beam current density is plotted in figure 7-3. A weighted, least-square fit linear trend line passes through the data. The reaction order with respect to the electron beam current density is thus determined to be unity.

The slope of the trend line is 12.8 ± 0.7 units min^{-1} $(\mu\text{A mm}^{-2})^{-1}$. 12.8 units of nitrogen AES signal per minute can be converted to a rate of nitrogen surface concentration change of 5.6×10^{10} atoms cm^{-2} s^{-1}. Every $\mu\text{A mm}^{-2}$ is equivalent to 6.24×10^{14} e^- cm^{-2} s^{-1}. The quotient of these two values shows that on W(110), it takes about 10^4 electron collisions onto the sample surface to excite one ammonia molecule to dissociative adsorption.

Figure 7-2 N AES signal evolution graph. W(110), P(NH_3) 1.0×10^{-7} torr. Crystal at room temperature. AES at normal incidence, beam energy 2 keV, different beam current. (a) 25.0 μA, (b) 20.0 μA, (c) 15.0 μA, (d) 11.0 μA, (e) 10.0 μA, (f) 7.5 μA, & (g) 5.0 μA. Four points rate determination method was used on all but the 25.0 μA experiment.

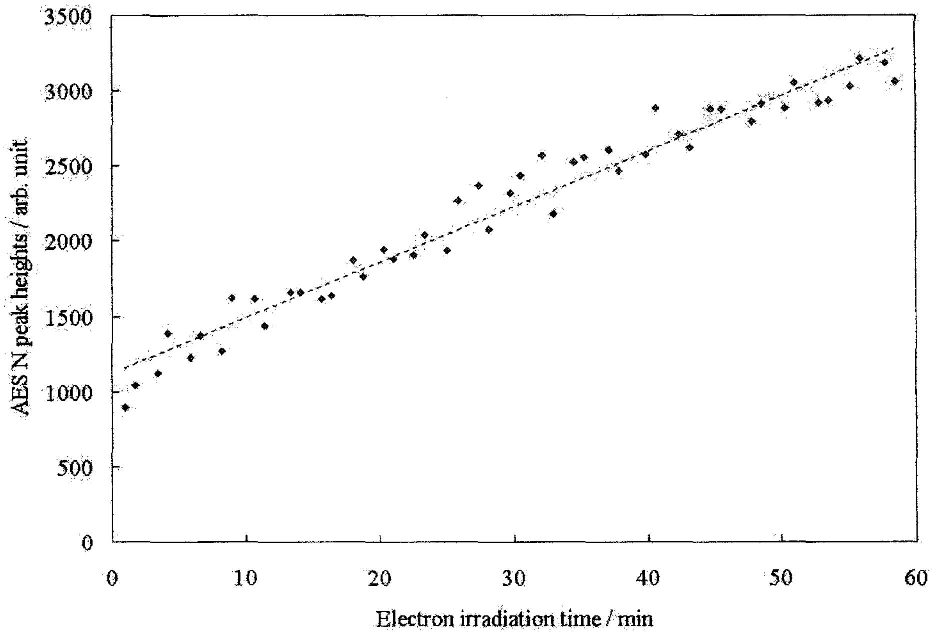

Figure 7-2(a) Beam current = 25.0 μA, (current density = 2.89 μA mm^{-2})

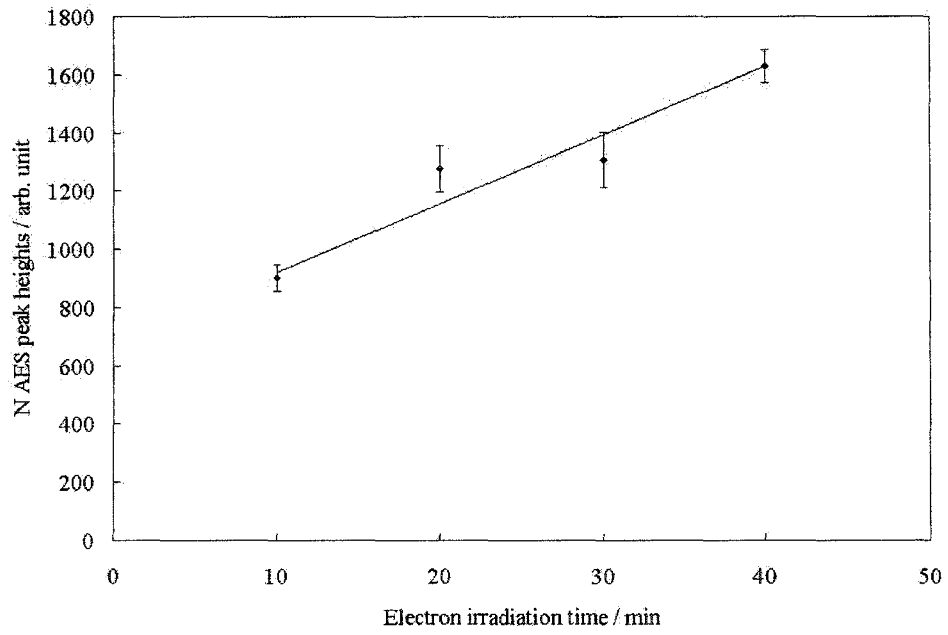

Figure 7-2(b) Beam current = 20.0 μA, (current density = 2.31 μA mm^{-2})

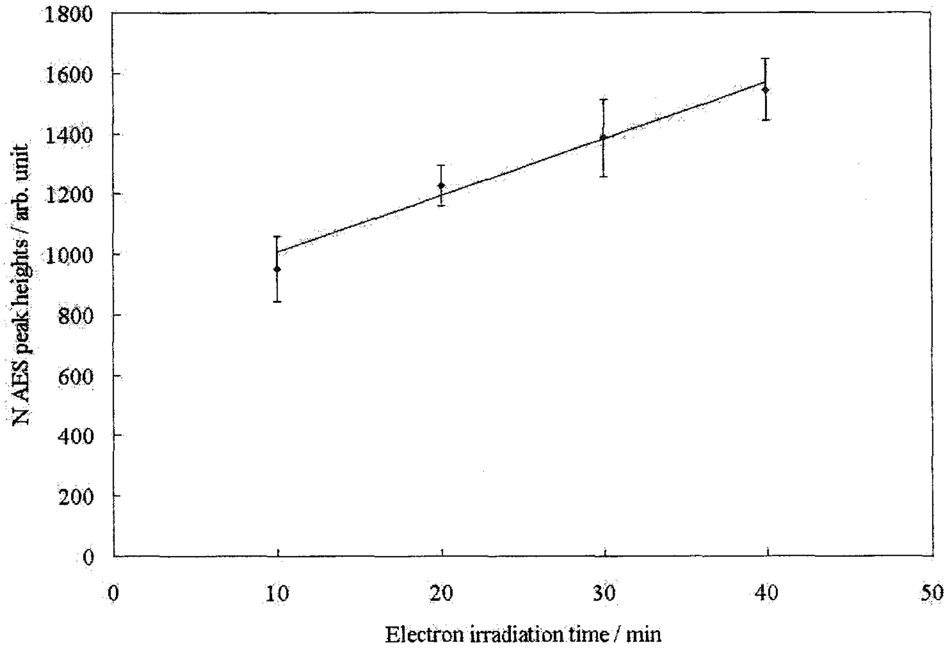

Figure 7-2(c) Beam current = 15.0 μA, (current density = 1.73 μA mm^{-2})

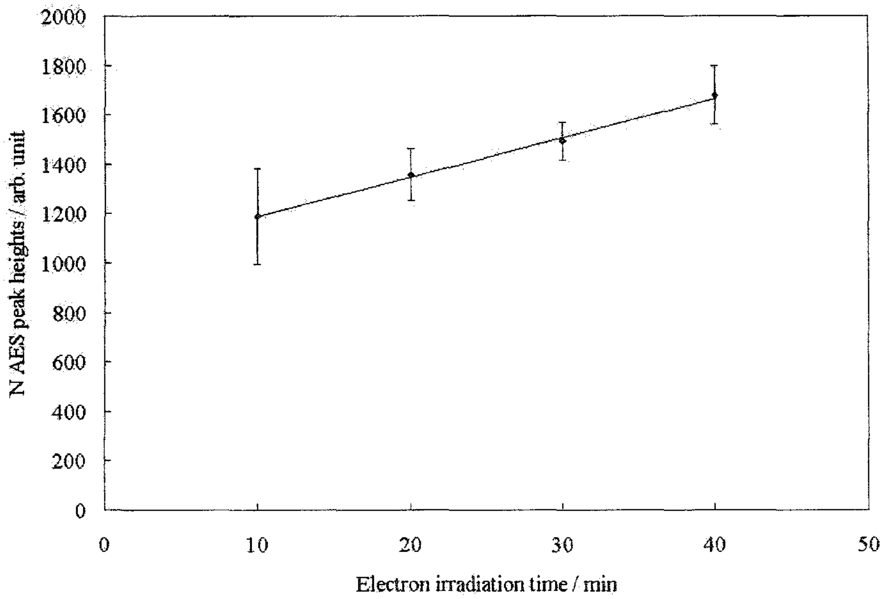

Figure 7-2(d) Beam current = 11.0 μA, (current density = 1.29 μA mm^{-2})

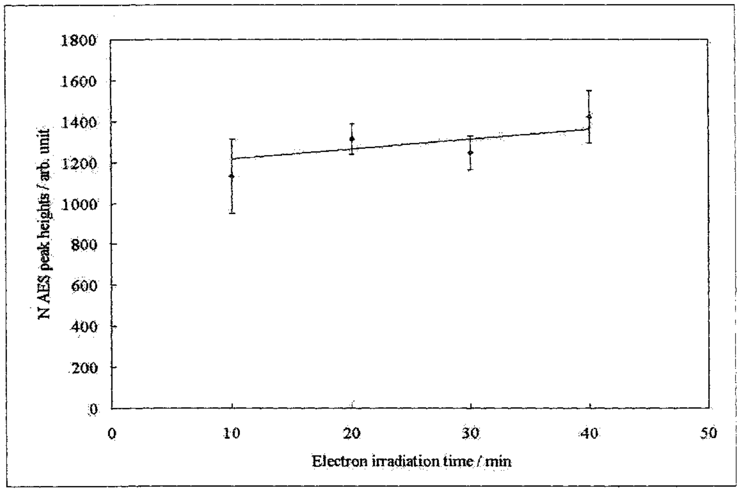

Figure 7-2(e)

Beam current = 10.0 μA, (current density = 1.16 μA mm^{-2})

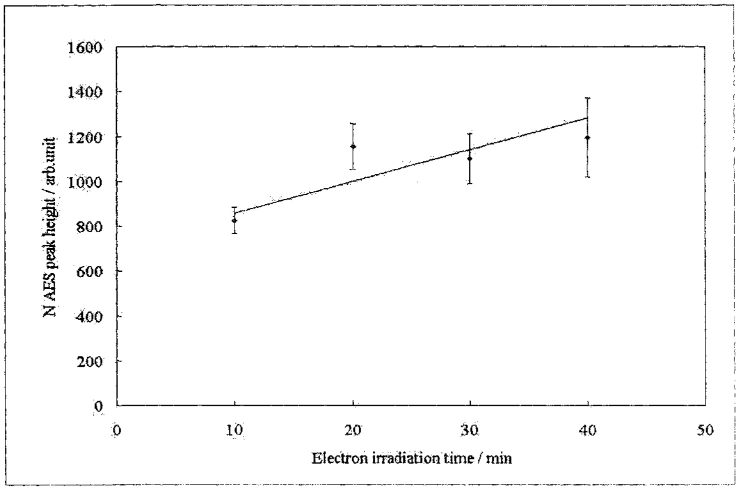

Figure 7-2(f)

Beam current = 7.5 μA, (current density = 0.87 μA mm^{-2})

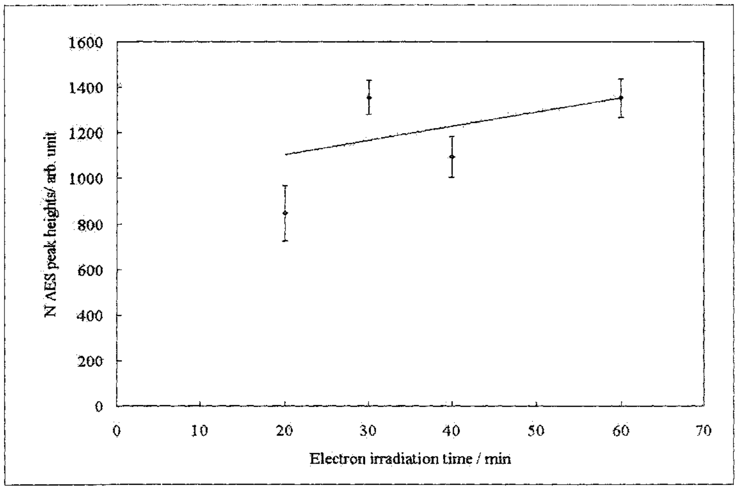

Figure 7-2(g)

Beam current = 5.0 μA, (current density = 0.59 μA mm^{-2})

Beam current / μA	Beam current density / μA mm^{-2}	Initial ESA rate / arb. units per min
25.0	2.89	36.9 ± 1.1
25.0	2.89	35.0 ± 2.8
20.0	2.31	23.6 ± 2.3
15.0	1.73	18.8 ± 2.0
11.0	1.29	15.9 ± 0.6
10.0	1.16	4.8 ± 3.5
7.5	0.87	14.2 ± 4.7
5.0	0.59	6.3 ± 3.1

Table 7-1 The values of the electron beam current, the current density and initial ESA rate.

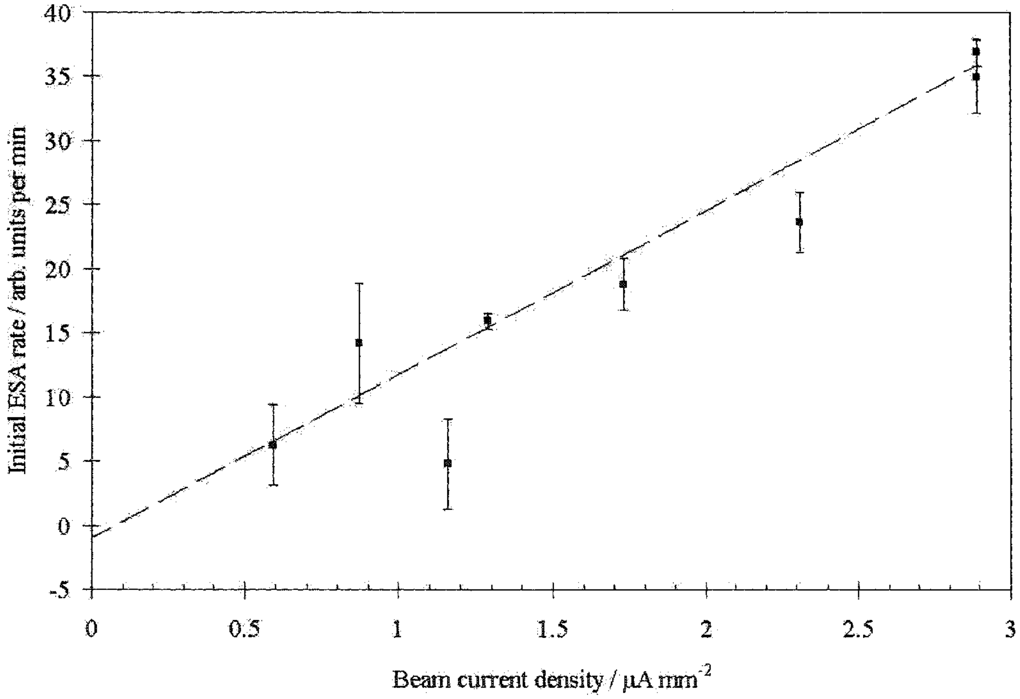

Figure 7-3 The initial ESA rates *vs.* the beam current density of the stimulated ammonia adsorption on W(110) at room temperature. P(NH_3) 1.0×10^{-7} torr. Crystal at room temperature. AES at normal incidence, beam energy 2 keV. A first order relationship is displayed with the weighted, least squares linear fit.

7.4 DISCUSSION

It is observed from figure 7-2 that under the given experimental conditions of a 300 K crystal temperature and 1.0×10^{-7} torr ammonia pressure, the limiting factor is the electron current density. If the beam current had become excessive at a value in the range of study, the initial adsorption rate would not have increased linearly with the beam current from that value onward. It is expected that at some much higher beam current than 25.0 μA this linearity would no longer hold.

7.4.1 Unity reaction order with respect to the beam current density

The reaction order with respect to the beam current density of the electron stimulated ammonia adsorption on W(110) at room temperature is unity.

$$\nu = k \times [e]^{1}$$

Referring to figure 7-3, it is seen that increasing the beam current density increases the initial stimulated adsorption rate. It is arguable that the data may resemble a power law curve instead of a straight line. The choice of a linear fit over a curve is based on:

(*i*) A weighted, least square linear fit that passes though the origin within uncertainty suggests clearly the measured effect is due to electron stimulation. Ground state ammonia adsorption (*i.e.*, adsorption with zero electron beam current density) is not going to yield an adsorption rate with this dependence; and

(*ii*) A first order relationship between the electron beam current density and the stimulated ammonia adsorption rate has a simple interpretation. Such is not the case for a power law relationship between the two.

For comparison, Danielson *et al.* [1978] and Tarasova *et al.* [1994] also reported a first order relationship between the initial adsorption rate and the beam current density in their study of ammonia interaction with Ru(0001) and Si(100). Another report by Sun and Ekerdt [1993] also reported such first order properties of the beam current density, up to 10^{15} e cm^{-2} s^{-1}, in their NH_3 / GaAs(100) system.

7.4.2 One-electron stimulation process

It is not surprising to find the rate of stimulated ammonia adsorption is first order with respect to the electron beam current. The role of electrons in the overall adsorption scheme is to excite the W–NH_3 system from ground state electronic configurations to a more energetic excited state. The excitation is a one-electron process. The probability of an excitation-led ammonia dissociative chemisorption does not change with the frequency of electronic excitation. Therefore increasing the beam current (*i.e.*, the electron bombardment frequency per unit area) increases the frequency of excitations and excitation-led dissociation proportionately. The first order relationship is to be expected.

Should there be a significant contribution from consecutive excitations: an additional excitation to an excited state before it is relaxed, the electron beam current might have exhibited a second order relationship to the initial adsorption rate. This behaviour was not observed in the present experiments nor has consecutive electronic excitation been reported to be a general phenomenon.

7.4.3 Cross-section for electron stimulated ammonia adsorption

Most nitrogen AES signal evolution graphs observed have shown a linear signal increase at the initial stage. The nitrogen signal at any given time t after the start of electron irradiation may be expressed as:

$$N^{AES}(t) = N^{AES}(t=0) + (J\,Q / e) \cdot t \qquad \ldots (7\text{-}1)$$

where N^{AES} ($t = 0$) is the nitrogen AES signal at zero electron irradiation time, J is the electron current density, Q is the cross section and e is an electron charge.

The quotient ($J\, Q \,/\, e$) is thus the slope for each nitrogen AES signal evolution graph, or the initial electron stimulated adsorption rate. When the stimulated adsorption rates were plotted against the electron current density (figure 7-3), the slope of this graph is going to be $Q \,/\, e$. The cross section of the electron stimulated ammonia adsorption on tungsten can therefore be measured by multiplying the slope with e.

The slope in figure 7-3 is 12.8 units (μA mm^{-2})$^{-1}$ min^{-1},

$$\begin{aligned} Q &= 12.8\ (\mu\text{A mm}^{-2})^{-1}\ \text{min}^{-1} \cdot e \\ Q &= 12.8\ (10^{-6}\ \text{A} \cdot 10^{2}\ \text{cm}^{-2})^{-1}\ (60\ \text{s})^{-1} \cdot e \\ Q &= 2.13 \times 10^{3}\ \text{C}^{-1}\ \text{cm}^{2} \cdot e \\ Q &= 3.4 \times 10^{-16}\ \text{cm}^{2} \end{aligned}$$

The result agrees well with the 4×10^{-16} cm^2 reported on NH_3/W(100) by Anderson and Estrup [1968]. This value also compares favourably with the cross section determined from other ammonia systems (1.6×10^{-16} cm^2 on NH_3/Ni(110) [Klauber *et al.* 1985], 6.3×10^{-17} cm^2 on NH_3/GaAs(100) [Sun *et al.* 1993] and 3×10^{-16} cm^2 on NH_3/Rh(0001) [Danielson *et al.* 1978]).

7.5 CONCLUSION

Results for the effect of the beam current density on the kinetics of the electron stimulated ammonia adsorption on W(110) at room temperature have been presented. The reaction order was found to be first order with respect to the beam current density. The cross section for the electron stimulated ammonia adsorption was determined to be 3.4×10^{-16} cm^2.

The variation of the stimulation beam current density in the adsorption experiments made the continuous and simultaneous AES measurements method employed in the previous two chapters unworkable. The electron beam failed to serve a dual purpose as the stimulation electrons for ammonia adsorption and the primary electrons for AES study. A new experimental method was developed to reduce pumping time and speed up data acquisition four times. The integrity of the AES measurements was maintained and considerable effort was spent to prevent the analysis beam from generating extra stimulated ammonia adsorption during the AES measurements.

Until now the electron stimulated ammonia adsorption on W(100) and W(110) has been explained by an ESA active site – chemisorption site model. The model has been able to explain the key observations in the stimulated adsorption experiments, which include:

(i) A consistent coverage-independence on the initial rate of stimulated ammonia adsorption (the model was first introduced to explain this);

(ii) Zero order behaviour at high ammonia pressure from a positive order behavior at low ammonia pressures (saturation of ESA active sites was introduced and integrated with the model).

However, a lingering issue unresolved in this model is the separation between the ESA active sites and the chemisorption sites. It is not clear what properties of the ESA active sites make them a preferential position for the electron stimulated dissociation of ammonia. The ESA active sites must be small in number, present a special environment for ESA and yet be unsuitable for the final chemisorption sites.

Therefore, unless there is other evidence which helps explain the mysterious nature and characteristics of the ESA active sites, this model has to be treated with caution. Fortunately, the experimental results of an investigation about the effects of the angle of incidence of the electron beam will lead to new insight and the possibility of another model which is able to explain the surprising experimental observations. These results remove the burden of dealing with the ESA active site – chemisorption site issue.

CHAPTER EIGHT

ANGLE OF INCIDENCE OF THE ELECTRON BEAM AND THE STIMULATED AMMONIA ADSORPTION

8.1 INTRODUCTION

The dependence of the kinetics of electron stimulated adsorption of ammonia on the intensity of the electron beam was described in the previous chapter. The role played by the angle of incidence of the beam will be investigated in this chapter.

The basic theory of the electron stimulation process has been reviewed in chapter one. Direct momentum transfer from the incident electron to the target adsorbate is not considered to be the primary reason for electron stimulated desorption of the adsorbates. The stimulation process is instead believed to involve Franck-Condon transitions (MGR model) [Menzel and Gomer 1964, Redhead 1964]. Interaction with an incident electron initiates a Franck-Condon transition from the ground state configuration of a substrate-adsorbate system to some excited state. After the electronic excitation, nuclear motion may occur over a time scale of 10^{-13} s, converting potential energy of the new potential surface into kinetic energy. If the adsorbate overcomes the attractive force from the substrate, it desorbs from the surface [Ramsier and Yates, Jr. 1991].

8.1.1 Electron stimulation and adsorption

The initiation of the Franck-Condon transition is the first step of the electron stimulation process and is the only step in which the incident electrons are involved. The incident electrons have two properties that are experimentally controllable. One is the magnitude of the electron beam current density, which has been discussed in chapter seven. The other is the incident angle of the electron beam. In the present W–NH_3 system, the ammonia adsorbates are thought to be weakly adsorbed onto the substrate in an inverted umbrella orientation (figure 8-1). The three outward-pointing N-H bonds are directional with respect to the surface normal, even if free rotation around the principal axis is allowed. The angle between the directional N-H bonds and the incident electron beam may affect the probability of initiating the electron stimulation process.

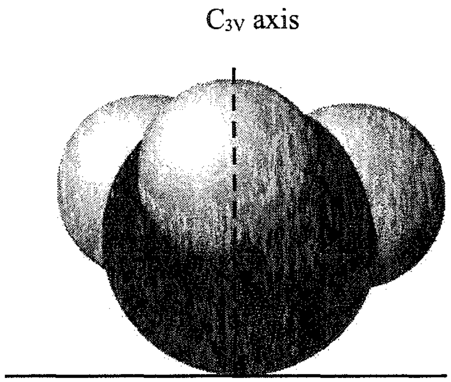

Figure 8-1

Illustration of a side-view of an adsorbed NH_3. Its principal C_{3V} axis is perpendicular to the surface. Each of the three N-H bonds is about 65° away from the C_{3V} axis.

8.1.2 Electron stimulation and enhanced sensitivity of glancing incidence AES

On the other hand, the Auger transitions are also triggered by a primary beam of energetic incident electrons. The ammonia coverage in the stimulated adsorption experiments is determined by AES. The incident angle of this electron beam can affect the magnitude of the AES signals in many ways. One of them is the distance that these electrons travel in the shallow depth over which the low energy Auger electrons can escape. The length of this path is proportional to the number of target atoms the electrons may encounter and ionize. The investigations of the effects of the incident angle of the electron beam are presented in this chapter.

In any Auger transition process, the first step is the core-level ionization of the target atom by an incident primary electron [Barr 1994]. Following the ionization, the non-radiative Auger relaxation is not affected by any properties of this incident electron. Therefore when the Auger analysis is affected by the angle of incidence of the primary electron beam, it is the core-level ionization process that is affected.

Auger transitions are detectable only when they happen near the substrate surface. The critical depth depends on the characteristic energy of the Auger electrons. This critical depth is referred to as the Auger sensitive layer in the following discussion. Regardless of the incident angle of the primary electron beam, the high-energy electrons would penetrate to a much larger depth. However, any Auger electrons emitted beyond the Auger sensitive layer do not make a contribution to the collected Auger current. These electrons lose their characteristic energy (180 eV for W_{NNN} transition) via inelastic collisions before leaving the sample to the vacuum.

The number of W_{NNN} Auger transitions increases when the primary electrons collide with more tungsten atoms in the substrate surface layer, and induce more core-level ionizations. The length of the path these primary electrons travel in the Auger sensitive layer, however, depends on the incident angle of the electron beam. By simple trigonometry and referring to figure 8-2, a G.I. electron beam travels $(\cos\theta)^{-1}$ farther in the Auger sensitive layer than an N.I. electron beam does. In the present experiments the off-normal incidence angle is 75°, and $(\cos 75°)^{-1} = 3.86$. The analysis thus indicates that the electrons in this G.I. primary electron beam will encounter 3.86 times more tungsten atoms than the N.I. primary beam, in the Auger sensitive layer. In principle, this will make the tungsten AES signal generated by the G.I. primary beam 3.86 times stronger than that generated by the N.I. beam.

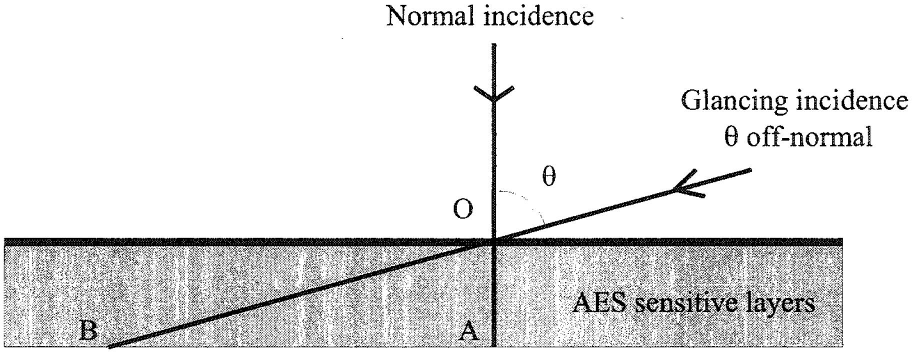

Figure 8-2 Illustration of the travel paths of the normal incidence (OA) and the glancing incidence electrons (OB). OA = OB cos θ.

In addition, an electron back-scattering factor also affects the Auger analysis when the angle of incidence of the primary electron beam is varied. The primary electrons will scatter elastically and inelastically as they penetrate into the sample. Many of them scatter inelastically back toward the surface. Figure 8-3 demonstrates this effect qualitatively [Bishop 1965, Neave *et al.* 1972]. The contours of equal primary electron energy loss illustrates that the distribution tends to decrease exponentially as the radial displacement increases. At glancing incidence a large proportion of high-energy back-scattered electrons are formed close to the surface. Only electrons of high energy can initiate core-level ionization and generate Auger electrons. At normal incidence, with increasing primary energy, high-energy electrons are formed at increasing depths in the solid and consequently far fewer back diffuse without further loss to the region from which Auger electrons can escape.

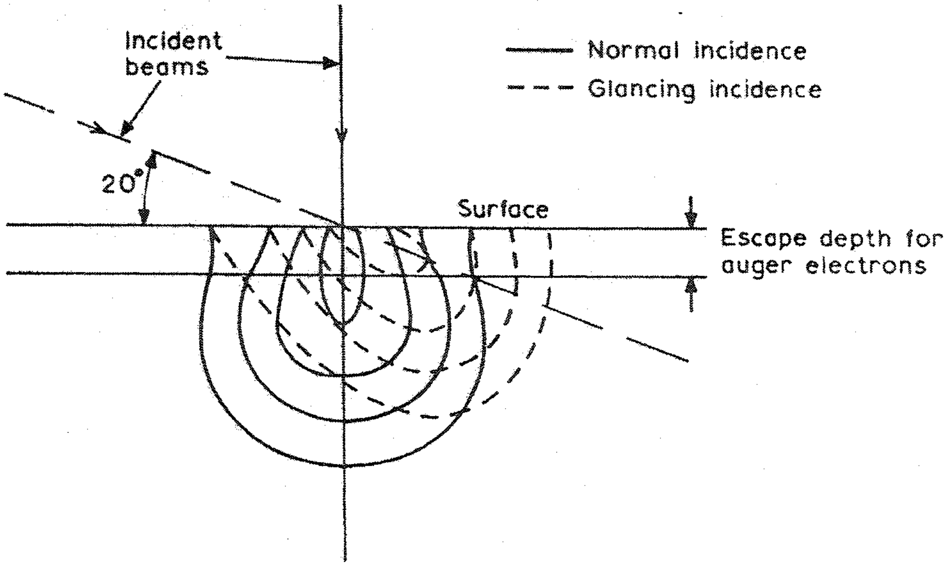

Figure 8-3 Schematic diagram of contours of equal primary electron energy loss, showing the effect of using normal and glancing incidence electron beam. After Neave *et al.* [1971].

8.2 EXPERIMENTAL PROCEDURES

Electron stimulated ammonia adsorption experiments were all performed using the same experimental conditions with a 300 K crystal temperature and a 1.0×10^{-7} torr ammonia pressure. The surface composition was continuously monitored by AES during the adsorption experiments. The experimental controllable varied in this series of experiments was the angle of incidence of the electron beam. In some experiments, as with all those described so far, the electron gun at normal incidence (N.I.) to the substrate surface was used to generate the electron beam for the stimulated adsorption. In other experiments, a glancing incidence (G.I.) electron gun was used (figure 2-7), directed at 75° off-normal incidence to the surface (figure 8-2, $\theta = 75°$).

A minor difference between the two electron beams was the beam energy. The N.I. electron beam was of energy 2.0 keV. The beam energy of the glancing incidence beam was slightly lower at 1.8 keV. During the time of the experiments the control unit of the G.I. electron gun was unable to keep a stable 2.0 keV beam energy. To determine if and how much effect was a difference of 0.2 keV in beam energy on the AES measurements, three Auger spectra of different beam energy (1.6, 1.8 and 2.0 keV) were collected from a nitrogen-covered sample by the N.I. electron gun. No difference was observed in the size and energy of the nitrogen and tungsten AES peaks. A difference of 0.2 keV beam energy was therefore considered negligible.

8.3 RESULTS

The AES signal evolutions acquired during the stimulated adsorption experiments on W(100) are shown collectively in figure 8-4, for both normal and glancing incidence electron beams. The data of the experiments on W(110) are shown in figure 8-5. The key numerical data acquired from the experimental results are shown in tables 8-1 and 8-2 for the two orientations respectively.

The results on different orientations are qualitatively similar. The fast adsorption rate on W(100) at room temperature limited the number of AES data that can be used to determine the initial adsorption rate. This in turn increases the uncertainty. In the following discussion, emphasis will be put on the data on the W(110) surface because of the better precision.

8.3.1 Tungsten AES signals

The tungsten AES signals decreased as the electron stimulated ammonia adsorption proceeded on the crystal surfaces. As the adsorbate coverage increased, more tungsten surface atoms were covered, causing this decrease in the tungsten AES signals. The change in the tungsten AES signals against electron irradiation time generally mirrored the linearity displayed in the nitrogen AES signals. The period of linear AES signal change matched that of the nitrogen AES signals as well (~45 and 20 minutes in the N.I. and G.I. experiment on W(110) respectively, figure 8-5; and less than 10 minutes in both experiments on W(100), figure 8-4).

The initial tungsten AES signals, unlike their nitrogen counterparts, were largely different in magnitude in the two adsorption experiments with electron beams of different angle of incidence. The tungsten signal in the G.I. experiment was nearly three times as large as that in the N.I. experiment, $\left.\frac{\text{G.I.(W)}}{\text{N.I.(W)}}\right|_{t_0}^{110} = 2.7$. There was no reason to believe any

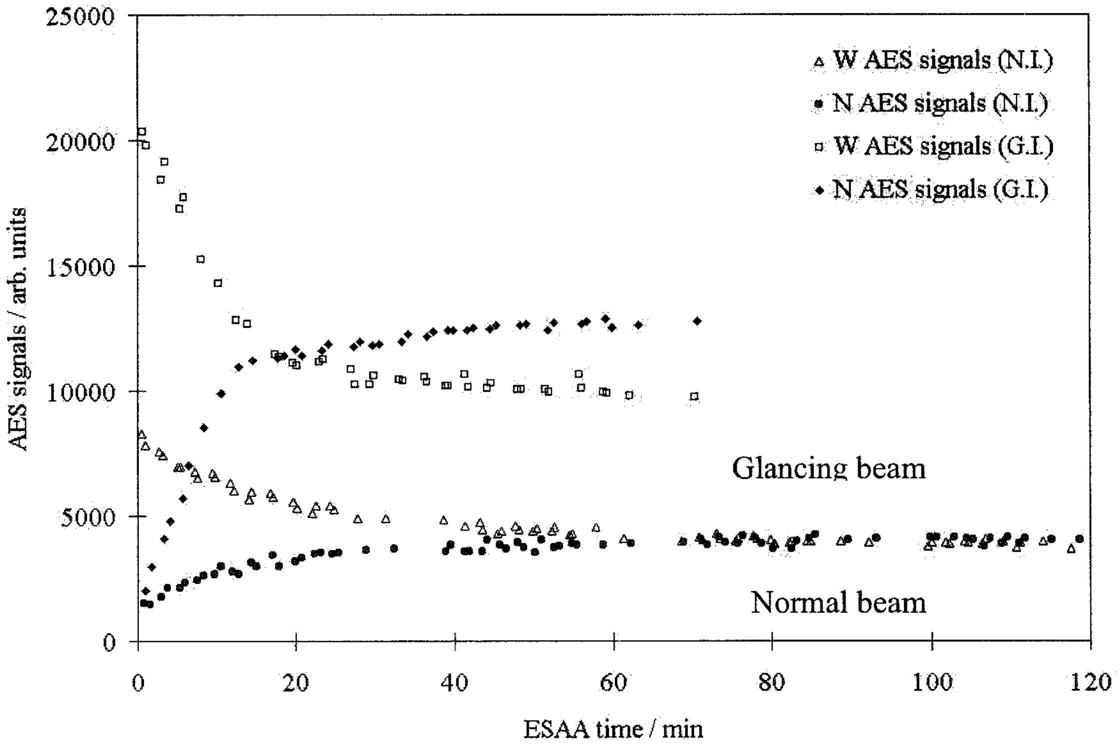

Figure 8-4 The AES signals evolution graph displaying both electron stimulated ammonia adsorption experiments on W(100) at room temperature and in 1.0×10^{-7} torr of ammonia. The details of the two electron beams were discussed in the text.

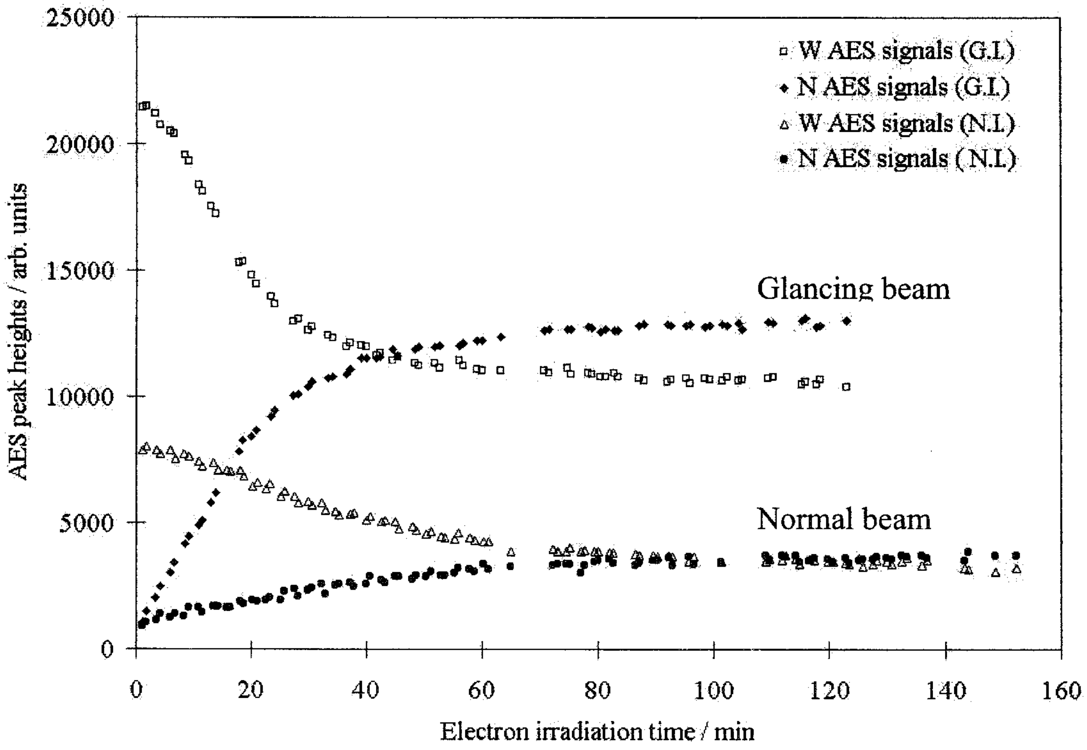

Figure 8-5 The AES signals evolution graph displaying both electron stimulated ammonia adsorption experiments on W(110) at room temperature and in 1×10^{-7} torr NH_3.

	Normal incidence	Glancing incidence
Initial rate of N AES signal increase / arb. units per min.	144 ± 6	850 ± 45
NH_3 coverage by ground state adsorption / arb. units	1370 ± 70	1260 ± 210
NH_3 saturation coverage / arb. units	4030 ± 110	12700 ± 130
Initial W AES signal [1]/ arb. units	8070 ± 240	20090 ± 270
Final W AES signal [2]/ arb. units	3920 ± 110	10020 ± 330

[1] The tungsten AES signal measured from the ammonia-covered (by ground state adsorption) surface.

[2] The tungsten AES signal measured from the sample surface saturated with ammonia by electron stimulated adsorption at room temperature.

Table 8-1 The effect of angle of incidence on key features of the AES evolution curves of figure 8-4 for the adsorption experiments on W(100).

	Normal incidence	Glancing incidence
Initial rate of N AES signal increase / arb. units per min.	41.5 ± 1.3	393 ± 5
NH_3 coverage by ground state adsorption / arb. units	1070 ± 30	780 ± 60
NH_3 saturation coverage / arb. units	3630 ± 110	12880 ± 115
Initial W AES signal / arb. units	7910 ± 80	21360 ± 170
Final W AES signal / arb. units	3370 ± 160	10650 ± 120

Table 8-2 The effect of angle of incidence on key features of the AES evolution curves of figure 8-5 for the adsorption experiments on W(110).

difference in the surface composition before electron irradiation, and therefore this difference was attributed to the enhanced Auger sensitivity with a primary electron beam at G.I. to the substrate surface discussed earlier in section 8.1.2.

The ratio at the end of the stimulated adsorption was also approximately three, $\left.\frac{\text{G.I.(W)}}{\text{N.I.(W)}}\right|_{t\infty}^{110} = 3.2$. These same ratios were to be expected, given that the same saturated ammonia adsorbed surface will be produced, regardless of the incident angle of the electron beams. In summary, both tungsten AES signal ratios agree with the predicted $(\cos\theta)^{-1}$ value.

It is important to remember these initial tungsten AES signals were not a result of a clean, bare tungsten surface, but a surface partially covered with ammonia (via ground state adsorption for a few minutes). In fact, when the tungsten AES signals for clean W(110) surface is compared, the signal ratio $\left.\frac{\text{G.I.(W)}}{\text{N.I.(W)}}\right|_{\text{clean}}^{110}$ yields a value of 4.1. This value actually is easier to interpret than both $\left.\frac{\text{G.I.(W)}}{\text{N.I.(W)}}\right|_{t0}^{110}$ and $\left.\frac{\text{G.I.(W)}}{\text{N.I.(W)}}\right|_{t\infty}^{110}$. Auger electron spectroscopy is a very surface sensitive analytical technique. Generally the signal weakens exponentially with the depth of the origins of the characteristic Auger electrons. The topmost layer contributes greater to the overall signal. In the $t = 0$ and ∞ cases, the tungsten surface is half and fully covered by ammonia and nitrogen respectively. The AES signals are certainly attenuated by the nitrogen adlayer, more seriously in the glancing incidence experiments than in the normal incidence ones. Hence the signal ratios are somewhat less than the expected $(\cos\theta)^{-1}$ value.

While on the clean tungsten surface, the signal ratio of 4.1 includes the $(\cos\theta)^{-1}$ expectation and the electron back-scattering effect. Both favour the glancing incidence AES signals, and so results in a $\left.\frac{\text{G.I.(W)}}{\text{N.I.(W)}}\right|_{\text{clean}}^{110}$ signal ratio greater than $(\cos\theta)^{-1}$.

8.3.2 Nitrogen AES signals

Both N.I. and G.I. nitrogen AES signal evolution series displayed a coverage-independent initial signal increase against the electron irradiation time. This feature was commonly observed in the results described in earlier chapters.

Despite the same beam currents of 25.0 μA in both experiments, the glancing incidence AES signals were seen generally bigger than the N.I. AES signals at the same electron irradiation time. At the end of the stimulated adsorption the nitrogen AES signal ratio, $\left.\frac{\text{G.I.(N)}}{\text{N.I.(N)}}\right|_{t_\infty}^{110}$, was 3.5, which again agreed with the predicted $(\cos\theta)^{-1}$ value.

There was one notable exception to the approximate $(\cos\theta)^{-1}$ signal ratio and this was at the beginning of the adsorption experiment, when the G.I. signal was only 1070 units, within error no different from the 780 units for the N.I. signal. The signal ratio $\left.\frac{\text{G.I.(N)}}{\text{N.I.(N)}}\right|_{t_0}^{110}$ was only 1.4, significantly smaller than the predicted $(\cos\theta)^{-1}$ value. The nitrogen AES signal ratio at zero electron irradiation time was definitely different from the other three mentioned earlier.

In fact, the ratio $\left.\frac{\text{G.I.(N)}}{\text{N.I.(N)}}\right|_{t}^{110}$ was continuously changing during the stimulated adsorption experiment (figure 8-6). The signal ratio increased from about unity at the beginning of the experiments to nearly five in about 30 minutes of electron irradiation time. The signal ratio increase was linear in the first 25 minutes, matching the length of the period in which the glancing incidence AES signal increase was also linear. After reaching a maximum of five, the signal ratio gradually decreased. The decrease stopped at about 90 minutes of electron irradiation time and stabilized at a ratio of about 3.7 in the next 30 minutes. This large variation of the nitrogen AES signal ratio and, more importantly, a unity initial signal ratio were unexpected.

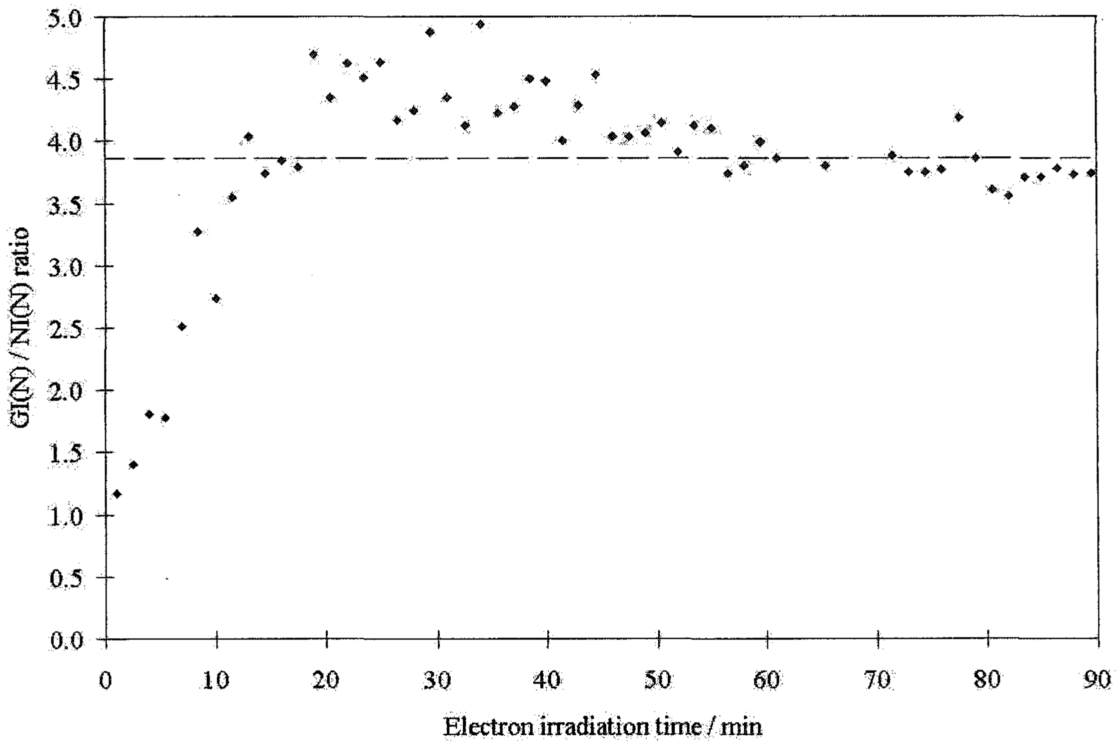

Figure 8-6 The ratio of the N AES signals, $\left.\frac{\mathrm{G.I.(N)}}{\mathrm{N.I.(N)}}\right|_t^{110}$, at the same electron irradiation time acquired in the glancing and normal incidence AES analysis during the electron stimulated ammonia adsorption experiments on W(110).
The individual N AES signals were shown in figure 8-5. The dotted line indicates the value of $(\cos 75°)^{-1}$.

For comparison purpose, the evolution of the nitrogen AES signal ratio on W (100), $\left.\frac{\mathrm{G.I.(N)}}{\mathrm{N.I.(N)}}\right|_t^{100}$, against electron irradiation time are shown in figure 8-7. The profile is qualitatively similar to the data of the adsorption experiments on W(110). Because of its fast initial adsorption rate, the AES signal ratio reached its peak in a short 15 minutes, compared to approximately 30 minutes in the experiments on W(110). The maximum signal ratio was smaller, at 3.9, compared to ~5 on W(110). The final signal ratio was also smaller at 3.3, compared to ~3.7 on W(110). The differences, however, did not affect the general interpretation of the evolution graphs.

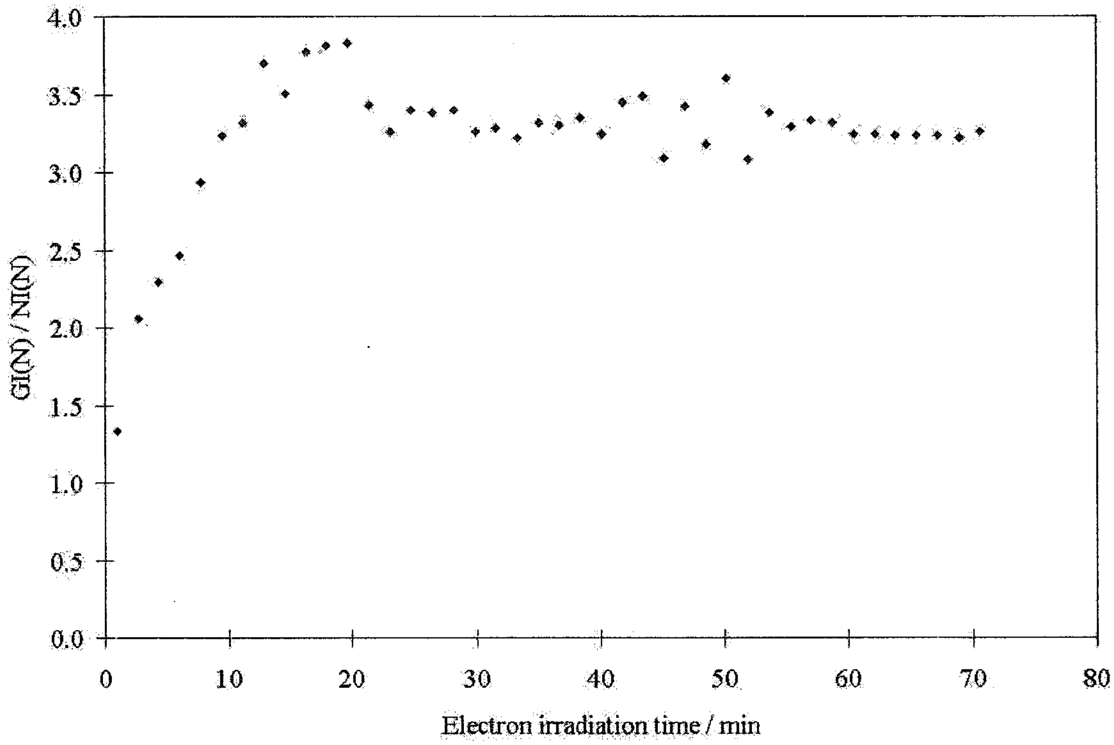

Figure 8-7 The ratio of the N AES signals, $\left.\frac{\text{G.I.(N)}}{\text{N.I.(N)}}\right|_{t}^{100}$, at the same electron irradiation time acquired in the glancing and normal incidence AES analysis during the electron stimulated ammonia adsorption experiments on W(100). The individual N AES signals were shown in figure 8-4.

8.4 DISCUSSION

The differences in the two nitrogen AES signals in the N.I. and G.I. electron stimulated ammonia adsorption experiments are surprising. The following discussion begins with a consideration of whether the stimulated adsorption itself, and not the analysis measurement, is affected by electron beams of different incidence angle. This is followed by a discussion of the origin and the magnitude of the AES sensitivity in using a glancing incidence electron beam in Auger analysis. This will be followed by an explanation of the large variation of the nitrogen AES signal ratio observed in figure 8-6.

8.4.1 Variation of nitrogen AES signal ratio

When the nitrogen AES signals in the two experiments are compared at electron irradiation time *t* throughout the experiments, the signal ratio $\left.\frac{\text{G.I.(N)}}{\text{N.I.(N)}}\right|_t$ is continuously changing. One possibility is simply that the surface compositions at time *t* were different in the N.I. and G.I. adsorption experiments. This would indicate the electron stimulated ammonia adsorption kinetics depend on the incident angle of the incident electrons. The alignment of the N-H bonds in the ammonia adsorbates and the path of the stimulation electrons then determined the N-H bond dissociation probability. A higher initial rate of nitrogen AES signal change was observed for the G.I. electron beam experiments and this implies the "head on" alignment between the N-H bonds and the electron beam enhances the adsorption rate over the "sideways" alignment (figure 8-8).

Another possibility is that the properties being affected by the angle of incidence of the electron beam is not the stimulated reactions but the Auger analysis. In the following section we will discuss how the first option (*i.e.*, effect on ESA) alone is ruled out and how the second option (*i.e.*, effect on AES) is preferred.

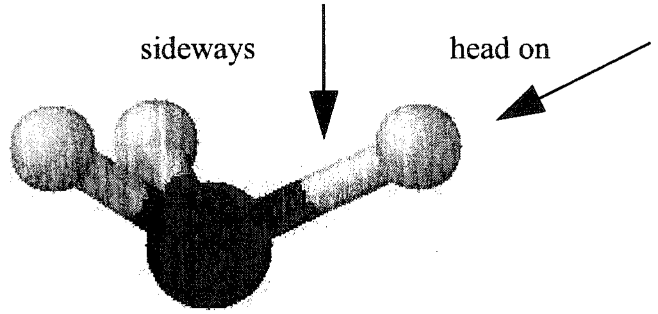

Figure 8-8 A diagram illustrating the two possible ways of electron collision on an adsorbed ammonia molecule. The arrows indicate the incident trajectories of the electrons. "Head on" refers to the electron course parallels the N-H bond. "Sideways" refers to the electron course nearly perpendicular to the N-H bond.

The surface composition of the sample is not affected by the electron beam at t_0 and t_∞, when the surface is only covered with ground state adsorbed ammonia and when the surface is saturated with electron stimulated adsorbed ammonia. The electron beam has not yet affected the adsorption process in the former and has completed its effect in the latter. If the angle of incidence of the electron beam affects only the ESA process and not the Auger analysis, the measured nitrogen AES signal ratio ($\left.\frac{\text{G.I.(N)}}{\text{N.I.(N)}}\right|_{t}$) is going to be of the same value whether $t = 0$ or ∞. Obviously, the experimental results do not agree with this interpretation. On W(100), $\left.\frac{\text{G.I.(N)}}{\text{N.I.(N)}}\right|_{t_0}^{100}$ is 1.3 while $\left.\frac{\text{G.I.(N)}}{\text{N.I.(N)}}\right|_{t_\infty}^{100}$ is 3.3 (figure 8-7). On W (110), the difference is even greater. $\left.\frac{\text{G.I.(N)}}{\text{N.I.(N)}}\right|_{t_0}^{110}$ and $\left.\frac{\text{G.I.(N)}}{\text{N.I.(N)}}\right|_{t_\infty}^{110}$ are of values 1.1 and 3.5 respectively (figure 8-6).

Moreover, the electron stimulated ammonia adsorption reached completion (*i.e.*, the nitrogen AES signal reached its maximum size) in approximately the same beam irradiation time regardless of the angle of incidence of the electron beam. This suggests the incident angle of the electron beam does not affect the adsorption kinetics. Any explanation invoking differences in kinetics for the G.I. and N.I. beams is incapable of explaining the anomaly at $t = 0$. We are forced to look at the alternative possibility of different Auger sensitivity factors for the two beam orientations which change with surface composition.

8.4.2 Stepwise ammonia dissociation to nitrogen

An alternative explanation for the strange variation in the $\frac{\text{G.I.(N)}}{\text{N.I.(N)}}$ signal ratio of figures 8-6 and 8-7 could arise from different nitrogen Auger sensitivities during the adsorption period. At the beginning of the experiment the surface species will be NH_3 from ground state adsorption, or possibly NH_2 if the adsorption is dissociative. Throughout electron beam irradiation, N–H bond breaking will lead to a progression of NH_X species through NH and finally leaving a surface saturated with bare N species. If the G.I. and N.I. nitrogen Auger sensitivities for $NH_{2\text{ or }3}$, NH and N are different it may be possible to account for the observed variation in figures 8-4 to 8-7.

Adsorbed ammonia is dissociated via electron stimulation of the sample surface:

$$\underset{*}{NH_3} \xrightarrow{e} \underset{*}{NH_2} + H$$

The ultimate location of the dissociated H atoms is not considered here. The electron stimulated reaction does not just stop after the dissociative chemisorption. Instead, the stimulated dissociation continues and degrades the NH_2 to NH, and eventually N:

$$\underset{*}{NH_2} \xrightarrow{e} \underset{*}{NH} \xrightarrow{e} \underset{*}{N}$$

Upon completion of electron stimulated adsorption the substrate surface is covered with bare nitrogen adatoms, every hydrogen atom having been stripped away. The bare nitrogen adatoms are the topmost layer. The primary incident electrons from both electron guns can reach the nitrogen atoms with no attenuation. These primary electrons initiate Auger transitions and stimulate ammonia adsorption. The angular dependence of this electron irradiation is important. Before the saturated adsorption is reached, during the experiments the surface is adsorbed with a mix of NH_3, NH_2, NH and N. All of them are the topmost layer adsorbates. However, unlike the bare nitrogen adatoms, N(ad), the nitrogen atoms of the adsorbates NH_3, NH_2 and NH are not the topmost atoms. These three adsorbates are all oriented to interact with the substrate surface via the nitrogen atom. The bonded hydrogen atom(s) is/are pointed away from the crystal surface. In effect the topmost atoms of these adsorbates are the hydrogen atom(s). NH_3 is of an inverted umbrella shape (figure 8-1). NH_2 is *V*-shaped (figure 8-9) and NH has the only hydrogen atom right on top of the nitrogen atom (figure 8-10).

Our investigation is directed at how these hydrogen atoms affect the angle dependence of the incident electron beam of the Auger transitions or the stimulated dissociation. Visualizing the geometric orientation of individual NH_X gives a hint as to how and why these different adsorbates respond differently in the (nitrogen) Auger analysis, even though they all contain a single nitrogen atom.

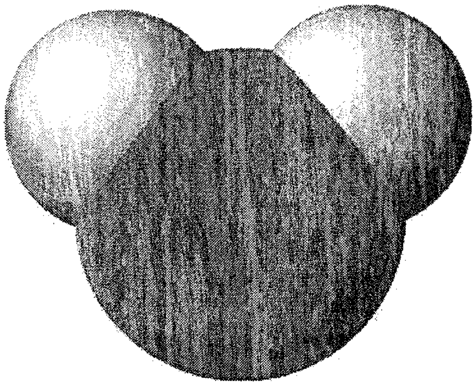

Figure 8-9 Illustration of a side-view of a *V*-shaped adsorbed NH_2.

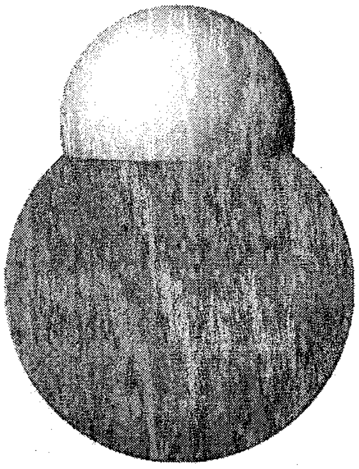

Figure 8-10 Illustration of the side-view of an adsorbed NH.

8.4.3 AES sensitivity and the angle of incidence of the primary electron beam

The number of hydrogen atoms, the *molecular* geometry of the NH_X adsorbates and the incident angle of the primary electron beam are related and discussed in this subsection. The difference in the response to the nitrogen AES signals is quantified with an AES sensitivity factor.

8.4.3.1 *Normal incidence beam Auger analysis of NH_X species*

The top views of the space-filling models of adsorbed NH_3, NH_2 and NH are shown in figure 8-11.

The sensitivity of the nitrogen AES signal for each of these adsorbates depends on the degree of openness or exposure of the nitrogen atom to the primary electron beam. Viewing from above, a larger proportion of the nitrogen atoms (the darker shade) are exposed on the adsorbed NH_3 and NH_2 than on the adsorbed NH. It should be noted the number of bonded hydrogen atoms does not play a significant role in this discussion.

The sensitivity of the nitrogen AES signal depends on how exposed the nitrogen atom is under the *shielding* of the hydrogen atoms above it. This hydrogen shielding is a measure of the number of hydrogen atoms, as well as the relative alignment of the N-H

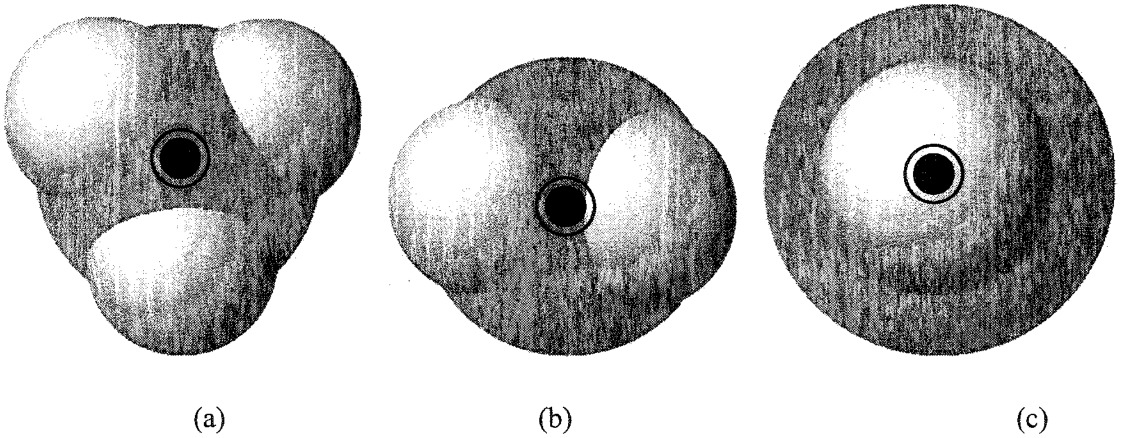
(a) (b) (c)

Figure 8-11 The top views of the adsorbed (a) NH_3, (b) NH_2 and (c) NH.
The black dot in each figure is meant to represent the normal incidence electron, pointing into the paper.

bonds and the incident angle of the electron beam. The adsorbed NH_3 and NH_2 should yield similar nitrogen AES sensitivity when the Auger analyses are conducted with an electron beam at normal incidence to the sample surface. The difference in the number of hydrogen atoms is compensated by a difference in the H-N-H bond angle. The adsorbed NH, however, may yield a much lower (nitrogen) AES sensitivity over the other two adsorbates. While its number of hydrogen atoms is the least among the three degrading NH_X adsorbates, its on-top orientation puts the screening hydrogen atom directly in the way of the incident electrons. This more direct interference decreases the number of incident electrons reaching the nitrogen atom underneath more severely in NH than in NH_3 or NH_2. The result is a smaller proportion of the primary electrons can induce N_{KLL} Auger transitions and thus leads to a smaller AES sensitivity.

8.4.3.2 *Glancing incidence beam Auger analysis of NH_X species*

The top views of the space-filling models of adsorbed NH_3, NH_2 and NH in figure 8-11 are no longer appropriate in discussing the Auger sensitivity in the glancing incidence beam Auger analysis. The glancing incidence electron beam is 75° off the surface normal (figure 8-2). The side views of the space-filling models of the adsorbed NH_3, NH_2 and NH are displayed in figure 8-12.

The AES sensitivities of the adsorbed NH_3 and NH_2 can be collectively discussed. With the 75° off-normal glancing incidence electron beam, the hydrogen atoms are clearly obstructing the incident electrons path to the nitrogen atom. The intersection angle between the N-H bonds and the electron beam is only ~10°. Either free rotation of hydrogen atoms around the principal axis or rigid adsorption with random orientation will have a partial hydrogen screening effect exerted on the nitrogen atom, up to a maximum of one hydrogen atom equivalence. The effect therefore can be as strong as in the "head on" alignment of the adsorbed NH for the normal incidence electron beam in the previous sub-section. The hydrogen atoms screen a major proportion of the bonded nitrogen atoms underneath. On the other hand, the on-top hydrogen atom of the adsorbed NH is far away from the glancing incidence electron beam. The hydrogen atom thus only negligibly shields the nitrogen atom underneath from being bombarded by the primary electrons. The number of induced N_{KLL} Auger transition is high and so is the nitrogen Auger sensitivity. In fact its sensitivity is thought to be similar to that of a bare nitrogen adatom, although there will be some screening from H atoms on adjacent species.

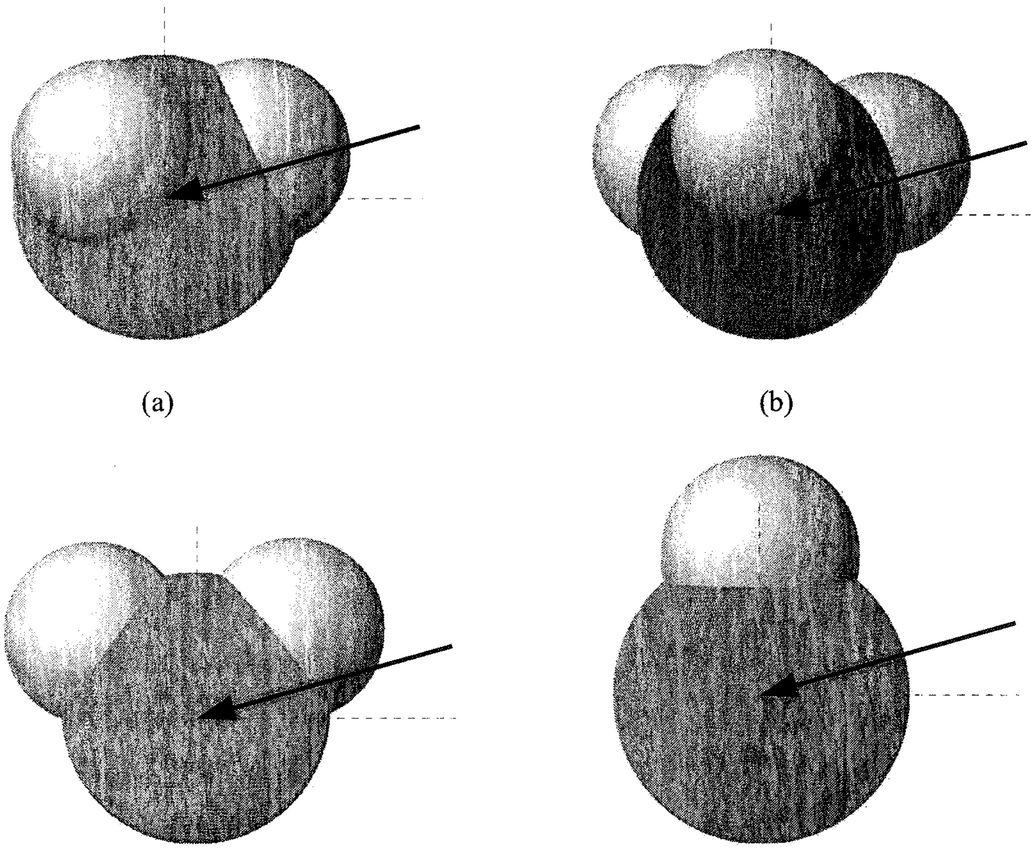

(a) (b)

(c) (d)

Figure 8-12 The side views of the adsorbed (a) & (b) NH_3, (c) NH_2 and (d) NH. The vertical and horizontal dotted lines in each diagram represent the surface normal and the surface plane originating from the centre of the nitrogen atom, for illustrative purpose. The arrow represents the 75° off-normal glancing incidence electron beam.

schematic diagram (figure 8-13). Consider the bare nitrogen adatoms have an intrinsic Auger sensitivity of 100%, the Auger sensitivities of the others are scaled down depending on the number of hydrogen atoms bonded to the central nitrogen and the relative alignment between the electron beam and the N-H bonds. For simplicity the Auger sensitivities of the adsorbed NH_3 and NH_2 are not distinguished from each other. The change in the number of hydrogen atoms and the change in the H-N-H bond angle act in opposition.

It becomes clear that the nitrogen AES signal can be dependent on the identities of the nitrogen-containing species on the sample surface.

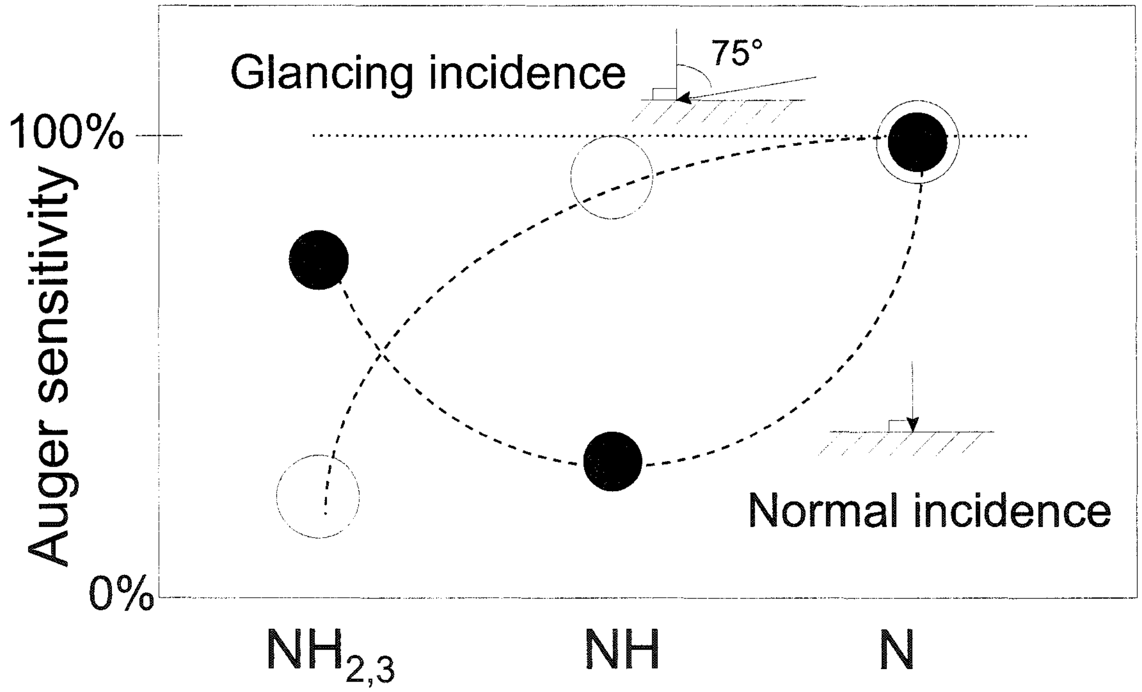

Figure 8-13 A schematic diagram of the Auger sensitivities of the adsorbed $NH_{2,3}$, NH and N with the primary electron beam at normal (●) or glancing incidence (O).

8.4.4 Past discussion of the AES shielding effect by heavy metal atoms

While the postulated shielding effect by N-H bonds is a key new finding in this thesis, there has been a heated discussion about a related AES shielding effect by heavy metals.

In 1990, Hubbard *et al.* presented their finding of measurements of the complete angular distribution of Auger electrons (65 eV) emitted from Pt(111) [Hubbard *et al.* 1990 (a) & (b)]. Their results revealed "*silhouettes of near-surface atoms back lit by Auger emissions originating from atoms deeper in the metal*". Auger signals were found to vary with the direction of emission from the surface. The findings supported their blocking model whereby platinum atoms in crystal behave as atomic point emitters for isotropic Auger electrons and also spherical atomic scatters of uniform cross sections.

Hubbard's model did not need other mechanisms such as anisotropic emission, diffraction, or multiple scattering to explain their measured results. The exclusion of these other mechanisms, however, was criticized by Egelhoff and other researchers [Egelhoff 1987, 1988 & 1990, Chambers 1990, Egelhoff *et al.* 1990, Wang *et al.* 1990, Woodruff 1990]. Their theoretical and experimental results suggested, on the contrary, the screening atoms behaved not as a blocker but as an electrostatic lens that focused the incident electrons on the underlying atoms. This enhanced the excitation probability of the atoms behind the screening atoms. Similarly the focussing effect of the screening atoms affected the angular dependence of the Auger electron emission from the atoms underneath.

The strength of forward scattering generally increases with atomic number of the scattering atom. While this electron scattering was proposed for platinum atoms, it is shown in this thesis that the effect is also detectable for hydrogen atoms. Hydrogen atoms might be thought to show a negligible effect, having such a low atomic number.

Auger electrons in this earlier discussion was 65 eV and rather low. In this thesis the emphasis is on shielding of the 2 keV incident primary electron beam. The postulation of the N-H bond shielding is novel and does not contradict any published results by other researchers.

8.4.5 Implication of the Auger sensitivity on the measured AES signal

The dependence of the nitrogen Auger sensitivity on the incident angle of the electron beam and the identity of the adsorbed species allows an explanation of the variation of the nitrogen AES signal ratio (figures 8-6 and 8-7).

It is understood that in the initial stage of an electron stimulated ammonia adsorption experiment the majority of the surface adsorbates will be NH_3 and NH_2. Referring to figure 8-13, the Auger sensitivity of $NH_{2,3}$ is low for the glancing incidence electron beam analysis and high for the normal incidence analysis, combining to give a low $\frac{\mathrm{G.I.(N)}}{\mathrm{N.I.(N)}}$ signal ratio. This explains the lowest $\frac{\mathrm{G.I.(N)}}{\mathrm{N.I.(N)}}$ ratio of ~1.3 at the very beginning of the electron stimulated ammonia adsorption experiments.

As the reaction proceeds, the electron stimulated degradation continues and $NH_{2,3}$ will be gradually replaced by NH. Figure 8-13 shows adsorbed NH can yield a high $\frac{\mathrm{G.I.(N)}}{\mathrm{N.I.(N)}}$ signal ratio. The Auger sensitivity is high with a glancing incidence electron beam and low for a normal incidence beam. The $\frac{\mathrm{G.I.(N)}}{\mathrm{N.I.(N)}}$ signal ratio increase to a maximum of about five at about 25 minutes of electron irradiation time can therefore be attributed to the stimulated degradation of $NH_{2/3}$ to NH. The adsorbed NH will be the dominant surface species when the $\frac{\mathrm{G.I.(N)}}{\mathrm{N.I.(N)}}$ signal ratio achieved its maximum value of about five. Note that for the adsorbed NH species the glancing incidence electron beam will give a larger signal because of the increased path length, back scattering and reduced hydrogen atom screening.

The last stage of the stimulated degradation of NH to N features a decrease of the $\frac{\text{G.I.(N)}}{\text{N.I.(N)}}$ signal ratio. The increase of the Auger sensitivity of NH to N with the normal incidence electron beam overwhelms the small rise with the glancing incidence electron beam, and thus the signal ratio drops. This analysis agrees with the data shown in figures 8-6 and 8-7. The $\frac{\text{G.I.(N)}}{\text{N.I.(N)}}$ signal ratio for the adsorption experiments on W(110) decreased after passing through its maximum at ~25 minutes of electron irradiation, becoming constant after 90 minutes. The final constant signal ratio of about 3.7 after 90 minutes corresponds to a surface essentially covered with nitrogen adatoms. There was no more dissociation and therefore no more change in the Auger sensitivities. Furthermore, since no attenuation from hydrogen is possible, we observe the conventional $(\cos \theta)^{-1}$ value.

This detailed and subtle dependence of the Auger sensitivity on the hydrogen content of the adsorbed species and angle of incidence of the electron beam explains the variation of the $\frac{\text{G.I. (N)}}{\text{N.I. (N)}}$ signal ratio throughout the stimulated ammonia adsorption experiments. No longer is it necessary to invoke different N-H bond dissociation probabilities for normal and glancing beams to explain an apparent 9.5× difference in the apparent initial adsorption rates, and yet achieve a saturated coverage after the same exposure time. It also complements the basic understanding of the enhanced Auger sensitivity with a glancing incidence electron beam by the *path factor*. This path factor explained the signal ratio of the bare nitrogen adatoms satisfactorily, but failed when the nitrogen atoms are still bonded with hydrogen atoms.

More significantly, the realization of the continuous electron stimulated degradation of adsorbed ammonia and the variation in the Auger sensitivities opened a window for a new adsorption mechanism that can account for the linear, coverage-independent rate of nitrogen signal increase. The separate activation - chemisorption site model applied in earlier chapters was aimed to facilitate a coverage-independent ammonia adsorption rate. The kinetic model requires a distinct ESA active site with uniqueness over the chemisorption site that could not be understood. There is now a new way to treat the coverage-independent nitrogen AES signal increase. An earlier assumption in chapter three which relates the size of nitrogen AES signal and the overall ammonia surface concentration is found no longer valid. It has been shown that different NH_X adsorbates (x = 0-3) make a different contribution to the overall nitrogen AES signal. The observed nitrogen AES signal is a subtle convolution of the concentration and composition of the adsorbed NH_X species.

8.5 CONCLUSION

The effects of the angle of incidence of the electron beam on electron stimulated ammonia adsorption and on the Auger analysis were investigated. A large variation of the $\frac{\text{G.I. (N)}}{\text{N.I. (N)}}$ signal ratio was observed during the adsorption experiments. The path factor that enhances the sensitivity of Auger analysis with a glancing incidence electron beam would have yielded a constant signal ratio. The possibility of ESA probabilities that depend on the incident angle of the electron beam was explored and found unlikely.

Auger sensitivity depends on the relative alignment of the incident electron beam and the N-H bonds of NH_X(ad) (*i.e.,* the angle of incidence of the primary beam and the molecular geometry of the NH_X adsorbate). It also depends on the number of hydrogen atoms bonded to the central nitrogen atom. The application of this screened nitrogen Auger sensitivity concept explained the variation of the $\frac{\text{G.I. (N)}}{\text{N.I. (N)}}$ signal ratio satisfactorily. The varying Auger sensitivity of the degrading NH_X adsorbates allows the relaxation of the assumption that equates the overall surface concentration of nitrogen-containing adsorbates to the overall nitrogen AES signal. That assumption had been the foundation of the ESA active site - chemisorption site model, which was difficult to defend.

The new adsorption model must only explain a linear, coverage-independent, nitrogen AES signal increase, rather than a more stringent condition of a coverage-independent rate of stimulated ammonia adsorption. This idea will be developed in the next chapter.

CHAPTER NINE

MODEL FOR ELECTRON STIMULATED AMMONIA ADSORPTION ON TUNGSTEN SINGLE CRYSTAL SURFACES

9.1 INTRODUCTION

The objective of this chapter is to determine a probable adsorption model for the electron stimulated ammonia adsorption on tungsten single crystal surfaces, based on the experimental results already described in the earlier chapters.

The rate of electron stimulated ammonia adsorption was shown to be directly proportional to the beam current, a first order relationship.

The dependence of the rate on the ammonia pressure revealed that the kinetics of the electron stimulated adsorption involved the participation of ammonia in ESA active sites which could become saturated. At room temperature, below the low 10^{-8} torr range the reaction order with respect to ammonia pressure was just over unity on W(100). This reflects a linear relationship between the "equilibrium" concentration of ammonia in ESA active sites and gas pressure at low pressure. The reaction order became zero at higher ammonia pressures on both crystal orientations. An "ESA active site - chemisorption site" model was proposed to rationalize the observed coverage-independence of the initial rate of change of the nitrogen AES signals.

The Arrhenius plots in the crystal temperature studies demonstrated the existence of two states of ammonia adsorbates: a physisorbed, hydrogen-bonded (to the NH_2 adlayer) precursor state ammonia and a nitrogen-bonded (to the substrate surface), chemisorbed state. The former was shown to have a binding energy of ~7 kJ mol^{-1}, irrespective to the crystal orientation, while the binding energy of the latter was found to be 120 kJ mol^{-1} on W(100). The energy value was thought to be dependent on the crystal orientation and could not be determined on W(110).

The observation of an induction period in the high crystal temperature, low ammonia gas pressure experiments led to the belief that the limiting factor in the adsorption kinetics is the availability of the ESA active sites which could increase in number with electron bombardments. This is in conflict with a key aspect of the "ESA active site – chemisorption site" model, which assumed a constant number of ESA active sites to explain the coverage-independent stimulated adsorption rates.

The experiments with varying angle of incidence of the electron beam demonstrated that the identities of the nitrogen containing adsorbate (NH_3, NH_2, NH and N) could affect the overall sizes of the resultant nitrogen AES signal. This invalidated an initial assumption that the magnitude of the nitrogen AES signal was a sufficient measure of the total surface concentration of all nitrogen-containing adsorbates. The hydrogen atoms, not directly detectable by AES, have been thought to have a negligible effect on the Auger analysis of nitrogen.

The analyses of the adsorption experiments with the normal and glancing incidence electron beams suggested the adsorption kinetics were not affected by the incidence angle of the electron beam. The observed variation on the nitrogen AES signal ratio between the two experiments was therefore only explained by the different Auger sensitivities of the degrading ammonia adsorbates. The Auger sensitivity was thought to be governed by the relative alignment between the N-H bonds on the ammonia adsorbate and the electron beam, in addition to the number of hydrogen atoms bonded to the nitrogen atoms.

This offered a new possible explanation for the surprising apparent coverage-independent rate of electron stimulated ammonia adsorption generally observed in the initial stage of the nitrogen AES signal evolution graphs under so many different experimental conditions. The original interpretation involved an adsorption mechanism which demanded a rate of adsorption insensitive to the change of the substrate surface composition. Now since the nitrogen Auger sensitivity depends on the surface NH_X composition, a general adsorption model with a rate sensitive to surface coverage is possible. The changing Auger sensitivities of the degrading ammonia species may be utilized to explain the initial linear nitrogen AES signal increase. This allows the stimulated adsorption rate to be coverage-dependent, presumably in a $(1-\theta)$ fashion. This relaxation eliminates the difficult task in the ESA active site - chemisorption site model of pinpointing the specific ESA active sites which are not also chemisorption sites. The Auger sensitivity was generally increasing as NH_3(ad) degraded to N(ad). The combined effect may, coincidentally, yield a linear response of the overall nitrogen AES signals.

In this chapter, the idea of quantified Auger sensitivity factors and a more conventional coverage-dependent adsorption mechanism are integrated to explain the important experimental results reported in the earlier chapters. This approach circumvented the weaknesses in the former adsorption model (the ESA active site – chemisorption site model), in particular our inability to identify the small concentration of ESA active sites as distinct from the other surface sites on the single crystal surfaces.

9.2 DATA SIMULATION

The reliability of any adsorption model depends on how well its simulated data agree with the experimental results. The data simulation should satisfactorily reproduce all the important features of the experimental data. In the experiments of electron stimulated ammonia adsorption on W(100) and W(110), the most surprising feature of the results was the coverage-independent growth of the nitrogen AES signal. The linearity of the signal increase could extend to 70% of the final saturation level.

Before attempting a replication of nitrogen AES signal evolution graph, the general expression for the data simulation has to be established. The general idea was developed in chapter eight to produce simulated data by relating the different Auger sensitivities and the surface concentrations of the decomposing ammonia adsorbates.

The magnitude of the nitrogen AES signal is primarily decided by two factors: the Auger sensitivity factor ($\alpha^{i}{}_{\mathrm{NH_X}}$), which will depend on the incidence angle of the electron beam, *i*, and the surface coverage of each NH_X adsorbate ($\theta_{\mathrm{NH_X}}$).

$$\text{Nitrogen AES signal at time } t = \sum_{x=0}^{3}\left(\alpha^{i}{}_{\mathrm{NH_X}} \cdot \theta_{\mathrm{NH_X}}\right) \ \ldots \ (9\text{-}1)$$

These two factors and their generation are discussed in the following sub-sections.

In equation 9-1 each product term gives the contribution to the nitrogen AES signal by the NH_X adsorbate. The summation gives the total nitrogen AES signal from N, NH, NH_2 and NH_3. This expression assumes every nitrogen-containing species is adsorbed on the topmost layer.

9.2.1 The Auger sensitivity factors

The origin of the Auger sensitivity factors has been discussed in the previous chapter. Quantitatively expressing these Auger sensitivity factors is necessary for the data simulation of the nitrogen AES signals. The numerical values of the $\alpha^{i}{}_{\mathrm{NH_x}}$ values can only be estimated with two boundary conditions of better known surface coverages. One is the surface composition at the beginning of the stimulated adsorption experiment, of which the nitrogen AES signal was determined at time zero in a nitrogen AES signal evolution graph. This surface was composed of primarily ground state chemisorbed NH_2 and physisorbed, un-dissociated NH_3. The other one is the surface composition at the end of the stimulated adsorption experiment. This surface was adsorbed with a maximum coverage of nitrogen atoms, with all three bonded hydrogen atoms stripped away via the continuous electron stimulated dissociation.

An example using the W(100) stimulated adsorption experiment at room temperature with a normal incidence electron beam is given here for demonstrative purposes. For the first boundary condition, the size of the nitrogen AES signals at zero electron beam time (~1260 arb. units) can be identified with a half monolayer surface coverage as observed in the ground state adsorption experiments after an extended period (section 3.3). The saturated, full monolayer, nitrogen covered surface at the end of the adsorption experiment produced a nitrogen AES signal of ~4000 arb. units, representing the second boundary condition (section 4.3). For an angle of incidence *i*,

$$\text{For } t = 0, \qquad N_0^{\mathrm{AES}} = \sum_{x=0}^{3}\left(\alpha^{i}{}_{\mathrm{NH_x}}\cdot\theta_{\mathrm{NH_x}}\right) = \alpha^{i}{}_{\mathrm{NH_{2,3}}}\cdot\theta_{\mathrm{NH_{2,3}}} = \alpha^{i}{}_{\mathrm{NH_{2,3}}}\cdot 0.5$$

$$\text{For } t = \infty, \qquad N_\infty^{\mathrm{AES}} = \sum_{x=0}^{3}\left(\alpha^{i}{}_{\mathrm{NH_x}}\cdot\theta_{\mathrm{NH_x}}\right) = \alpha^{i}{}_{\mathrm{N}}\cdot\theta_{\mathrm{N}} = \alpha^{i}{}_{\mathrm{N}}\cdot 1.0$$

For normal incidence, $i = n$,

$$N_0^{AES} = 1260 = \alpha^n{}_{NH_{2,3}} \cdot 0.5\,; \qquad \alpha^n{}_{NH_{2,3}} = 2520$$

$$N_\infty^{AES} = 4000 = \alpha^n{}_N \cdot 1.0\,; \qquad \alpha^n{}_N = 4000$$

$$\therefore\ \alpha^n{}_{NH_{2,3}} = 0.63 \cdot \alpha^n{}_N \quad [100]$$

reflecting the attenuation of the nitrogen AES signal by hydrogen.

For glancing incidence, $i = g$,

$$N_0^{AES} = 1380 = \alpha^g{}_{NH_{2,3}} \cdot 0.5\,; \qquad \alpha^g{}_{NH_{2,3}} = 2760$$

$$N_\infty^{AES} = 12800 = \alpha^g{}_N \cdot 1.0\,; \qquad \alpha^g{}_N = 12800$$

$$\therefore\ \alpha^g{}_{NH_{2,3}} = 0.22 \cdot \alpha^g{}_N \quad [100]$$

reflecting a much greater attenuation by hydrogen for the glancing incidence beam.

For W(110) single crystal surfaces the magnitudes of the Auger sensitivity factors $\alpha^i{}_{NH_{2,3}}$ relative to $\alpha^i{}_N$, can be determined in the same way.

For normal incidence,

$$N_0^{AES} = 1040 = \alpha^g{}_{NH_{2,3}} \cdot 0.5\,; \qquad \alpha^n{}_{NH_{2,3}} = 2080$$

$$N_\infty^{AES} = 3630 = \alpha^n{}_N \cdot 1.0\,; \qquad \alpha^n{}_N = 3630$$

$$\therefore\ \alpha^n{}_{NH_{2,3}} = 0.57 \cdot \alpha^n{}_N \quad [110]$$

For glancing incidence,

$$N_0^{AES} = 780 = \alpha^g{}_{NH_{2,3}} \cdot 0.5\,; \qquad \alpha^g{}_{NH_{2,3}} = 1560$$

$$N_\infty^{AES} = 12880 = \alpha^g{}_N \cdot 1.0\,; \qquad \alpha^g{}_N = 12880$$

$$\therefore\ \alpha^g{}_{NH_{2,3}} = 0.12 \cdot \alpha^g{}_N \quad [110]$$

The greater attenuation for $NH_{2,3}$ on the (110) surface may reflect specific differences in geometry of the adsorbates on this surface.

The precision of these projected Auger sensitivity values were limited by the uncertainty of the measured nitrogen AES signals, and the assumptions of the designated half- or full monolayer coverages of ammonia. A deviation of ± 5% on top of the calculated values should be contemplated. The reliability of the smaller values of the $\alpha^{g}{}_{NH2,3}$ for W(100) and W(110) was therefore more severely affected.

The Auger sensitivity factor for NH(ad), $\alpha^{i}{}_{NH}$, cannot be determined by the boundary conditions. It is not believed there is a moment during the stimulated adsorption process when the sample surface is covered with only NH and no other nitrogen-containing adsorbates. However, following the hydrogen-shielding effect argument developed in the last chapter the magnitudes of $\alpha^{i}{}_{NH}$ can be estimated. In the experiments with the normal incidence electron beam the $\alpha^{n}{}_{NH}$ value would be even lower than the $\alpha^{n}{}_{NH2,3}$ value because of the head-on shielding effect by the lone on-top hydrogen atom. On the other hand, when the electron beam is at 75°-off surface normal (glancing incidence), this lone on-top hydrogen atom would be out of the way of the electron beam and provides little shielding to the nitrogen atom underneath from being bombarded with the electrons. Therefore the Auger sensitivity factor $\alpha^{g}{}_{NH}$ value would be high, comparable to the $\alpha^{g}{}_{N}$ value. The magnitudes of $\alpha^{i}{}_{NH}$ will be adjustable parameters in the simulation models.

9.2.2 Surface concentration of each NH_X

The second component in the generation of the nitrogen AES signal in equation 9-1 is the surface concentration of each of the dissociating ammonia adsorbates: θ_N, θ_{NH}, $\theta_{NH2,3}$. Once these time-dependent concentration values are determined, the nitrogen AES signal at any time *t* can be expressed. The changes of the surface concentration of each species, however, must follow this general reaction scheme:

$$\mathrm{NH_3} + * \rightleftharpoons \underset{*}{\mathrm{N}}\mathrm{H_3} \qquad K \qquad \ldots (9\text{-}2)$$

$$\underset{*}{\mathrm{N}}\mathrm{H_3} \xrightarrow{e} \underset{*}{\mathrm{N}}\mathrm{H_2} + \mathrm{H} \qquad k_1 \qquad \ldots (9\text{-}3)$$

$$\underset{*}{\mathrm{N}}\mathrm{H_2} + \mathrm{H} \xrightarrow{e} \underset{*}{\mathrm{N}}\mathrm{H} + \mathrm{H} \qquad k_2 \qquad \ldots (9\text{-}4)$$

$$\underset{*}{\mathrm{N}}\mathrm{H} + \mathrm{H} \xrightarrow{e} \underset{*}{\mathrm{N}} + \mathrm{H} \qquad k_3 \qquad \ldots (9\text{-}5)$$

Gas phase ammonia molecules are reversibly adsorbed onto the tungsten crystal surface on the ESA active sites. The weakly adsorbed molecules were stimulated by electron irradiation and those on available vacant sites dissociated into $\mathrm{NH_2}$ and H fragments. Continuous electron stimulation dissociated the adsorbed $\mathrm{NH_2}$ fragments into NH and then N on the crystal surface, each time losing a hydrogen atom.

In our stimulated adsorption experiments AES was the only experimental technique that measured atomic surface composition. AES, however, did not allow the individual surface concentration measurement of each $\mathrm{NH_X}$ species when they were on the sample surface simultaneously. Therefore the individual surface coverage of the dissociating ammonia adsorbates at any time *t* can only be simulated, derived from a plausible adsorption mechanism that achieved the dissociative adsorption in the fashion shown in equations 9-2 to 9-5.

This adsorption mechanism must yield data for the surface coverages agreeing with the boundary conditions (half-monolayer of $\mathrm{NH_{2,3}}$ at the beginning and one full monolayer of N at the end). In addition, when optimized with the three Auger sensitivity factors of the involved adsorbates, the simulated nitrogen AES signals should demonstrate the observed constant increase with electron irradiation time. A coverage-independent rate of AES signal increase, up to 70% of the saturation level, was observed experimentally.

9.3 REALISTIC SITE EXCLUSION SIMULATION METHOD

We adopt a realistic model to simulate the evolution of the surface coverage of the nitrogen-containing adsorbate. The scheme is simple: initially the sample surface is made up of a NH_2 half-covered, well-ordered surface, with every other surface site left unoccupied. Unpaired, these vacant surface sites cannot dissociatively adsorb ammonia. Due to the difference in the dimension of the surface lattice parameter (3.16 Å for tungsten) and the van der Waals diameter of ammonia (3.8 Å) [Matsushita and Hansen 1970, Peng and Dawson 1971, Lide 2003], the surrounded vacant sites are sterically hindered in accommodating new ammonia molecules. In this discussion the vacant sites being hindered for adsorption is referred to as site exclusion. Upon electron irradiation, the adsorbed NH_2 dissociate into less bulky NH(ad), and eventually N(ad). This removal of hydrogen atoms reduces the van der Waals size of the adsorbates. The vacant sites, which were sterically hindered by the bulky neighbours before electron irradiation, are now relieved from the burden and open to accommodate new ammonia molecules. The electron stimulated dissociation of the NH_2(ad) lifts the site exclusion. When ammonia molecules are allowed on the relaxed vacant sites, electron stimulated adsorption proceeds.

In this simulation scheme, we describe the site exclusion by the physical size of the adsorbates in a two dimensional picture.

9.3.1 Signal generation

On a hypothetical array of 14 × 14 surface sites (for a total of 196 sites) mimicking half-covered W (100), a NH_2 adsorbate was assigned onto every other site (figure 9-1). This resulted in an ideal C(2×2) surface ordering with an exact half monolayer coverage of ammonia. The other half of the surface sites was

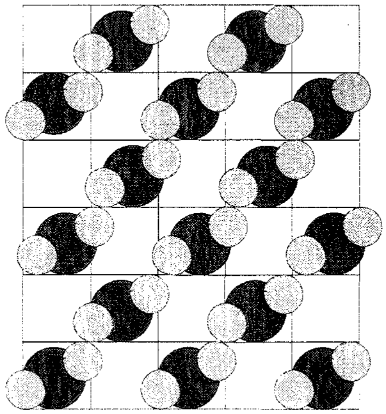

Figure 9-1
A portion of a W(100) surface half-filled with NH_2.

unoccupied. There were no adjacent pairs of vacant tungsten atoms were available to form a four-member transition state (see figure 1-2 on page 4) for ground state ammonia adsorption [Estrup and Anderson 1967 (b)]. Furthermore, in the model to be developed it will be assumed that NH_2 must dissociate by electron bombardment to the less bulky NH to permit NH_3 adsorption on an adjacent isolated vacant site.

Random coordinates were generated to mimic the position of the surface site where an incoming electron interacts with the sample surface. Should the coordinates match a NH_2 occupied surface site, this NH_2(ad) was dissociated via electron stimulation into a less voluminous NH (ad). The four neighbouring vacant sites then became accessible for new ammonia adsorption (figure 9-2). At 300 K and a high 1×10^{-7} torr gas pressure, the reaction order of ESA with respect to the gas pressure was zero on both crystal orientations. The rate limiting factor was therefore the availability of the vacant surface sites. As soon as a vacant surface site is released, it would be occupied with an ammonia precursor molecule. The edge effect of this finite array was taken care of by carrying the relaxation of steric hindrance due to any electron stimulated dissociation of bulky NH_2 at the side of the array across to the vacant site on the opposite side of the array.

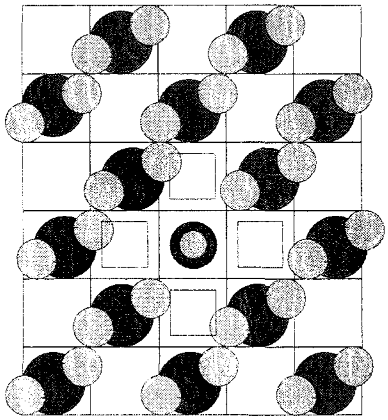

Figure 9-2
The same array with one NH_2 dissociated to NH and the four neighbour sites (double squares) became available for NH_3 adsorption.

There would be no effect when the random coordinates generate an electron bombardment on a vacant surface site, as nothing was available to be stimulated. Should a NH(ad) be electron bombarded, it could undergo a second stimulated dissociation into N and H. Further electron bombardment on a bare nitrogen adatom would not yield any effect. Electron stimulated desorption of any nitrogen-containing species was not considered. The dissociated hydrogen atoms were not considered to place any demand by site occupation, either by electron stimulated desorption or by adsorption between the nitrogen adsorption sites.

9.3.2 Results of data simulation with equal dissociation rate constants

In this data simulation method, the relative values of the rate constants of reactions 9-3 to 9-5 (k_1, k_2 and k_3) were adjusted by the necessary number of electron bombardments to trigger a successful electron stimulated dissociation. In the simplest case when $k_1 = k_2 = k_3$ every simulated electron bombardment at an adsorbed NH_X (x = 1-3) would lead to dissociation. In addition, electron bombardment of ground state adsorbed NH_2 led to further ammonia adsorption onto all its vacant neighbouring sites.

The changes in the surface coverages of $NH_{2,3}$, NH and N simulated assuming rate constants $k_1 = k_2 = k_3$ and every electron collision was effective in dissociation are shown in figure 9-3.

Since it was assumed the crystal surface was half-covered with ground state adsorbed ammonia before electron stimulation, $\theta_{NH_{2,3}}$ started at 0.5 ML at zero electron count. This high initial surface concentration of reactants induced a rapid electronstimulated dissociation of NH_2(ad). The rapid and massive relaxation of steric hindrance made an abundant number of vacant sites become available for new NH_3 physisorption and subsequent electron stimulated adsorption. This explained the sharp increase of $\theta_{NH_{2,3}}$ from 0.5 ML to ~0.73 ML in fewer than 80 electron impacts on the array (~4×10^{14} electron bombardments over 1 cm^2 of the crystal surface).

The fractional coverage simulation was mapped onto the normal and glancing incidence AES electron beam adsorption data on W(100) surface reported in chapter eight. In those two experiments the nitrogen AES signals reached the saturation level in approximately 60 minutes. Thus a conversion factor was employed to mimic a result of about two effective electron bombardments per minute on this 14 × 14 sites array (~10^{13} bombardments cm^{-2} min^{-1}). Using the pre-determined values of $\alpha^i_{NH_{2,3}}$ and α^i_N ,

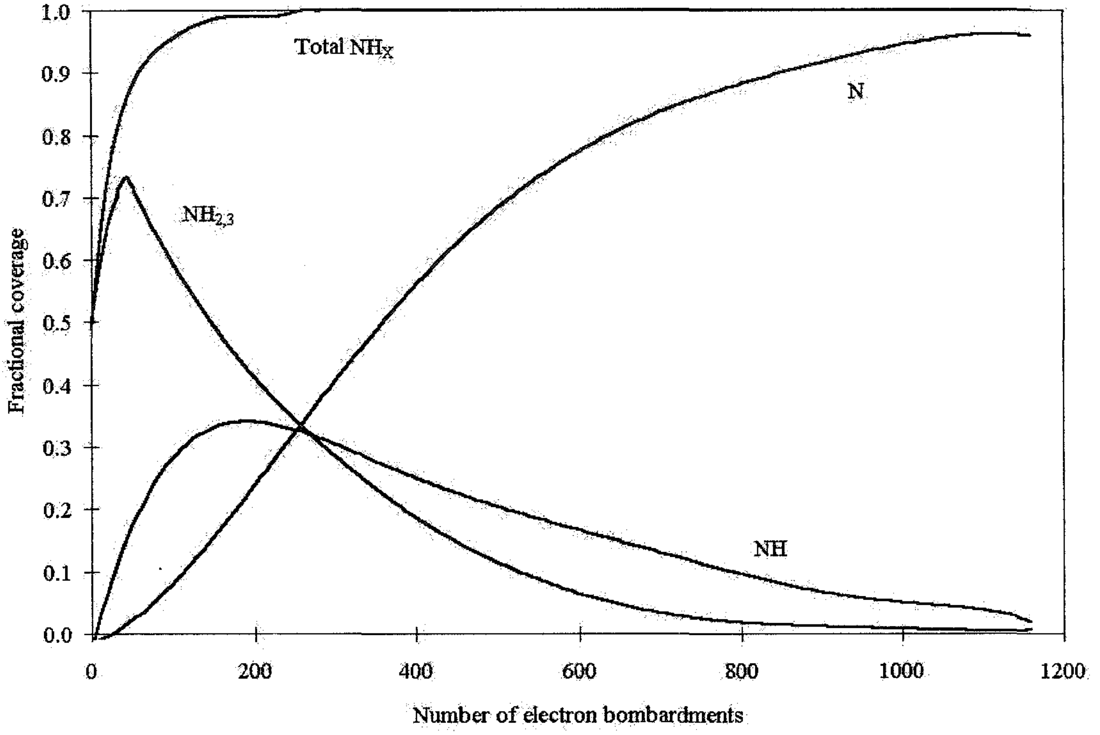

Figure 9-3 Site-filling simulation results of the fraction coverage of NH_X with $k_1 = k_2 = k_3$.

the value of α^i_{NH} were optimized to produce the best fit data set of simulated nitrogen AES signal generated by equation 9-1. The simulated and the experimental nitrogen AES signals are shown together in figures 9-4 (for normal incidence electron beam results) and 9-5 (for glancing incidence electron beam results). The values of the Auger sensitivity factors substituted into equation 9-1 are shown in Table 9-1.

	$\alpha^i_{NH2,3}$	α^i_{NH}	α^i_{N}
Normal incidence ($i = n$)	63 %	40 %	100 %
Glancing incidence ($i = g$)	18 %	75 %	100.00%

Table 9-1 The values of the Auger sensitivity factors involved in the simulation of the nitrogen AES signals in the stimulated adsorption experiments on W(100).

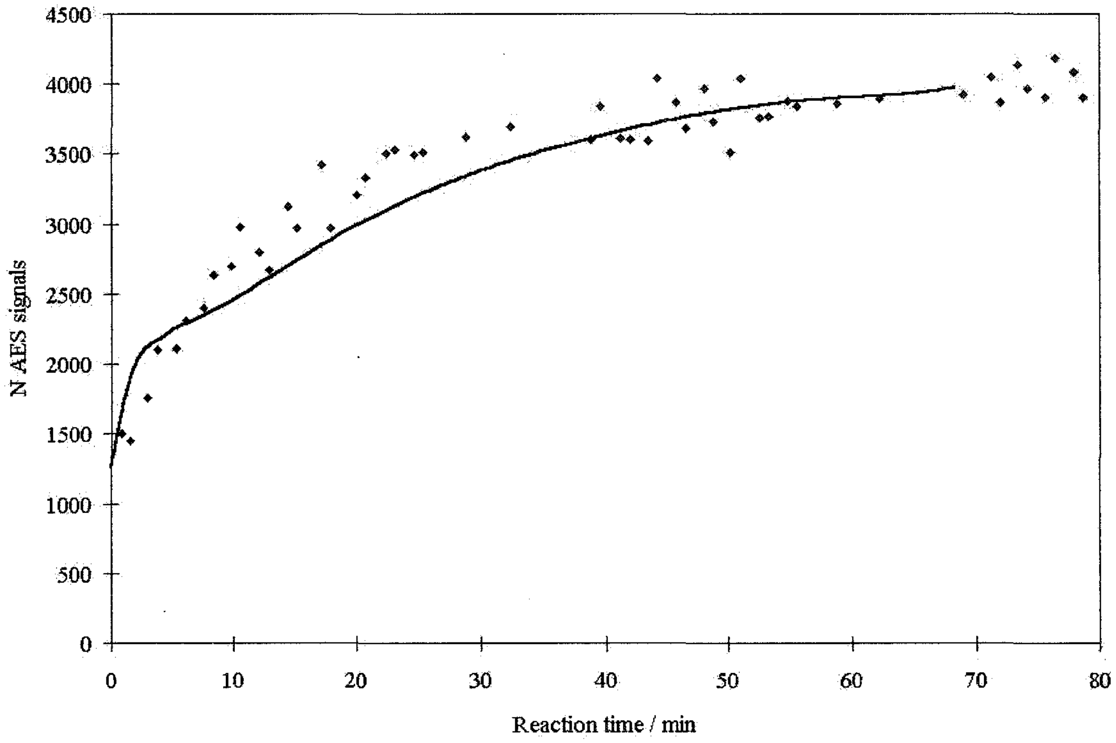

Figure 9-4 The comparison between the simulated nitrogen AES signals and the experimental AES signals of the electron stimulated NH_3 adsorption on W(100), 5×10^{-7} torr NH_3, 300 K, normal incidence electron beam.

Rate constants $k_1 = k_2 = k_3$.

Simulation parameters: $\alpha^{n}{}_{NH2,3}$ 63%, $\alpha^{n}{}_{NH}$ 40% and $\alpha^{n}{}_{N}$ 100%.

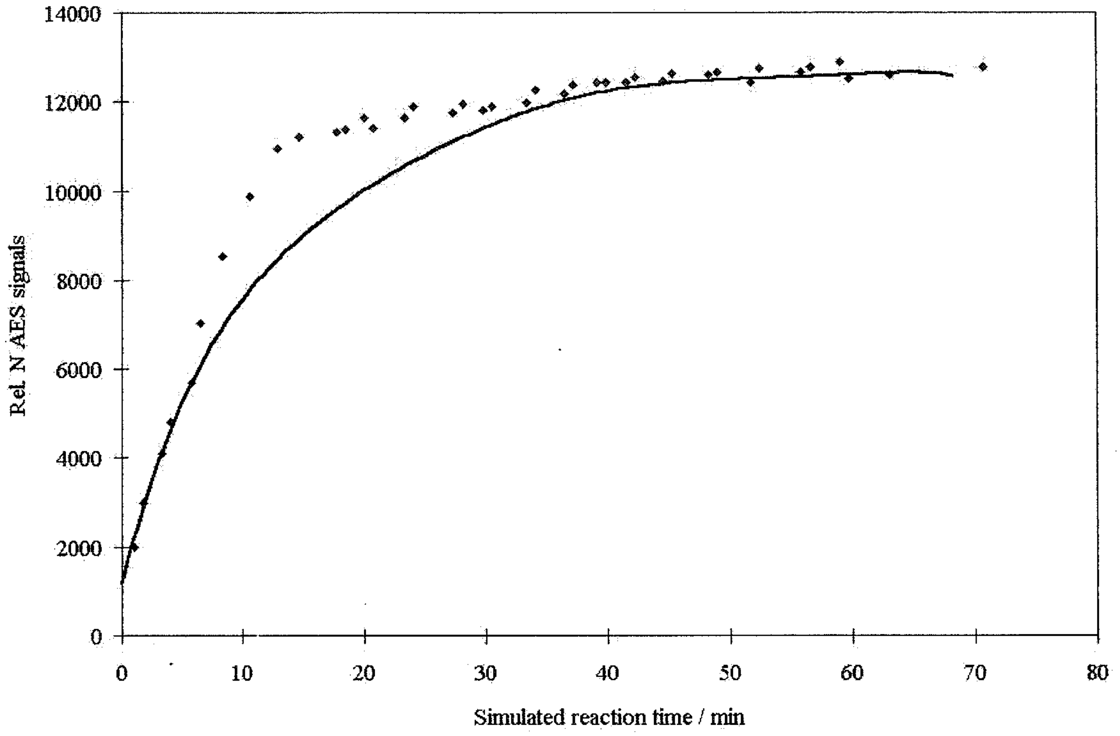

Figure 9-5 The comparison between the simulated nitrogen AES signals and the experimental AES signals of the electron stimulated NH_3 adsorption on W(100), 5×10^{-7} torr NH_3, 300 K, glancing incidence electron beam.

Rate constants $k_1 = k_2 = k_3$.

Simulation parameters: $\alpha^g{}_{NH2,3}$ 18%, $\alpha^g{}_{NH}$ 95% and $\alpha^g{}_N$ 100%.

The fit is not satisfactory. In the graph of the normal incidence electron beam experiments (figure 9-4), there was a bump in the simulated data series at the very beginning (about the first five minutes of electron irradiation time), displaying AES signals much higher than the experimental values. Only by decreasing the value of $\alpha^{n}{}_{\mathrm{NH}2,3}$ from a pre-calculated 63% to 50% would give a fit for the first three data points, yet the simulation would not even fit the experimental time zero value. Besides, the decrease was far more than the 5% uncertainty. The fitting in this initial stage did not get any better no matter how the $\alpha^{n}{}_{\mathrm{NH}}$ value was varied from 0 to 100%. The fitting was no better after this initial stage.

On the other hand, the simulation data agreed well with the experimental data in the glancing incidence beam experiments at the very beginning. In figure 9-5 it was seen in about the first six minutes of electron irradiation time, the simulated and the experimental data matched each other better than they did in the normal incidence beam experiments (figure 9-4). However, that was the only advantage of this simulation. The six minutes of constant rate of nitrogen AES signal increase was over 50% shorter than the fourteen minutes duration exhibited by the experimental data. The simulated signals were significantly weaker than the experimental signals in the period between the 6th and 30th minute. The difference was greatest at about the 14th minute, when the experimental AES signals stopped the linear increase. The difference became smaller after this moment. After the 30th minute mark the difference between the simulated and the experimental signals shrank to only a few per cent.

The data simulation for the stimulated adsorption experiments on W(110) was similarly performed. The comparison between the experimental data and the simulated data of the adsorption experiments with the normal incidence electron beam is shown in figure 9-6, and that with the glancing incidence electron beam can be seen in figure 9-7. The values of the Auger sensitivity factors used in the data simulation for the stimulated adsorption experiments on W(110) are found in table 9-2.

	$\alpha^{i}_{NH2,3}$	α^{i}_{NH}	α^{i}_{N}
Normal incidence ($i = n$)	43 %	20 %	100 %
Glancing incidence ($i = g$)	9 %	70 %	100 %

Table 9-2 The values of the Auger sensitivity factors involved in the simulation of the nitrogen AES signals in the stimulated adsorption experiments on W(110).

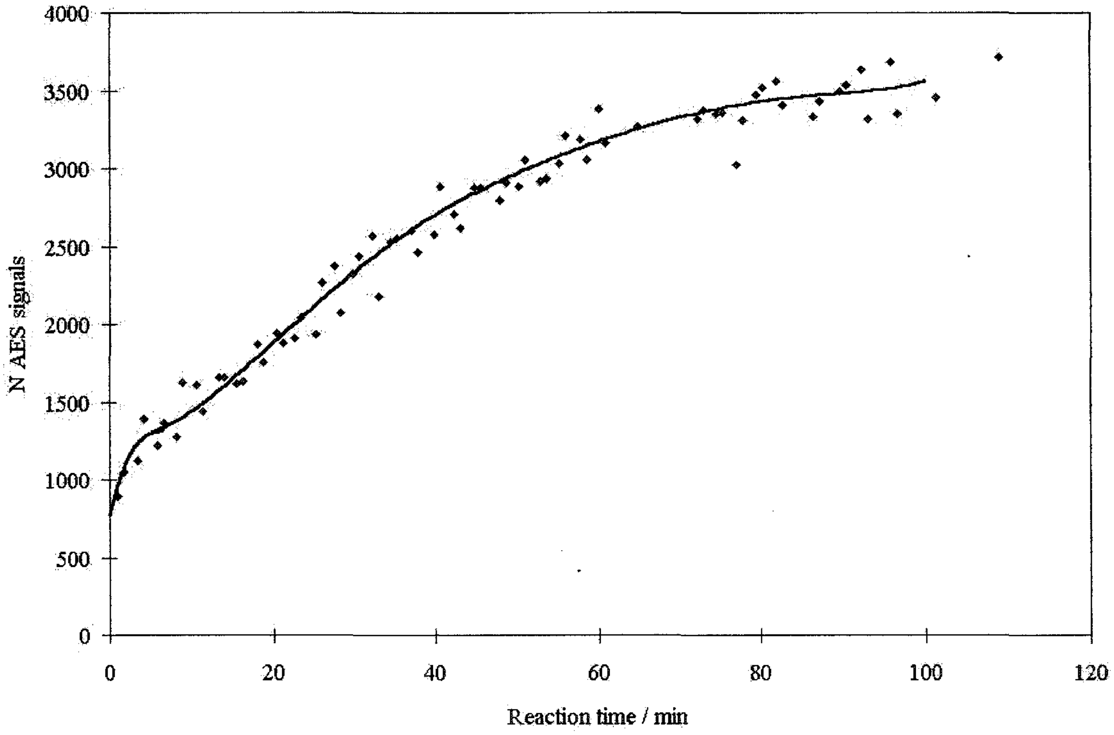

Figure 9-6 The comparison between the simulated nitrogen AES signals and the experimental AES signals of the electron stimulated NH_3 adsorption on W(110), 5×10^{-7} torr NH_3, 300 K, normal incidence electron beam.

Rate constants $k_1 = k_2 = k_3$.

Simulation parameters: $\alpha^{n}_{NH2,3}$ 43%, α^{n}_{NH} 20% and α^{n}_{N} 100%.

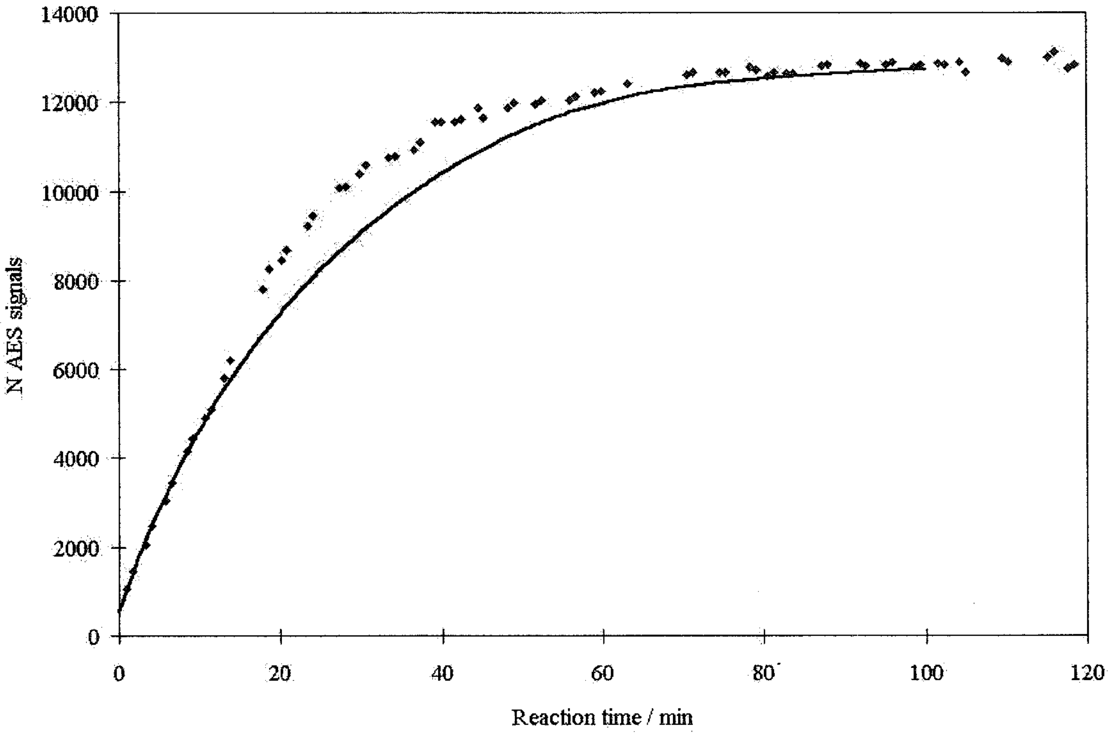

Figure 9-7 The comparison between the simulated nitrogen AES signals and the experimental AES signals of the electron stimulated NH_3 adsorption on W(110), 5×10^{-7} torr NH_3, 300 K, glancing incidence electron beam.

Rate constants $k_1 = k_2 = k_3$.

Simulation parameters: $\alpha^g{}_{NH2,3}$ 9%, $\alpha^g{}_{NH}$ 70% and $\alpha^g{}_N$ 100%.

For the electron stimulated ammonia adsorption on W(110), the agreement between the simulated and the experimental data was not as bad as in the W(100) case. In the normal incidence electron beam experiments, the data fitting was generally satisfactory (figure 9-6). There is still a bump in the simulated data at the very beginning of the AES signal evolution profile, as was the case for the W(100) experiments. The size was smaller and it matched better with the contour of the experimental data than it did in the W(100) case.

The fitting for the glancing incidence electron beam experiment results still had room for improvement (figure 9-7). The data fitting was good up to the level of 40% of relative nitrogen AES signals (~14 minutes), approximately the same as in the W(100) fitting. Afterward the simulated signals could not match the rapid and linear increase of the experimental signals. Every finding suggested there were problems in the methodology of the AES signal simulation.

9.3.3 Results of data simulation with adjusted dissociation rate constants

The relative values of the rate constants k_1, k_2 and k_3 were adjusted in order to achieve a better simulation. In the normal incidence beam experiments, the simulated signals were too strong at the beginning. Since the dominant species on the crystal surface during the initial stage was $NH_{2,3}$(ad), an attempt was made to decrease its surface concentration. The rate constant k_2 was increased to boost the NH_2 dissociation into NH. The condition of the rate constants was set as $k_1 = k_2 = 2 \times k_3$. Effectively, in the simulation process, it took one electron bombardment to dissociate NH_2 into NH, while it took two bombardments to dissociate NH into N. The rate of stimulated NH_2 dissociation was then twice as fast as that of NH dissociation. A simple justification might be that when the species contains twice as many N-H bonds the probability of a dissociation event is doubled. The change of surface coverages of the NH_X(ad) is shown in figure 9-8.

The initial increase of the $\theta_{NH2,3}$ was smaller (0.5 → 0.64 ML) when compared to that in figure 9-3 (0.5 → 0.73 ML). On the other hand, θ_{NH} increased to a larger extent (0.58 ML) than in figure 9-3 (0.35 ML). Both desired effects were achieved with the adjustments made on the relative values of the rate constants. The doubled rate constants k_1 and k_2 over k_3 resulted in a strong accumulation of NH(ad) and a quick depletion of $NH_{2,3}$(ad). This would help reduce the initial sharp increase of the simulated signal in the normal incidence beam adsorption experiments. The values of the Auger sensitivity factors $\alpha^n{}_{NH2,3}$ were greater than $\alpha^n{}_{NH}$ on both crystal surfaces. The faster reduction of $NH_{2,3}$ could drive the overall nitrogen AES signals smaller and reduce the size of that early spurt in the data simulation.

The comparisons between the experimental data and the simulated data (by this $k_1 = k_2 = 2 \times k_3$ approach) for the stimulated adsorption experiments on W(100) are displayed in figure 9-9 (normal incidence beam) and 9-10 (glancing incidence beam). Those for W(110) are shown in figure 9-11 (normal incidence beam) and 9-12 (glancing incidence beam).

The values of the corresponding Auger sensitivity factors in this scheme of data simulation are collected in table 9-3.

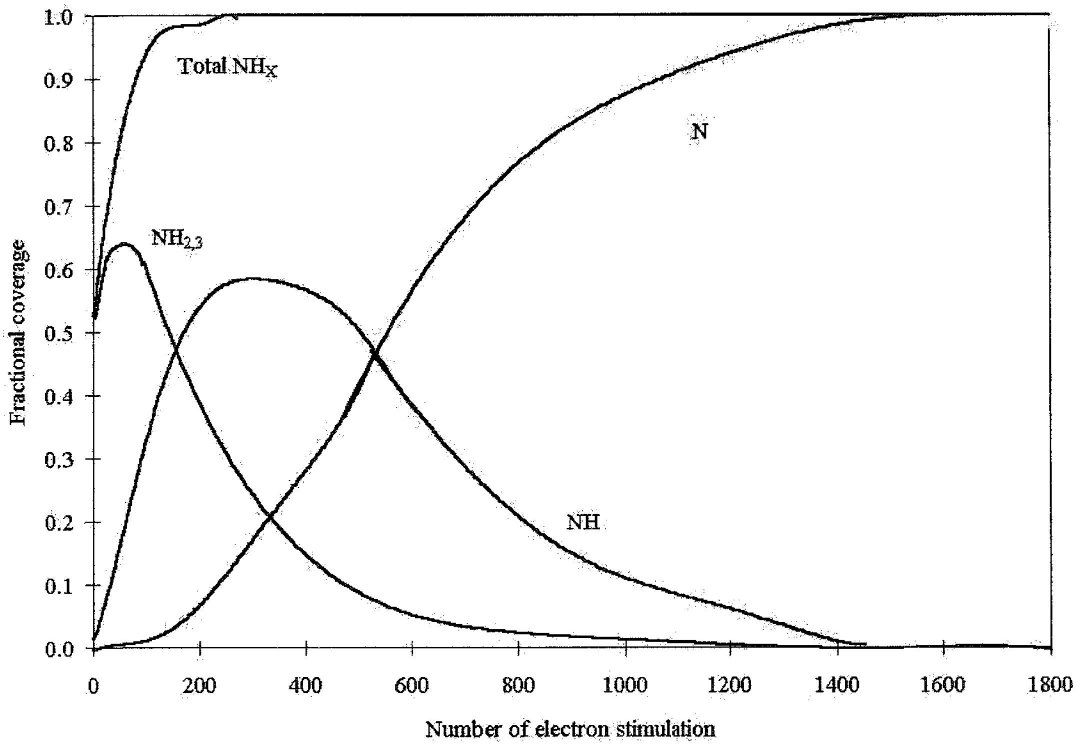

Figure 9-8 Site-filling simulation results of the fraction coverage of NH_X with $k_1 = k_2 = 2\ k_3$.

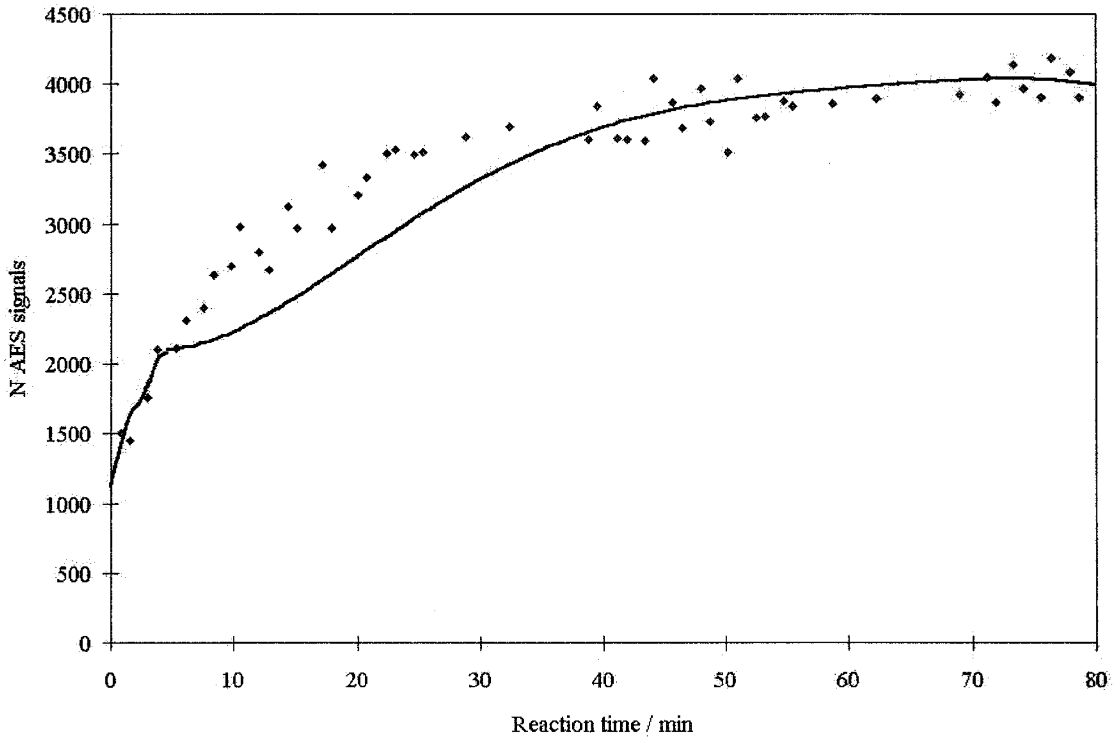

Figure 9-9 The comparison between the simulated nitrogen AES signals and the experimental AES signals of the electron stimulated NH_3 adsorption on W(100), 5×10^{-7} torr NH_3, 300 K, normal incidence electron beam.

Rate constants $k_1 = k_2 = 2 \times k_3$.

Simulation parameters: $\alpha^{n}{}_{NH2,3}$ 55%, $\alpha^{n}{}_{NH}$ 50% and $\alpha^{n}{}_{N}$ 100%.

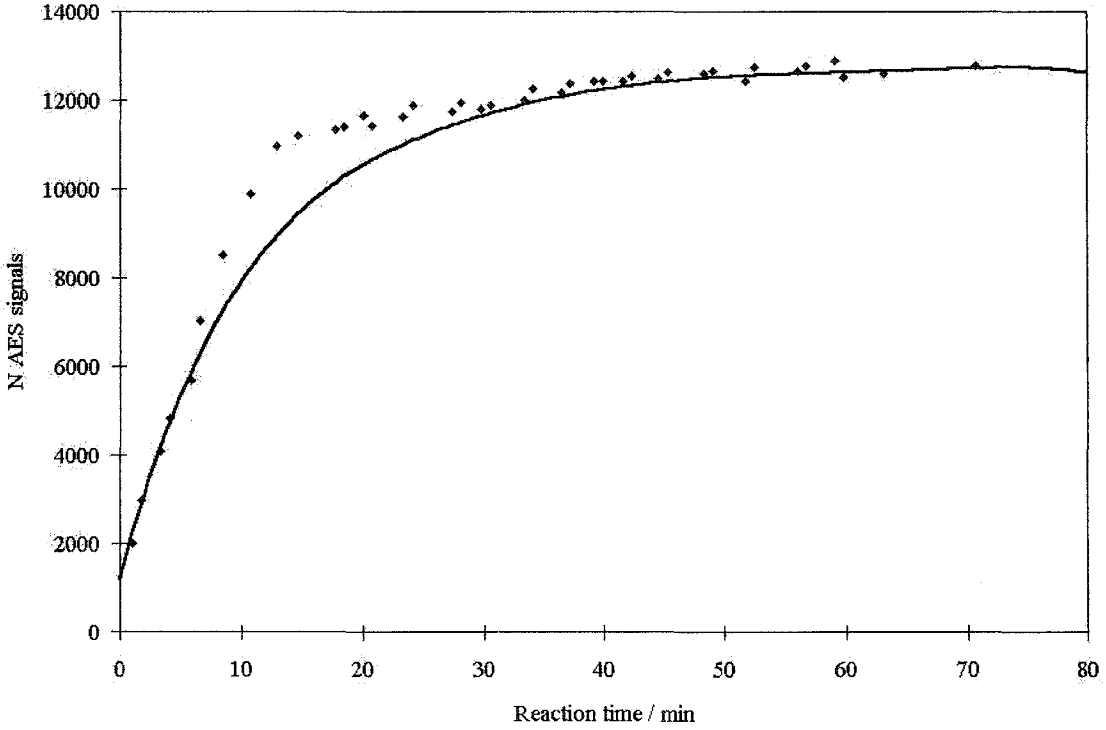

Figure 9-10 The comparison between the simulated nitrogen AES signals and the experimental AES signals of the electron stimulated NH_3 adsorption on W(100), 5×10^{-7} torr NH_3, 300 K, glancing incidence electron beam.

Rate constants $k_1 = k_2 = 2 \times k_3$.

Simulation parameters: $\alpha^{g}_{NH2,3}$ 18%, α^{g}_{NH} 85% and α^{g}_{N} 100%.

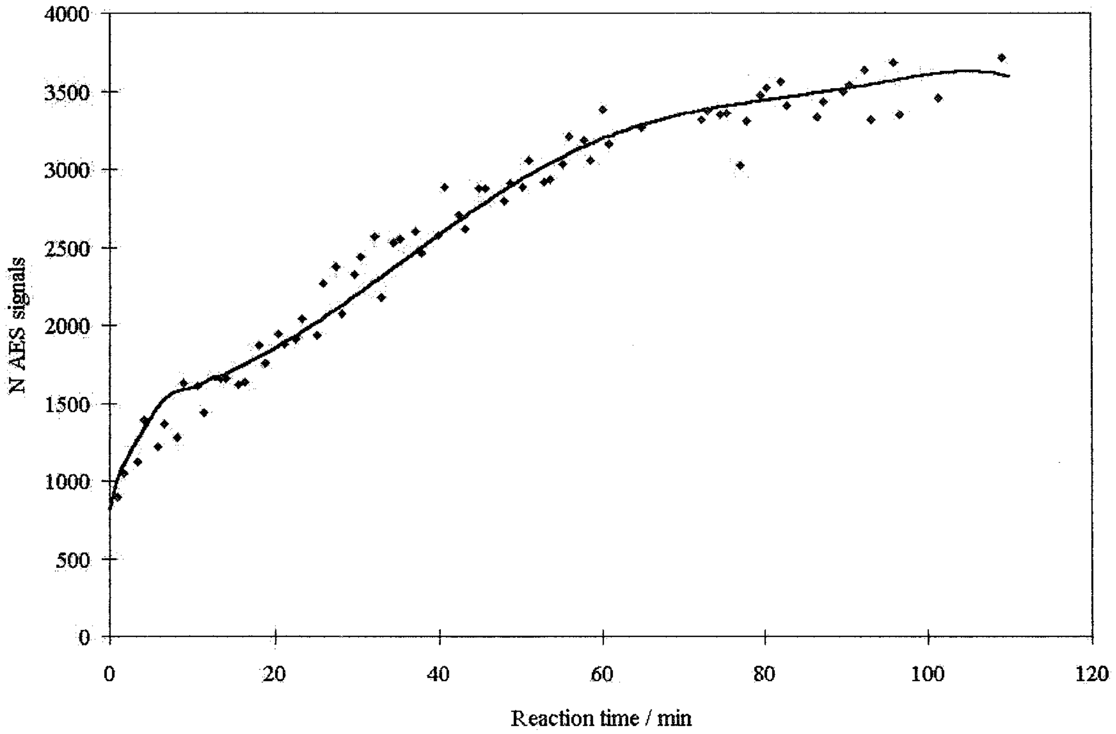

Figure 9-11 The comparison between the simulated nitrogen AES signals and the experimental AES signals of the electron stimulated NH_3 adsorption on W(110), 5×10^{-7} torr NH_3, 300 K, normal incidence electron beam.

Rate constants $k_1 = k_2 = 2 \times k_3$.

Simulation parameters: $\alpha^n{}_{NH2,3}$ 45%, $\alpha^n{}_{NH}$ 42.5% and $\alpha^n{}_{N}$ 100%.

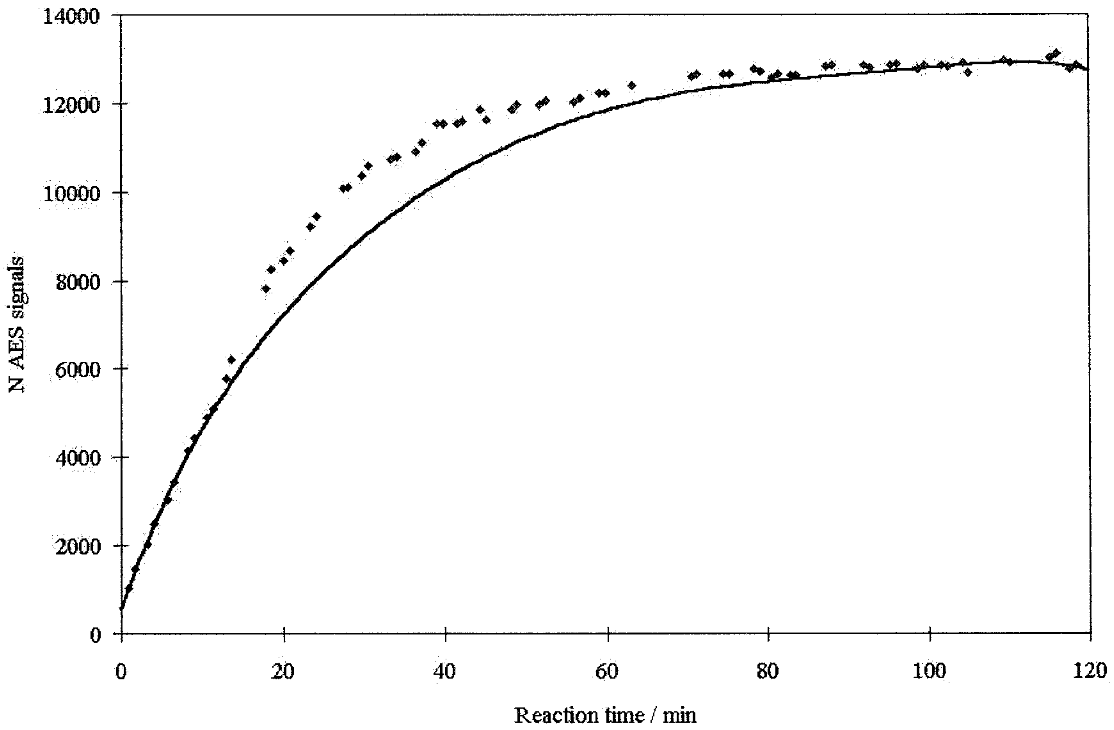

Figure 9-12 The comparison between the simulated nitrogen AES signals and the experimental AES signals of the electron stimulated NH_3 adsorption on W(110), 5×10^{-7} torr NH_3, 300 K, glancing incidence electron beam.

Rate constants $k_1 = k_2 = 2\times k_3$.

Simulation parameters: $\alpha^g{}_{NH2,3}$ 9%, $\alpha^g{}_{NH}$ 67.5% and $\alpha^g{}_{N}$ 100%.

		$\alpha^{i}_{NH2,3}$	α^{i}_{NH}	α^{i}_{N}
W(100)	Normal incidence ($i = n$)	55 %	50 %	100 %
	Glancing incidence ($i = g$)	18 %	85 %	100 %
W(110)	Normal incidence ($i = n$)	45 %	42.5 %	100 %
	Glancing incidence ($i = g$)	9 %	67.5%	100 %

Table 9-3 The values of the Auger sensitivity factors involved in the simulation of the nitrogen AES signals in the stimulated adsorption experiments on W(100) and (110). The relative values of the rate constants were set at $k_1 = k_2 = 2 \times k_3$.

The data fitting in figures 9-9 to 9-12, generated from fractional surface coverages θ_{NH_X} simulated with rate constants $k_1 = k_2 = 2\times k_3$, show some improvement over the earlier simulation scheme with $k_1 = k_2 = k_3$. In the normal incidence electron beam adsorption experiments, the difference due to the initial sharp rise of the simulated signals was smaller on both crystal orientations. For the stimulated adsorption experiments using the glancing incidence electron beam, the data simulation with this new condition also yielded a more satisfactory fit with the experimental data. The agreement between the two data series for the first 15 minutes of electron irradiation time was good. This was the period in which the simulated data could also demonstrate a linear signal increase with time. The advantage of this new simulation condition over the previous one was revealed by better agreement in the later period of the adsorption experiments. While the simulated signals stopped increasing linearly with time, the deceleration was less than in the previous data simulation.

While improvements were achieved by doubling the relative magnitudes of the rate constants k_1 and k_2 over k_3, the changes were limited in size only. The features of the disagreement between the simulated and the experimental data were never eliminated. Data simulations with other modifications on the relative sizes of the rate constants were conducted:

- $k_1 = k_2 = 3 \times k_3$,
- $k_1 = k_2 = 4 \times k_3$,
- $k_1 = k_2 = 1/2 \times k_3$,
- $k_1 = k_2 = 1/3 \times k_3$.

None of them led to significant improvement. The imperfection of this data simulation appeared to lie elsewhere than in the relative magnitudes of the rate constants.

9.4 INCREASED STERIC HINDRANCE CONSTRAINT

The other significant assumption in the present model is the total relaxation of steric hindrance against the occupation of all adjacent vacant sites when a single NH_2 dissociates to NH. Perhaps sizes demand that a vacant site can only be occupied by NH_3 if two adjacent occupied sites have undergone dissociation to NH. In the previous picture it required only one such event.

The new variation on the data simulation process now was to assume that it took the electron stimulated dissociation of not just one, but two of the surrounding NH_2(ad) to make the vacant site available for further ammonia adsorption. Once an ammonia molecule was allowed to adsorb onto this vacant site, electron stimulation could dissociate it and its NH_2 fragment would be chemisorbed onto the surface, completing the electron stimulated ammonia adsorption process.

9.4.1 Signal generation

On the same hypothetical array of 14 × 14 surface sites, 98 NH_2 adsorbates were again positioned at every other surface site in a C(2×2) array. Four occupied neighbour sites thus surrounded every vacant site. The list of random coordinates applied in the same fashion to mimic electron bombardment on the specific part of the surface. Every electron bombardment on an occupied site would lead to a stimulated dissociation of the local NH_X ($x = 1$-3) and partly relieve the steric hindrance experienced by its four neighbouring vacant sites. However, in this new scheme a more severe relaxation condition must be met in order to activate this vacant site for further ammonia adsorption. A vacant site would only become available for ammonia accommodation when two of its four neighbour NH_2(ad) were dissociated and changed to NH(ad), which was of a smaller van der Waals diameter (figure 9-13). The values of the rate constants were taken to be equal ($k_1 = k_2 = k_3$), neglecting any difference in the cross-section for electron stimulated dissociation of the three NH_X species (x = 1-3). The evolution of the fractional coverages of the various ammonia species with electron bombardment is displayed in figure 9-14.

An obvious difference of this fractional coverage evolution profile over the previous two (figures 9-3 and 9-8) was the change of the $NH_{2,3}$ coverage at the beginning. Instead of rapidly increasing from 0.5 ML, it decreased initially in this scheme. In the past two data simulation schemes, one electron stimulated dissociation of a ground statea dsorbed NH_2

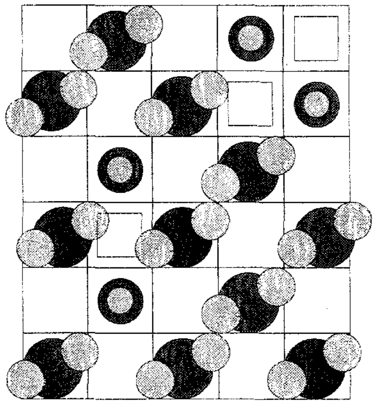

Figure 9-13
The same array with 4 NH_2 become NH and the 3 neighbour sites (double squares) become available for ESA.

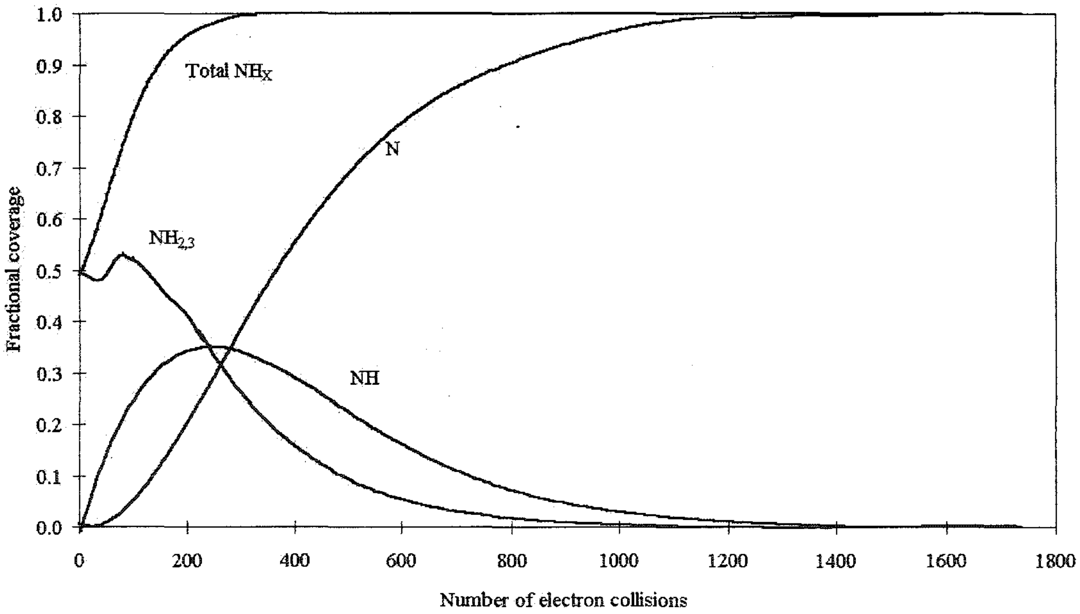

Figure 9-14 Site-filling simulation results for the fraction coverage of NH_X with $k_1 = k_2 = k_3$. Vacant site re-activation only achieved by electron stimulated dissociation of at least two of the four neighbouring $NH_2(ad)$.

could easily lead to adsorption of four new NH_3 molecules. One dissociation would reduce the steric hindrance on its four neighbouring vacant sites. Therefore a net gain of three $NH_{2,3}$ resulted, and led to the spike observed for $\theta_{NH_{2,3}}$ in the two earlier data simulations. In this new simulation scheme the initial stimulated dissociation of ground state adsorbed NH_2 would not immediately lead to extra adsorption of ammonia, because of the more severe condition for the activation of a vacant surface site. The net result was therefore an early, true depletion of NH_2, as observed for the initial decrease in the $\theta_{NH_{2,3}}$ profile. The replenishment of NH_3 into $\theta_{NH_{2,3}}$ did not balance the loss of NH_2 until a significant amount of the ground state NH_2 was already dissociated. It set a stage that one more stimulated dissociation of an NH_2 could lead to extra adsorption of NH_3. At that moment the $\theta_{NH_{2,3}}$ increased again and eventually reached to a relative maximum of ~0.53 ML.

9.4.2 Results of the data simulation with the more severe relaxation condition

The simulated nitrogen AES signals were again generated using equation 9-1 and the newly determined fractional coverages of the degrading ammonia adsorbates. The comparisons were shown in figures 9-15 (normal incidence electron beam) and 9-16 (glancing incidence electron beam) for the adsorption results on W(100), and in figures 9-17 (normal incidence electron beam) and 9-18 (glancing incidence electron beam) for the adsorption results on W(110).

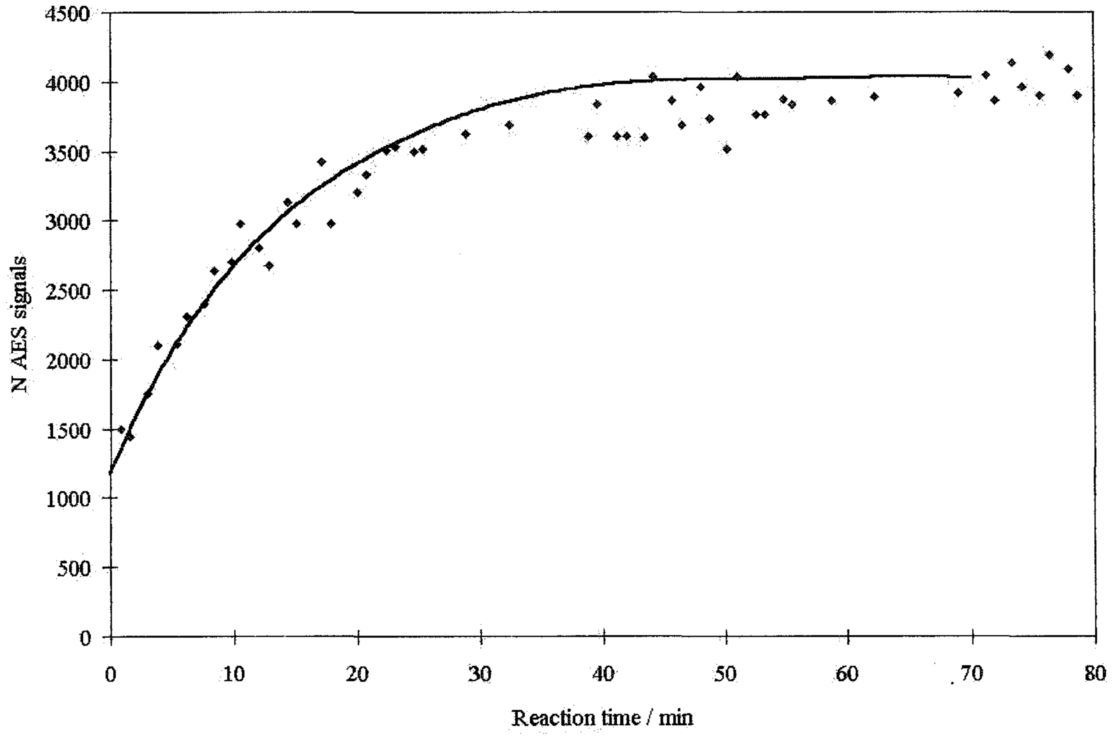

Figure 9-15 The comparison between the simulated nitrogen AES signals and the experimental AES signals of the electron stimulated NH_3 adsorption on W(100), 5×10^{-7} torr NH_3, 300 K, normal incidence electron beam.

Rate constants $k_1 = k_2 = k_3$.

Simulation parameters: $\alpha^{n}_{NH2,3}$ 63%, α^{n}_{NH} 42.5% and α^{n}_{N} 100%.

A more severe condition for re-activation of vacant sites, see text for detail.

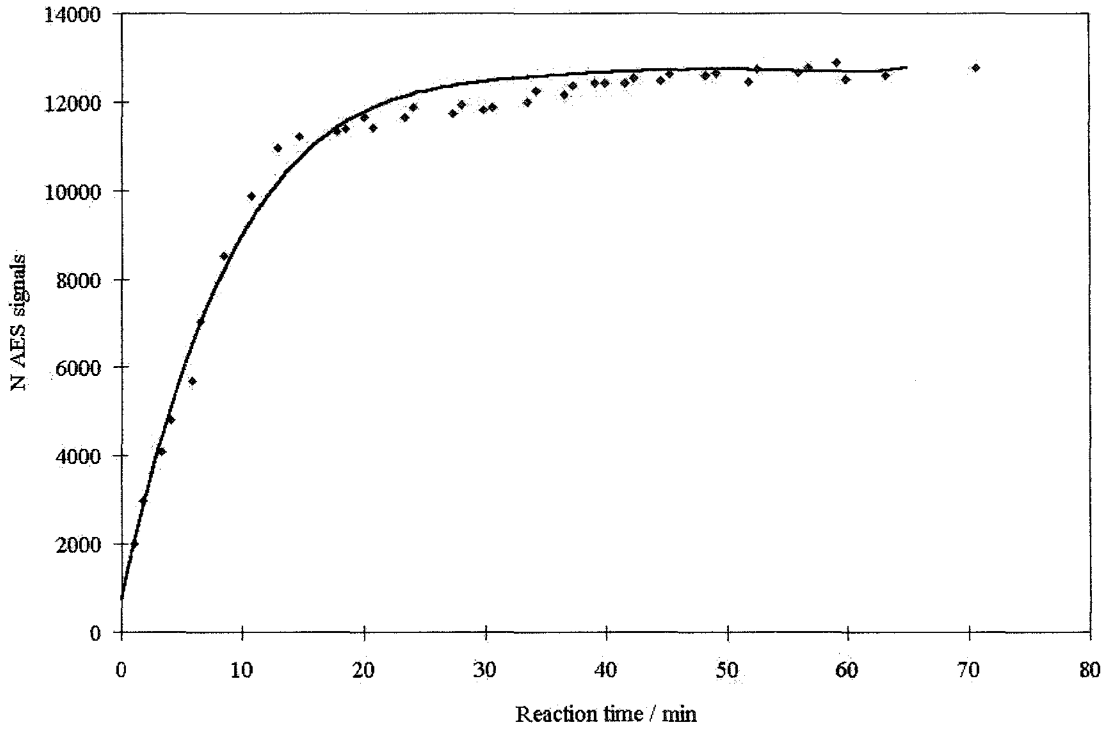

Figure 9-16 The comparison between the simulated nitrogen AES signals and the experimental AES signals of the electron stimulated NH_3 adsorption on W(100), 5×10^{-7} torr NH_3, 300 K, glancing incidence electron beam.

Rate constants $k_1 = k_2 = k_3$.

Simulation parameters: $\alpha^{g}_{NH2,3}$ 18%, α^{g}_{NH} 90% and α^{g}_{N} 100%.

A more severe condition for re-activation of vacant sites, see text for detail.

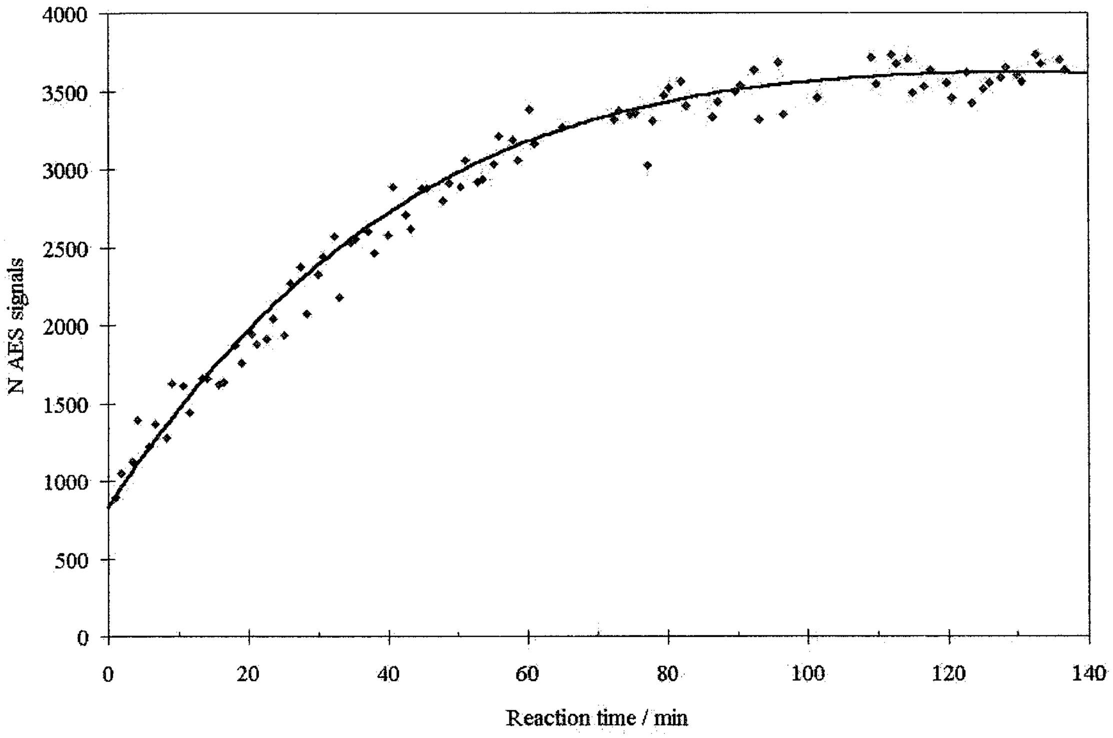

Figure 9-17 The comparison between the simulated nitrogen AES signals and the experimental AES signals of the electron stimulated NH_3 adsorption on W(110), 5×10^{-7} torr NH_3, 300 K, normal incidence electron beam.

Rate constants $k_1 = k_2 = k_3$.

Simulation parameters: $\alpha^{n}{}_{NH2,3}$ 50%, $\alpha^{n}{}_{NH}$ 40% and $\alpha^{n}{}_{N}$ 100%.

A more severe condition for re-activation of vacant sites, see text for detail.

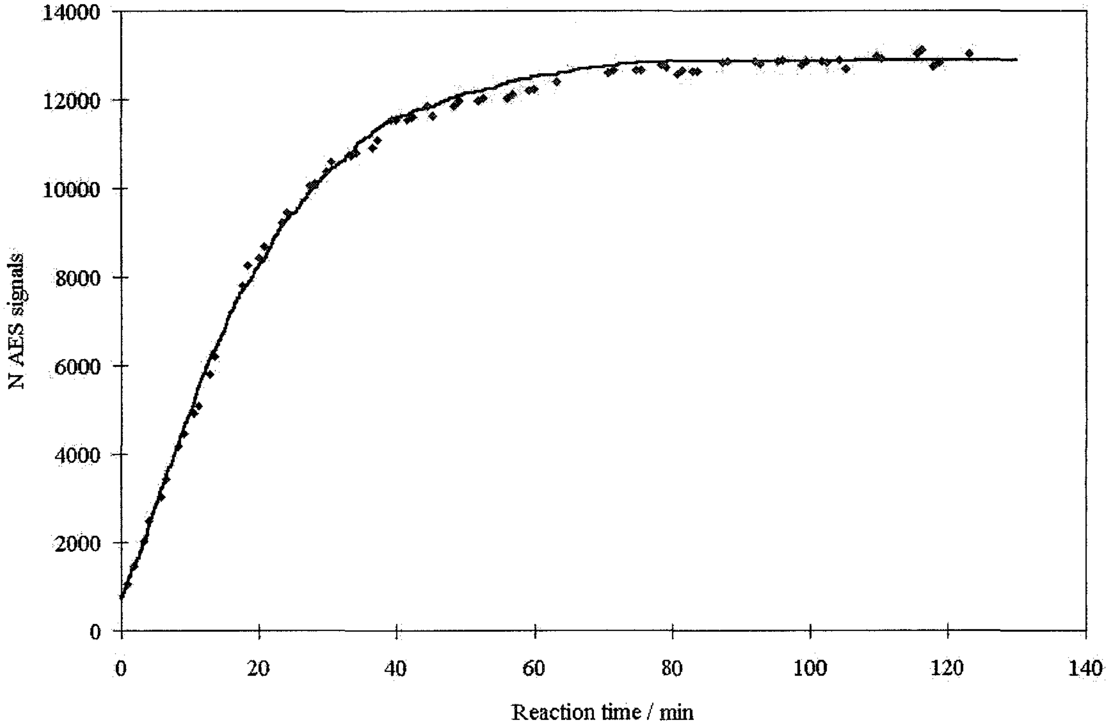

Figure 9-18 The comparison between the simulated nitrogen AES signals and the experimental AES signals of the electron stimulated NH_3 adsorption on W(110), 5×10^{-7} torr NH_3, 300 K, glancing incidence electron beam.

Rate constants $k_1 = k_2 = k_3$.

Simulation parameters: $\alpha^{g}{}_{NH2,3}$ 11.5%, $\alpha^{g}{}_{NH}$ 75% and $\alpha^{g}{}_{N}$ 100%.

A more severe condition for re-activation of vacant sites, see text for detail.

The simulated data appeared to match well with the experimental nitrogen AES signals in all four cases. One imperfection that might be criticized is a disagreement between the two at the turning point (between 85% and 95% of relative nitrogen AES signals) of the signal evolution profile of the glancing incidence electron beam experiments.

The relevant values of the Auger sensitivity factors of the four electron stimulated ammonia adsorption experiments on W(100) and W(110) are shown in table 9-4.

		$\alpha^i_{NH2,3}$	α^i_{NH}	α^i_N
W(100)	Normal incidence ($i = n$)	63 %	42.5 %	100 %
	Glancing incidence ($i = g$)	18 %	90 %	100 %
W(110)	Normal incidence ($i = n$)	50 %	40 %	100 %
	Glancing incidence ($i = g$)	11.5 %	75%	100 %

Table 9-4 The values of the Auger sensitivity factors involved in the simulation of the nitrogen AES signals in the stimulated adsorption experiments on W(100) and (110). The relative values of the rate constants were set at $k_1 = k_2 = k_3$. A more severe condition for re-activation of vacant sites, see text for detail.

The agreement could certainly be improved by further adjustment of the small numbers of adjustable parameters in the model or by removing some of the constraints, *e.g.*, $k_1 = k_2 = k_3$, identical probabilities for normal and glancing incidence or more subtle steric considerations. It is not felt that the present data justify any extensions at this time.

9.5 Revisit of the ESA active site - chemisorption site model

The new site exclusion adsorption model has solved a very important feature in our ESA experimental results (the apparent coverage-independent nitrogen AES signal increase rate). In this section we will compare this model with the ESA active site - chemisorption site model.

While the ESA active site - chemisorption site model was designed to offer a coverage-independent ESA rate, there are two glaring disadvantages: (*a*) the failure in identifying the ESA active sites on the crystal surface, and (*b*) the contradiction in the constancy of ESA active sites in the induction period discussion.

The dilemma in (*a*) has already been discussed in previous sections. In the site exclusion adsorption model, the apparent coverage-independence of the rate of nitrogen AES signal is appropriately explained by the site exclusion principle and the Auger sensitivity factors. This is a clear improvement over the ESA active site - chemisorption site model which interprets the experimental results inappropriately as an apparent coverage-independence of ESA rate.

Another advantage of this site exclusion adsorption model shows in explaining the induction period. In chapter six, the ESA active site - chemisorption site model only manages to offer a speculation about the origin of the observed induction period. It is a duration in which the ESA active sites are forming on the surface. This contradicts the basic of this model which requests a constant number of ESA active sites so as to offer a constant ESA rate.

In the current site exclusion model, the vacant sites are naturally made available for ESA by ESD of the neighbouring adsorbates. The high temperature condition made the crystal surface crowded with ground state adsorbed NH_2 at the beginning. It is understandable if it takes a longer time to dissociate enough NH_2(ad) via electron stimulation, which in turn opens the vacant sites for ESA by steric hindrance relaxation.

Therefore there is a duration (the induction period) of which the ESA rate is apparently zero. The low pressure condition enhances the effect because it lowers the collision frequency of the gaseous ammonia molecules bombarding the available vacant surface sites. This is going to be the principle way of getting ammonia onto the vacant sites for electron stimulation. The surface concentration of the hydrogen-bonded precursor state ammonia precursors (7 kJ mol^{-1} desorption energy) is next to negligible at the high crystal temperature. Therefore the length of induction period extends with a decreasing ammonia pressure.

Most importantly, in the site exclusion adsorption model it there is no need to differentiate surface sites like the ESA active site - chemisorption site model does. There simply is no evidence for the surface site differentiation as required in this model. In the site exclusion model, ESA eventually happens on every vacant site. It does not require any rapid surface diffusion of NH_2 from one site to another site.

In summary, the site exclusion adsorption model is superior to the ESA active site - chemisorption site model in every way. It is advantageous to adopt this site exclusion model for the electron stimulated adsorption of ammonia on the tungsten single crystal surfaces.

9.6 CONCLUSION

Generally speaking this last data simulation scheme was shown to be successful in duplicating the genuine nitrogen AES signal profile on both crystal orientations and in experiments with either electron beam. The most interesting feature about the initial rise of the nitrogen AES signals was reproduced. The signal increase was of a constant rate, seemingly coverage-independent and continued from the beginning till as high as 70% of saturation level.

The success of the current adsorption model is based on the consideration of different nitrogen Auger sensitivities for different NH_X adsorbates and the concept of vacant site activation and steric hindrance relaxation. The utilization of these ideas provides a satisfactory explanation for the important observation of the long-lasting, coverage-independent nitrogen AES signal increase. Previously, this feature needed to be treated as a coverage-independent ammonia adsorption rate. Without the hypothesis of the variable Auger sensitivity, every nitrogen-containing adsorbate was regarded as making the same contribution to the overall nitrogen AES signals. Under this assumption, all increase of the nitrogen AES signal must come as a result of increase of ammonia adsorption. Fitting the observation of coverage-independent nitrogen AES signal increase became a mission of finding a way to allow the stimulated adsorption of new ammonia molecules in a coverage-independent fashion, which was difficult. A model was suggested which involved two kinds of surface sites: ESA active sites (where $NH_3 \xrightarrow{e} NH_2 + H$ was thought to happen) and chemisorption sites (where NH_2 was favourably adsorbed). In theory this model allowed the ammonia adsorbed to increase in the required linear fashion. However this model also generated additional un-resolved problems, such as the physical or chemical uniqueness of an ESA active site over a chemisorption site.

The current data simulation scheme, on the other hand, avoided the disadvantages of the “ESA active site – chemisorption site”. It separated the magnitude of the nitrogen AES signals and the <u>total</u> surface coverage of nitrogen. The flexibility was achieved by the Auger sensitivity concept, which was backed by the different number of the nitrogen-bonded hydrogen atoms and the different relative orientation between these N-H bonds and the incident primary electron beam for the various NH_X (x = 0-3). The surface concentrations of each adsorbate species were continually changing, by new ammonia adsorption and electron stimulated dissociation, during the adsorption process. The combination of the varying NH_X surface concentration and the different Auger sensitivity factors managed to describe the important result of the coverage-independent rate of increase of the nitrogen AES signal, while allowing a more conventional, truly coverage-dependent ammonia adsorption mechanism.

In fact the glancing incidence AES data demand a dependence of nitrogen Auger sensitivity on NH_X composition. There are obvious and serious ramifications for the use of AES for surface analysis of all species containing N and H.

CHAPTER TEN

SUMMARY AND CONCLUSIONS

The observations and conclusions from the previous chapters will be highlighted in this chapter, and suggestions for future work proposed.

10.1 ELECTRON STIMULATED REACTIONS

In an ammonia environment, when a tungsten single crystal surface is irradiated with an electron beam, excitation processes such as stimulated adsorption and dissociation can occur on both W(100) and W(110). Ground state adsorption of ammonia at 300 K saturates the crystal surfaces with a half monolayer nitrogen coverage. Electron stimulation increases the saturation coverage to one full monolayer.

10.1.1 Coverage-independent rate of nitrogen AES signal increase

The initial rates of change of the nitrogen AES signals are observed to be constant and coverage-independent till ~ 70 % of saturation level. The range of ammonia pressure in which the linearity is observed is nearly two orders of magnitude from 1×10^{-9} torr, and the crystal temperature range is over 150 K from room temperature. At first this observation led us to propose an "activation site - chemisorption site" adsorption mechanism. The rapid regeneration of the activation sites prevents the reaction rate from being slowed down by accumulation of adsorbates. This model was eventually abandoned because these special surface sites were not identified. Moreover a better model was subsequently revealed by hydrogen screening effects.

The dependence of the stimulated adsorption kinetics on various experimentally controllable conditions was investigated.

10.1.2 Reaction order and ammonia pressure

The reaction order with respect to the ammonia pressure decreased to zero in the 10^{-8} torr pressure range in electron stimulated ammonia adsorption experiments on W (100) and W(110) at room temperature. The critical values of the gas pressure was found to be 3×10^{-8} torr on W(100) and 8×10^{-8} torr on W(110). With lower gas pressure, the rate of stimulated ammonia adsorption decreases with pressure on both orientations.

10.1.3 Binding energy of ammonia precursors and crystal temperature

The investigation of the effects of crystal temperature on the kinetics of electron stimulated ammonia adsorption revealed two states of ammonia adsorption. One of them is an adlayer-hydrogen-bonded, physisorbed precursor state. The binding energies are determined to be 7 ± 11 and 6 ± 5 kJ mol^{-1} on W(100) and W(110) respectively. The values being independent of crystal orientation support the idea that the ammonia molecules are connected to the adlayer but not the substrate atoms.

The other adsorption state has a binding energy of 120 ± 11 kJ mol^{-1} on the W (100) surface. It is believed to be an ammonia molecule adsorbed onto a vacant site surrounded by bulky NH_2 adsorbates. The high energy value suggests it is a chemisorption – the ammonia molecule is bonded to the tungsten surface via the lone pair electrons on the nitrogen atom. The stimulated adsorption rate only significantly decreases after the crystal temperature is over 150 K above room temperature. This suggests the saturation of tungsten-bonded ammonia is only relaxed above this temperature. The results show that the saturation nitrogen coverage decreases when the crystal temperature increases. This suggests a dynamic balance between electron stimulated adsorption (ESA) and thermal or electron stimulated desorption (ESD).

10.2 EFFECT OF THE ELECTRON BEAM

10.2.1 Electron beam current density

The magnitude of the electron current density affects the stimulated adsorption in a first order manner. A timesaving experimental method was developed to study this effect, without compromising the danger of making Auger measurements in the presence of residual ammonia pressure.

The cross-section for the electron stimulated ammonia adsorption on W(110) is calculated to be 3.4×10^{-16} cm^2, in very good agreement with published results of similar systems [Anderson and Estrup 1968, Danielson *et al.* 1978, Klauber *et al.* 1985 and Sun *et al.* 1993].

10.2.2 Electron beam angle of incidence

This angle dependence is found to affect primarily the Auger analysis and minimally the adsorption kinetics. The nitrogen AES signal evolution graphs of adsorption experiments with electron beams of normal and glancing incidence showed the reaction approaches completion in both cases at the same time.

Most interestingly, while we are puzzled at understanding the coverage-independent *adsorption rate*, we eventually realized an assumption of equating the nitrogen AES signal and the nitrogen coverage is invalid. Each nitrogen-containing species (N, NH, NH_2 or NH_3) contributes differently to the measured nitrogen AES signal. The results led us to believe the bonded hydrogen atoms exert a primary electron beam shielding effect on the attached nitrogen atom. When the hydrogen atoms are right in the electron path to the nitrogen atom, the probability of the nitrogen atom being ionized (and thus ejecting the characteristic Auger electron) is reduced. Such is the case for $NH_{2,3}$ under a glancing incidence electron beam, and NH under a normal incidence beam. This results in a low value for the Auger sensitivity, a measure of how well the nitrogen atom is measured by the AES technique.

The overall nitrogen AES signal measured can be expressed as a summation of products of the Auger sensitivity and the surface concentration of each nitrogen-containing adsorbate.

$$\text{Nitrogen AES signal at time } t = \sum_{x=0}^{3} \left(\alpha^{i}_{\mathrm{NH_x}} \cdot \theta_{\mathrm{NH_x}} \right)$$

The coverage evolution of each species during the reaction period is simulated by a mathematical approach and a site filling method. The latter is detailed to consider the possible steric hindrance that limit the availability of the vacant sites for ammonia precursor adsorption — the steric hindrance being exerted by bulky adsorbate molecules surrounding the vacant sites. Each simulation method has demonstrated a certain degree of success, and allowed a coverage-dependent adsorption rate resulting in a coverage-independent Auger signal increase. These observations have a serious impact on AES surface analysis of systems involving species containing nitrogen and hydrogen.

10.3 SUGGESTIONS FOR FUTURE WORK

10.3.1 Determination of coverage of each adsorbate species

The reliability of the Auger sensitivity values of individual adsorbate species can be enhanced tremendously when the surface concentration values are more precisely determined. Our two primary analytical tools, AES and LEED, do not allow such an investigation. The electronic configurations of the nitrogen atom of the four adsorbate species (N, NH, NH_2 and NH_3) are different, because the number of bonded hydrogen atoms and the degree of electron mixing with the substrate tungsten atoms is different for each of them. However, the difference in the characteristic energy of the Auger electrons is so small that it is beyond the resolution of our AES system. A LEED study is also not suitable for this task of coverage determination. Changes of surface symmetry of the adsorbate layer will help determine the coverage of adsorbates, but the 10^{-7} torr gas pressure condition would not sustain a long-range order of adsorbate which is necessary in LEED analysis.

This task may be better suited to surface analytical techniques such as ultraviolet photoemission spectroscopy (UPS), high-resolution electron energy loss spectroscopy (HREELS), or second harmonic generation (SHG) [Somorjai and Rupprechter 1998]. These analytical tools give information on the bonding of adsorbates to the surface.

10.3.2 Angle of incidence of electron beam: adsorption kinetics or AES?

The discussed adsorbate coverage determination during the adsorption experiments (by analytical techniques not using an electron probe as AES does) can lead to a more definite answer as to whether the kinetics of the electron stimulated ammonia adsorption on tungsten is affected by the angle of incidence of the electron beam. Currently we conclude that the incidence angle of the beam does not affect the adsorption kinetics because the nitrogen AES signals reached their maximum at approximately the same time in experiments with either electron beam. Such approach would also fail to explain the different $\left.\frac{\text{G.I.(W)}}{\text{N.I.(W)}}\right|_{t_0}$ signal ratio discussed in chapter eight. The second argument, however, is based on an assumption of mutual exclusion that the angle of incidence of the electron beam affects either the kinetics or the AES analysis. The experimental coverage determination can help clarify this issue.

10.3.3 Variation in the angle of incidence of electron beam

Our preliminary analysis found out when the N–H bond is parallel to the incident electron beam, such as NH(ad) to N.I. electron beam or to a lesser extent $NH_{2,3}$(ad) to GI electron beam, the hydrogen shielding is very strong. Currently our glancing incidence angle electron gun is 75° off-normal. The N–H bonds in NH_2 and NH_3 is about 65° off-normal, however. The use of an electron gun capable of varying the angle of incidence can reveal a lot more information about this alignment factor in hydrogen shielding effect. For example, if a 65° off-normal electron beam generated AES data that lead to an even lower $\alpha^{g}_{NH_{2,3}}$ signal ratio then it will become a very positive evidence for the validity of our conclusions.

In addition, these experiments can generate a reference to check if the ammonia adsorbate is tilted on the crystal surface. So far it is only an assumption that the principal axis of NH_2 and NH_3 being parallel to the surface normal. The assumption is most likely valid, but it is worthy to point out at Mocuta *et al.* [1997a] has shown ammonia adsorbed at tilted orientation on Cu(110) surface at very low temperature (80 K). Two of the three hydrogen atoms develop weak interactions with the substrate atoms and pull themselves towards the crystal surface.

Such studies over a range of angles of incidence would give a better understanding of the subtle differences between the kinetics on the W(100) and W(110) surfaces. Further insight would come from studies in which it was possible to rotate the crystal about its normal, *i.e.*, vary the azimuthal angle.

10.4 CONCLUDING REMARKS

The work presented in this thesis is the first systematic investigation of the kinetics of electron stimulated adsorption of ammonia on tungsten single crystal surfaces, and any ammonia / transition metal system to the best of the author's knowledge.

Ammonia adsorption has been studied for a long time because of its industrial and technological importance (*e.g.*, catalysts for ammonia synthesis, or metallic nitride thin films as protective coatings). Many investigators have used analytical techniques which use electrons as probe (*e.g.*, AES and LEED) to make measurements in the presence of ammonia gas. Few paid attention to the fact that the analysis being conducted was actually altering the effects they intended to study. Furthermore the effect of hydrogen on the Auger sensitivity of nitrogen puts new constraints on surface analysis by Auger electron spectroscopy.

References

Alnot, P., Cassuto, A. and King, D. A., *Faraday Discuss. Chem. Soc.*, **87**, 291-302 (1989)

Anderson, J. and Estrup, P. J., *Surf. Sci.*, **9**, 463-467 (1968)

Armstrong, R. A., *Diffraction methods*, in *Experimental methods in catalytic research*, Anderson, R. B. and Dawson, P. T. (Eds), Vol. 3, Academic Press, Inc., New York, 1976.

Barr, T. L., *Modern ESCA: The principles and practice of X-ray photoelectron spectroscopy*, CRC Press, Boca Raton, 1994. pp. 5-29.

Bater, C., Sanders, M. and Craig Jr., J. H., *Surf. Interface Anal.*, **29**, 208-214 (2000) (a)

Bater, C., Sanders, M. and Craig Jr., J. H., *Surf. Sci.*, **451**, 226-231 (2000) (b)

Berkowitz, J., Ellison, G. B. and Gutman, D., *J. Phys. Chem.*, **98**, 2744-2765 (1994)

Bessent, M. P., Hu, P., Wander, A. and King, D. A., *Surf. Sci.*, **325**, 272-278 (1995)

Bishop, H. E., *Proc. Phys. Soc. (London)*, **85**, 855-866 (1965)

Brundle, C. R., *J. Vac. Sci. Technol.*, **11**, 212-224 (1974)

Burns, A. L., Stechel, E. B. and Jennison, D. R., *Surf. Sci.*, **363**, 303-312 (1996)

Chambers, S. A., *Scienc*, **248**, 1129 (1990)

Chen, Y., *Transition metal nitride surfaces and electrons*, Ph. D. Dissertation, McMaster University, 1996.

Childs, K. L. and Hedberg, C. L., *Handbook of Auger electron spectroscopy*, 3rd ed., Physical Electronics Inc., Eden Prairie, Minn., 1995.

Danielson, L. R., Dresser, M. J., Donaldson, E. E. and Sandstrom, D. R., *Surf. Sci.*, **71**, 615-629 (1978)

Dawson, P. T., *J. Catal.*, **33**, 47-56 (1974)

Dawson, P. T. and Hansen, R. S., *J. Chem. Phys.*, **48**, 623-636 (1968).

de Segovia, J. L., *Vacuum*, **47**, 333-340 (1996)

Diebold, U. and Madey, T. E., *J. Vac. Sci. Technol.*, **A10**, 2327-2335 (1992)

Egawa, C., Shindo, H., Onishi, T. and Tamaru, K., *J. C. S. Faraday I*, **77**, 927-935 (1981)

Egawa, C,. Naito, S. and Tamaru, K., *Surf. Sci.*, **131**, 49-60 (1983)

Egelhoff Jr.,W. F., Linnett, J. W. and Perry, D. L., *Faraday Discuss. Chem. Soc.*, **60**, 127-136 (1976)

Egelhoff Jr., W. F., *Phys. Rev. Lett.*, **59**, 559-562 (1987)

Egelhoff Jr., W. F., *J. Vac. Sci. Technol.*, **A 6**, 730-734 (1988)

Egelhoff Jr., W. F., Gadzuk, J. W., Powell, C. J. and Van Hove, M. A., *Science*, **248**, 1129 (1990)

Egelhoff Jr., W. F., *Crit. Rev. Solid States Mat. Sci.*, **16**, 213-235 (1990)

Ermich, W., *Philips Res. Repts.*, **20,** 94-105 (1965)

Espenson, J. H., *Chemical kinetics and reaction mechanisms*, McGraw-Hill, Inc., New York, 1981. pp. 65-69

Estrup, P. J. and Anderson, J. *J. Chem. Phys.*, **46**, 563-567 (1967) (a)

Estrup, P. J. and Anderson, J. *J. Chem. Phys.*, **46**, 567-570 (1967) (b)

Estrup, P. J. and Anderson, J. *J. Chem. Phys.*, **49**, 523-528 (1968)

Haber, F. and Le Rossignol, R., *Z. Elektrochem.*, **14**, 181-196 (1908)

Hagstrum, H. D., Rowe, J. E. and Tracy, J. C., *Electron spectroscopy of solid surface*, in *Experimental methods in catalytic research*, Anderson, R. B. and Dawson, P. T. (Eds), Vol. 3, Academic Press, Inc., New York, 1976.

Griffiths, K., King, D. A., Aers, G. C. and Bendry, J. B., *J. Phys. C: Solid State Phys.*, **15**, 4921-4931 (1982)

Grosman, M. and Löffler, D. G., *J. Catal.*, **80**, 188-193 (1983)

Habbard, A. T., Frank, D. G., Batina, N., Golden, T. and Lu, F., *Science*, **247**, 182-188 (1990) (a)

Habbard, A. T., Frank, D. G. and Golden, T., *Science*, **248**, 1131-1133 (1990) (b)

Jablonski, A. and Powell, C. J., *Surf. Sci. Report*, **47**, 33-91 (2002).

Klauber, C., Alvey, M. D., and Yates Jr., J. T., *Surf. Sci.*, **154**, 139-167 (1985).

Kroll, P. *Phys. Rev. Lett.*, **90**, 125501/1-125501/4 (2003)

Lambert, R. M. and Bridge, M. E., *Chemisorption of the hydrides and oxides of nitrogen on metal surfaces*, in *The chemical physics of solid surfaces and heterogeneous catalysis*, King, D. A. and Woodruff, D. P. (Eds.), Vol. 3B, Elsvier Science Publishers B. V., Amsterdam, 1984.

Lichtman, D., *Ultramicroscopy,* **23**, 291-298 (1987)

Lide, D. R. (ed.), *CRC Handbook of Chemistry and Physics,* 83rd ed., CRC Press, Cleveland, 2003.

Lindau, I., and Spicer, W. E., *J. Electron Spectrosc. Relat. Ph.*, **3**, 409-413 (1974)

Madey, T. E. and Yates Jr., J. T., *J. Vac. Sci. Technol.*, **8**, 525-555 (1971)

Madey, T. E., *Surf. Sci.*, **299/300**, 824-836 (1994)

Masson, D. P., Merrill, R. P. and Houston, P. L., *Surf. Sci.*, **330**, 239-254 (1995)

Matsushita, K. and Hansen, R. S., *J. Chem. Phys.*, **52**, 4877-1889 (1970)

Max Appl., *Ammonia*, in *Ullmann's Encyclopedia of Industrial Chemistry*, Wiley-VCH Verlag GmbH & Co.KGaA, 2002. (http://www.mrw.interscience.wiley.com/ueic/articles/a02_143/frame.html)

May, J. W., Szostak, R. J. and Germer, L. H., *Surf. Sci.*, **15**, 37-76 (1969)

McAllister, J. and Hansen, R. S., *J. Chem. Phys.*, **59**, 414-22 (1973)

McDaniel, E. W., *Atomic Collisions: Electron and photon projectiles*, John Wiley & Sons Inc., New York, 1989. pp 18-25.

Menzel, D., *J. Electron Spectrosc. Relat. Ph.*, **76**, 73-83 (1995)

Menzel, D. and Gomer, R., *J. Chem. Phys.*, **41**, 3311-3328 (1964)

Mocuta, D., Ahner, J. and Yates Jr., J. T., *Surf. Sci.*, **383**, 299-307 (1997) (a)

Mocuta, D., Ahner, J. and Yates Jr., J. T., *J. Chem. Phys.*, **107**, 5968-5972 (1997) (b)

Neave, J. H., Foxon, C. T. and Joyce, B. A., *Surf. Sci.*, **29**, 411-423 (1972)

Peng, Y. K. and Dawson, P. T., *J. Chem. Phys.*, **54**, 950-961 (1971)

Pilling, M. J. and Seakins, P. W., *Reaction kinetics*, Oxford University Press, New York, 1995. pp. 198-200

Powell, C. J., *Surf. Sci.*, **44**, 29-46 (1974)

Ramsier, R. D. and J. T. Yates Jr., *Surf. Sci. Report*, **12**, 243-378 (1991)

Rao, C. N. R. and Rao, G. R., *Surf. Sci. Report*, **13**, 221-263 (1991)

Raval, R., Harrison, M. A. and King, D. A., *Nitrogen adsorption on metals*, in *The chemical physics of solid surfaces and heterogeneous catalysis*, King, D. A. and Woodruff, D. P. (Eds.), Vol. 3A, Elsvier Science Publishers B. V., Amsterdam, 1990.

Redhead, P. A., *Can. J. Phys.*, **42**, 886-905 (1964)

Reed, A. P. C. and Lambert, M., *J. Phys. Chem.*, **88**, 1954-1959 (1984)

Rivière, J. C., *Surface Analytical Techniques*, Oxford University Press, New York, 1990. pp 219-237.

Schwaner, A. L., Pylant, E. D. and White, J. M., *J. Vac. Sci. Technol.*, **A14**, 1453-1456 (1996)

Seah, M. P. *Quantification of AES and XPS*, in *Practical surface*, Briggs, D. and Seah, M. P. (Eds), Chichester, John Wiley & Sons Ltd., 1983.

Shamir, N., Lin, J. C. and Gomer, R., *Surf. Sci.*, **214**, 74-84 (1989)

Shindo, H., Egawa, C., Onishi, T. and Tamaru, K., *J. C. S. Faraday I*, **76**, 280-290 (1980)

Somerton, C. and King, D. A., *Surf. Sci.*, **89**, 391-402 (1979)

Somorjai, G. A. and Rupprechter, G., *J. Chem. Edu.*, **75**, 162-176 (1998)

Sun, Y.-M. and Ekerdt, J. G., *J. Vac. Sci. Technol.*, **B 11**, 610-613 (1993)

Sun, Y.-M., Sloan, D., Huett, T., White, J. M. and Ekerdt, J. G., *Surf. Sci. Lett.*, **295**, L982-L986 (1993)

Sun, Y.-M., Sloan, D., Ihm, H. and White, J. M., *J. Vac. Sci. Technol.*, **A14**, 1516-1521 (1996)

Tarasova, O. L., Kotlyar, V. G., Saranin, A. A., Khramtsova, E. A. and Lifshits, V. G., *Surf. Sci.*, **310**, 209-216 (1994)

Toth, L. E., *Transition Metal Carbides and Nitrides*, Academic Press, New York, 1971.

Tucker, Jr., C. W., *Surf. Sci.*, **2**, 516-521 (1964)

Tully, J. C., *Annu. Rev. Phys. Chem.*, **51**, 153-178 (2000)

Wang, X.-D., Han, Z.-L., Tonner, B. P., Chen, Y. and Tong, S.Y., *Scienc*, **248**, 1129-1131 (1990)

Woodruff, D. P. and Delchar, T. A., *Modern techniques of surface science*, 2nd ed., Cambridge University Press, Cambridge, 1994. Chapter 3.

Woodruff, D. P., *Scienc*, **248**, 1131 (1990)

Uebing, C., *Prog. Solid State Chem.*, **26**, 157-240 (1998)

Yih, S. W. H. and Wang, C. T., *Tungsten: Sources, Metallurgy, Properties and Applications*, Plenum Press, New York, 1979.

Zaera, F., *Prog. Surf. Sci.*, **69**, 1-98 (2001)

Zerr, A., Miehe, G. and Riedel, R., *Nature Materials*, **2**, 185-189 (2003)